Bulk and confinement-induced phase transitions in colloidal suspensions

Cover:
Density contour plot of the configuration shown in Fig. 8.4(a).

Images at the bottom of the odd pages:
Snapshots from a Brownian dynamic simulation of hard spheres with a short range attractive interaction (see chapter 8). The final configuration in also shown in Fig. 8.4(a).

A digital version of this thesis is available at http://www.colloid.nl
Author contact: a.fortini@phys.uu.nl

ISBN-13: 978-90-9021513-6

Bulk and confinement-induced phase transitions in colloidal suspensions

Fasenovergangen van colloïdale suspensies in bulk en begrensde geometrieën

(met een samenvatting in het Nederlands)

PROEFSCHRIFT

ter verkrijging van de graad van doctor aan de Universiteit Utrecht
op gezag van de rector magnificus, prof.dr. W. H. Gispen
in gevolge het besluit van het college voor promoties
in het openbaar te verdedigen
op maandag 12 Februari 2007, te 10.30 uur

door

Andrea Fortini

geboren op 2 augustus 1976 te Orzinuovi, Italië

Promotor: Prof. dr. A. van Blaaderen
Co-promotor: Dr. M. Dijkstra

This work is part of the research program of the *Stichting voor Fundamenteel Onderzoek der Materie* (FOM), that is financially supported by the *Nederlandse Organisatie voor Wetenschappelijk Onderzoek* (NWO).

Perché la materia di studio sarebbe infinita

Francesco Guccini

Contents

1 Introduction **1**
- 1.1 Soft Condensed Matter . . . 1
- 1.2 Monte Carlo computer simulations . . . 2
- 1.3 Models of colloidal suspensions . . . 3
  - 1.3.1 Hard spheres . . . 3
  - 1.3.2 Charged colloids: DLVO theory . . . 4
  - 1.3.3 Colloid-polymer mixtures . . . 6

2 The wall-fluid interface of hard spheres and AOV colloid-polymer mixtures **11**
- 2.1 Introduction . . . 11
- 2.2 The hard-wall model . . . 12
- 2.3 Overview of interfacial thermodynamics . . . 13
  - 2.3.1 Wall-fluid interfacial tension for the semi-grand canonical ensemble 13
- 2.4 Adsorption at a hard wall from scaled-particle theory . . . 14
- 2.5 Thermodynamic integration of hard-core potentials . . . 16
  - 2.5.1 Step function . . . 17
  - 2.5.2 Triangular function . . . 18
  - 2.5.3 Cut exponential function . . . 18
- 2.6 Simulation details . . . 19
- 2.7 Wall-fluid interfacial tension of hard spheres . . . 19
- 2.8 Wall-fluid interfacial tension of model colloid-polymer mixtures . . . 21
- 2.9 Conclusions . . . 23

3 Hard spheres confined between two hard walls **25**
- 3.1 Introduction . . . 25
- 3.2 Model and Method . . . 27

3.3 Results . . . 28
3.4 Conclusion . . . 32

4 Colloid-polymer mixtures confined between two parallel planar walls 33
4.1 Introduction . . . 33
4.2 Model . . . 35
4.3 Simulation method . . . 35
4.4 Kelvin equation for binary mixtures . . . 38
4.4.1 Constant Polymer Chemical Potential . . . 40
4.4.2 Constant Pressure . . . 40
4.4.3 Normal Path Relation . . . 42
4.5 Results . . . 42
4.5.1 Phase diagrams . . . 44
4.5.2 Structure at coexistence . . . 47
4.5.3 Structure off-coexistence . . . 50
4.5.4 Two dimensional limit . . . 52
4.5.5 Kelvin equation . . . 54
4.6 Conclusions . . . 55

5 Effect of excluded volume interactions on colloid-polymer mixtures 59
5.1 Introduction . . . 59
5.2 Model . . . 60
5.3 Method . . . 62
5.4 Results . . . 64
5.4.1 Bulk phase behaviour and gas-liquid interfacial tension . . . 64
5.4.2 Confined system: Capillary condensation . . . 66
5.5 Conclusions . . . 68

6 Phase behaviour of model charged colloid-polymer mixtures 69
6.1 Introduction . . . 69
6.2 The model . . . 71
6.3 Simulation details . . . 72
6.4 Theory . . . 75
6.4.1 Charged colloids . . . 75
6.4.2 Charged colloid-polymer mixtures . . . 76
6.4.3 Free volume fraction in a charged sphere dispersion . . . 77
6.5 Results . . . 79
6.5.1 Hard spheres . . . 79
6.5.2 Results for model charged colloid-polymer mixtures . . . 81
6.6 Conclusions . . . 87

7 Gas-liquid phase separation in oppositely charged colloids 89
7.1 Introduction . . . 89
7.2 Model . . . 90
7.3 Simulation Methods . . . 91

7.4 Results . . . 93
7.5 Conclusions . . . 99

8 Brownian dynamics simulations of phase-separating colloid-polymer mixtures 101
8.1 Introduction . . . 101
8.2 Model and Method . . . 103
8.3 Results . . . 104
8.4 Conclusions . . . 109

Bibliography 113

Summary 123

Samenvatting 127

Publications 129

Curriculum 131

Dankwoord 132

1

Introduction

1.1 Soft Condensed Matter

The term soft condensed matter characterises a class of materials that are very common in everyday life. Glues, paints, soaps, viruses, bacteria, blood, and many food dispersions like milk, mayonnaise and ice creams are all classified as soft matter systems. In this thesis, we will concentrate on a particular type of soft matter, referred to as colloidal suspensions, in which solid particles (colloids) with sizes between 10 nanometers to 10 micrometers are suspended in a liquid solvent. Due to the collisions of solvent molecules, the colloids experience random pressure fluctuations that cause an irregular random walk of the particles through the solvent, known as Brownian motion. The colloidal particles are then able to explore the whole configurational space, and eventually reach the equilibrium configuration that minimises the free energy. This ability of colloidal systems to *self-assemble* into a particular configuration can be described using the tools of statistical physics, with colloidal particles playing the role of atoms or molecules. However, since the associated relevant time and length scales are much larger than in atomic and molecular systems, direct experimental observations using advanced microscopy techniques enable the study of many interesting physical phenomena in real space and real time. Since the first experiments of Perrin [1] at the beginning of last century, colloids have been used as model systems to study fundamental problems of statistical physics, like crystallisation [2–6], gas-liquid separation [7, 8], nucleation [9, 10], capillary waves at the gas-liquid interface [11, 12], and the wetting of solid substrates [13, 14]. Nonetheless, colloids are more than just model systems for atomic and molecular matter. In fact, the properties of colloidal suspensions can be changed in such a way that both the strength and the range of the interactions can be controlled independently, giving rise to complex and fascinating phase behaviours, with no counterpart in the atomic world. As an example of parameters that can be changed to control the phase behaviour of colloidal suspensions we mention the shape and the density of colloids, the salt concentration, or the size and density of added polymers. While these processes are sometimes difficult to control precisely in an experiment, simulations are characterised by well defined parameters, and hence repre-

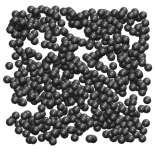

sent an ideal tool to explore the equilibrium properties of colloidal suspensions. Furthermore, computer simulations bridge the distance between the complexity of real experiments, and the approximate descriptions of theories.

The scope of this thesis is to analyse the phase behaviour of colloidal suspensions with computer simulations. In the rest of this introductory chapter we will briefly introduce the simulation technique, and the models for colloidal suspensions used in this thesis. In chapter 2, we will show results for the interfacial free energy of model colloidal suspensions in contact with a single wall. In chapters 3, 4, and 5 we will analyse the effect of confinement between two walls on the equilibrium phase behaviour of hard spheres and colloid-polymer mixtures. Chapters 6, and 7 are dedicated to the bulk phase behaviour of charged colloidal suspensions. In chapter 8, we analyse non-equilibrium behaviour of colloids with short range attractive interactions.

1.2 Monte Carlo computer simulations

In this section, without any pretence to completeness, we give an introduction of the Metropolis Monte Carlo (MC) method that is used throughout the thesis. For a complete introduction to the subject of molecular simulations we refer the reader to the references [15–18]. In fact, the scope of this section is to prepare the reader to the more detailed simulation sections of the following chapters where advanced techniques for calculating the free energies will be introduced.

The thermodynamics of a classical system, with constant number of particles N, in a constant volume V, at fixed temperature T (canonical ensemble) can be derived from the Helmholtz free energy

$$F = -k_B T \log Q \,, \tag{1.1}$$

with the partition function

$$Q = \frac{1}{h^{3N} N!} \int d\vec{p}^N d\vec{r}^N \exp[-H(\vec{r}^N, \vec{p}^N)/k_B T] \,, \tag{1.2}$$

where h is the Planck constant, k_B is the Boltzmann constant, $\vec{r}$ stands for the position of the particles, $\vec{p}$ stands for the momenta, and $H(\vec{r}^N, \vec{p}^N)$ is the Hamiltonian of the system. The knowledge of the free energy is sufficient to determine all thermodynamic properties, but unfortunately its direct computation is prohibited by the huge number of configurations that must be taken into account. Already for small systems the number of configurations in the integral (1.2) would require a computational time many orders of magnitude larger than the current universe lifetime. In principle, the same problem exists for the computation of the thermal average of an observable A

$$\langle A \rangle = \frac{\int d\vec{p}^N d\vec{r}^N A(\vec{r}^N, \vec{p}^N) \exp[-H(\vec{r}^N, \vec{p}^N)/k_B T]}{\int d\vec{p}^N d\vec{r}^N \exp[-H(\vec{r}^N, \vec{p}^N)/k_B T]} \,. \tag{1.3}$$

The direct computation of the integrals in Eq. (1.3) is not possible due to the huge number of configurations to be evaluated in the integral. Nevertheless, Metropolis et al. [19] devised an indirect method to compute the average $\langle A \rangle$. The basic idea behind what is now

called Metropolis Monte Carlo algorithm is to randomly generate configurations that obey the Boltzmann distribution, and sample the observable A for a number of these configurations. For a simulation in the canonical ensemble, a run is started from a configuration of N particles in a box of volume V. The system must have a well defined potential energy U. A particle i is selected at random. Its position r_i is then changed by a random amount Δr. The difference in energy $\Delta U = U(r_i + \Delta r) - U(r_i)$ between the new and old configuration determines if the trial move is accepted or not. The new configuration is accepted, i.e. the particle is moved to the new position, if $\Delta U < 0$, or with a probability $\exp(-\Delta U / k_b T)$ if the energy difference is positive. If the move is rejected the particle i stays in the old position r_i. The trial move is repeated in a cycle. Once in a while, the value A_k of the observable A is computed for the instantaneous configuration k. The procedure ensures that the average over M independent and uncorrelated configurations

$$\langle A \rangle = \sum_{k=1}^{M} \frac{A_k}{M}, \tag{1.4}$$

is equal to the result of the average (1.3). With the MC algorithm we can estimate the average value of an equilibrium observable and compare it with experiments, furthermore MC simulations are not restricted to the canonical ensemble, and other quantities, like pressure or chemical potential, can be kept fixed during the simulation.

1.3 Models of colloidal suspensions

1.3.1 Hard spheres

The first model for colloidal particles that we consider is that of hard spheres. As its name suggests, in this model we consider perfect spheres whose interaction is zero except when two spheres overlap, in which case the interaction is infinity. The sphere-sphere potential then reads

$$v_{ij}(R_{ij}) = \begin{cases} \infty & \text{if } R_{ij} < \sigma \\ 0 & \text{otherwise} \end{cases}, \tag{1.5}$$

where $R_{ij} = |\vec{R}_i - \vec{R}_j|$ is the distance between two colloidal particles, with $\vec{R}_i$ the position of the centre-of-mass of colloid i, and σ the diameter of the sphere. The variable we will use to describe the concentration of hard spheres is the packing fraction (also called volume fraction) defined as $\eta = \pi/6\sigma^3 N/V$, with N the number of particles in a system with volume V. The equilibrium phase diagram of hard spheres is well understood. The fluid phase is stable for packing fractions $\eta < 0.4915$. Fluid and crystal phases coexist between $0.4915 < \eta < 0.5428$. While for packing fractions $\eta > 0.5428$ the f.c.c.[1] crystal phase is stable [2, 4]. Since the interaction energy of hard spheres is always zero, the crystal phase is stabilised by entropy only, spheres in the crystal phase have more free volume than in a disordered phase at the same density. Hard spheres contradict the notion that entropy always brings more disorder!

[1] The f.c.c phase is stable with respect to the h.c.p phase [20, 21], although recently it was suggested that the h.c.p phase is more stable at nearly close packed densities [22].

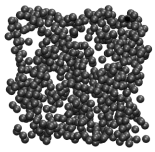

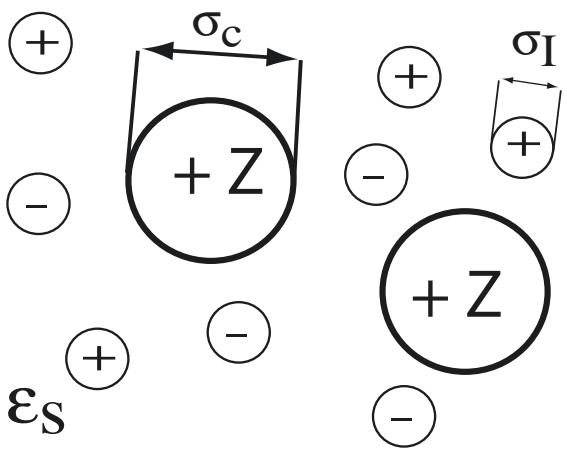

Figure 1.1: Illustration of the primitive model for charged colloids with diameter σ in a bath of microions with diameter σ_I in a solvent with dielectric constant ϵ_s.

1.3.2 Charged colloids: DLVO theory

Extension to the simple hard-sphere model must be made when colloidal particles carry charge. The interaction between charged spherical colloids of diameter σ_c with charge number Z can be modeled by a hard core plus a Coulombic interaction

$$u(R_{ij})/k_BT = \begin{cases} \infty & R_{ij} \leq \sigma_c \\ \frac{Z^2\lambda_B}{R_{ij}} & \text{otherwise} \end{cases}, \tag{1.6}$$

where $R_{ij} = |\vec{R}_i - \vec{R}_j|$ is the distance between colloid i and colloid j, $\lambda_B = e^2/\epsilon_s k_B T$ is the Bjerrum length, ϵ_s is the dielectric constant of the solvent, and e is the elementary charge. This interaction is usually screened by the addition of coions and counterions (salt) with diameter σ_I. The interaction potential between microions with charge numbers ± 1 is

$$u(r_{ij})/k_BT = \begin{cases} \infty & r_{ij} \leq \sigma_I \\ \pm\frac{\lambda_B}{r_{ij}} & \text{otherwise} \end{cases}, \tag{1.7}$$

where $r_{ij} = |\vec{r}_i - \vec{r}_j|$ is the distance between microion i and microion j, and the interaction potential between microions and colloids reads

$$u(|\vec{R}_i - \vec{r}_j|)/k_BT = \begin{cases} \infty & |\vec{R}_i - \vec{r}_j| \leq (\sigma_c + \sigma_I)/2 \\ \pm\frac{Z\lambda_B}{|\vec{R}_i - \vec{r}_j|} & \text{otherwise} \end{cases}. \tag{1.8}$$

The equations (1.6), (1.7) and (1.8) form the restricted primitive model (RPM) for charged colloidal suspensions. Unfortunately, simulations for this model are often difficult in many regions of the parameter space. For this reason, we will employ a coarse-grained version

of this model that is due to Derjaguin and Landau [23], and Verwey and Overbeek [24]. In the Derjaguin-Landau-Verwey-Overbeek (DLVO) theory, a single sphere carrying charge Z is suspended in a solvent with dielectric constant ϵ_s, and point-like co- and counter-ions with number density far from the sphere equal to n_s. The density profile of microions is given by the Boltzmann distribution

$$\begin{aligned} n_-(r) &= n_s \exp(e\phi(r)/k_B T) \,, \\ n_+(r) &= n_s \exp(-e\phi(r)/k_B T) \,, \end{aligned} \tag{1.9}$$

where $n_-(r)$ and $n_+(r)$ indicate the number density of counter- and coions respectively. The electric potential ϕ is determined by the net charge density $\rho(r) = e(n_+(r) - n_-(r))$ through the Poisson equation

$$\nabla^2\phi = -4\pi\frac{\rho(r)}{\epsilon_s} \,. \tag{1.10}$$

Hence, the combination of equations (1.9) and (1.10) leads to the Poisson-Boltzmann equation

$$\nabla^2\phi = 8\pi\frac{n_s}{\epsilon_s}\sinh(e\phi(r)/k_B T) \,. \tag{1.11}$$

The solution of this equation can be very complicated to obtain, but if the potential ϕ is small, it is commonplace to apply the Debye-Hückel approximation that consists in linearizing the hyperbolic sine of Eq. (1.11)

$$\frac{e}{k_B T}\nabla^2\phi = \kappa^2(e\phi(r)/k_B T) \,, \tag{1.12}$$

where we defined the inverse Debye screening length $\kappa = \sqrt{(8\pi\lambda_B n_s)}$. The solution of the linearized Poisson-Boltzmann equation is easily obtained and reads

$$\phi(r) = \frac{Z\lambda_B}{\sigma(1+\kappa\sigma/2)}\frac{\exp[-\kappa(r-\sigma)]}{r/\sigma} \,. \tag{1.13}$$

The interaction potential between two charged spheres within the DLVO theory is then derived assuming that the distribution of ions around each sphere is not disturbed by the presence of the other one. The effective pair potential between the two charged spheres carrying the same charge number Z is then given by

$$u(R_{ij})/k_B T = \begin{cases} \infty & R_{ij} \le \sigma_c \\ \frac{Z^2}{(1+\kappa\sigma/2)^2}\frac{\lambda_B}{\sigma}\frac{\exp[-\kappa(R_{ij}-\sigma)]}{R_{ij}/\sigma} & \text{otherwise} \end{cases} \,, \tag{1.14}$$

where R_{ij} is the distance between spheres i and j. Clearly, we recover the hard-sphere interaction, and hence its phase behaviour, in the high-salt limit of $\kappa\sigma \to \infty$. For decreasing $\kappa\sigma$ the liquid-face-centered-cubic (f.c.c.) coexistence region moves towards smaller values of the packing fraction [25, 26]. At intermediate values of $\kappa\sigma$ the stable solid phase transforms from the f.c.c. to a body-centered-cubic (b.c.c.) phase, and the coexistence region moves back to higher packing fractions.

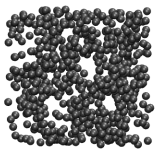

1.3.3 Colloid-polymer mixtures

Colloid-colloid interactions can be changed by adding a second component to the suspension. In this section we treat the case of added non-adsorbing polymers. Although the interaction can be in general complicated, we consider only the case of flexible polymer chains in a "good solvent" condition where the interactions between colloid and polymer are hard, and the excluded volume interactions between polymer chains are small. Provided the size and the number of polymers are sufficiently high, such mixtures can phase-separate into a *colloidal gas* phase that is poor in colloids and rich in polymers, and a *colloidal liquid* phase that is rich in colloids and poor in polymers. The mechanism behind this demixing transition is of entropic origin and is due to the so-called depletion effect. In Fig. 1.2(a), we illustrate the mixture of spherical colloids and polymer chains. Around each colloid there is a depletion region prohibited to the polymers due to the hard-core interaction (the chains cannot penetrate the colloids). If two colloids approach each other, so that two depletion zones overlap (light grey region in Fig. 1.2(a)), there is an increase in free volume for the polymer chains, i.e. an increase in entropy [27–30]. The increase in entropy can be described by an attractive interaction between colloidal particles. This effective attraction can also be viewed as arising from an unbalanced osmotic pressure pushing the colloids together as polymer coils are excluded from the depletion zones between the colloids.

Adding non-adsorbing polymer allows modification of the range and strength of attraction of the effective interactions between the colloidal particles. Adjusting the range of the attraction enables manipulating the topology of the phase diagram of a colloid-polymer mixture [8, 30–34]. Both the nature of the demixed phases as well as the colloid and polymer concentrations at which demixing takes place depend on the range of attraction [8, 35]. Industrially, it is relevant to understand the phase behaviour of colloid-polymer mixtures because colloidal particles and polymer chains are often jointly present in various products, such as food dispersions [36, 37]. A particularly simple model for colloid-polymer mixtures was proposed independently by Asakura and Oosawa [27, 38] and by Vrij [28], and is often referred to as the Asakura-Oosawa-Vrij (AOV) model.

Asakura-Oosawa-Vrij model

In this model, colloids and polymers interact via a hard-sphere-like potential, as the polymers are excluded from a centre-of-mass distance $(\sigma_c + \sigma_p)/2$ from the colloids, where $\sigma_p = 2R_g$, and R_g is the radius of gyration of the polymer coils. This so-called Asakura-Oosawa-Vrij (AOV) model [27, 28, 38, 39] is defined by the pair potentials

$$v_{cc}(R_{ij}) = \begin{cases} \infty & \text{if } R_{ij} < \sigma_c \\ 0 & \text{otherwise,} \end{cases} \tag{1.15}$$

where $R_{ij} = |\vec{R}_i - \vec{R}_j|$ is the distance between two colloidal particles, with $\vec{R}_i$ the position of the centre-of-mass of colloid i,

$$v_{pp}(r_{ij}) = 0, \tag{1.16}$$

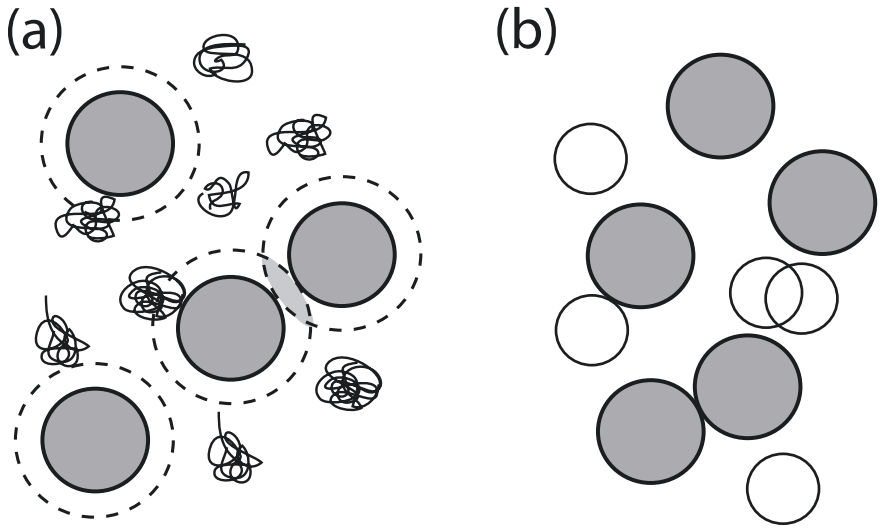

Figure 1.2: a) Illustration of a mixture of spherical colloids and polymer coils. Depletion zones (dashed lines) are inaccessible to polymers. Overlapping depletion zones between two colloids are indicated in light grey. b) Illustration of the AOV model for colloid (dark circles) and polymer (open circles) mixtures.

where $r_{ij} = |\vec{r}_i - \vec{r}_j|$ is the distance between two polymers, with $\vec{r}_i$ the position of the centre-of-mass of polymer i and

$$v_{\rm cp}(|\vec{R}_i - \vec{r}_j|) = \begin{cases} \infty & \text{if } |\vec{R}_i - \vec{r}_j| < (\sigma_{\rm c} + \sigma_{\rm p})/2 \\ 0 & \text{otherwise,} \end{cases} \tag{1.17}$$

where $|\vec{R}_i - \vec{r}_j|$ is the distance between colloid i and polymer j. The AOV model is illustrated in Fig. 1.2(b).

The size ratio $q = \sigma_{\rm p}/\sigma_{\rm c}$ is a geometric parameter that controls the range of the effective depletion interaction between the colloids. We denote the packing fraction by $\eta_k = (\pi\sigma_k^3 N_k)/(6V)$, with N_k the number of particles of species k in a volume V, and $k = {\rm c,p}$ for colloids and polymers, respectively. As alternatives to $\eta_{\rm p}$, we use as a thermodynamic variable the polymer fugacity $z_{\rm p}$, or the polymer reservoir packing fraction $\eta_{\rm p}^{\rm r}$ that satisfies the (ideal gas) relation

$$\eta_{\rm p}^{\rm r} = \frac{\pi}{6}\sigma_{\rm p}^3 z_{\rm p}. \tag{1.18}$$

Effective potential

Even within the context of the highly simplified AOV model, it is often more convenient to adopt a more coarse-grained view of the binary mixture by ignoring the degrees of freedom of the polymer coils and using polymer-mediated effective interactions between the

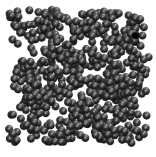

colloids. When there is a large size asymmetry between colloids and polymer it is possible to integrate out the degrees of freedom of the polymer coils, and map the binary mixture of colloids and polymers onto an effective one-component system interacting with an effective one-component Hamiltonian [40–43]. This effective Hamiltonian consists of zero-body, one-body, two-body, and higher-body terms. We derive an exact expression for the polymer-mediated effective pair potential or depletion potential. The potential part of the Hamiltonian is the sum of three interaction terms $H = H_{\rm cc} + H_{\rm cp} + H_{\rm pp}$, where

$$\begin{aligned} H_{\rm cc} &= \sum_{i<j} v_{\rm cc}(R_{ij}) \,, \\ H_{\rm cp} &= \sum_{i} \sum_{j} v_{\rm cp}(|\vec{R}_i - \vec{r}_j|) \,, \\ H_{\rm pp} &= \sum_{i<j} v_{\rm pp}(r_{ij}) \,. \end{aligned} \tag{1.19}$$

It is convenient to consider the system in the (N_c, V, z_p, T) ensemble, in which the fugacity $z_p = \Lambda_p^{-3} \exp(\beta\mu_p)$ of the polymer coils is fixed. Here μ_p denotes the chemical potential and $\beta = 1/k_B T$. The thermodynamic potential $F(N_c, V, z_p, T)$ can be written as

$$\exp(-\beta F) = \sum_{N_p=0}^{\infty} \frac{z_p^{N_p}}{N_c! N_p! \Lambda_c^{3N_c}} \int_V d\vec{R}^{N_c} \int_V d\vec{r}^{N_p} \exp[-\beta(H_{\rm cc} + H_{\rm cp})] \,. \tag{1.20}$$

We define an effective Hamiltonian $H_{\rm eff} = H_{\rm cc} + \Omega$ such that

$$\exp(-\beta F) = \frac{1}{N_c! \Lambda_c^{3N_c}} \int_V d\vec{R}^{N_c} \exp[-\beta H_{\rm eff}] \,. \tag{1.21}$$

The thermodynamic potential Ω is then

$$\begin{aligned} \exp(-\beta\Omega) &= \sum_{N_p=0}^{\infty} \frac{z_p^{N_p}}{N_p!} \int_V d\vec{r}^{N_p} \exp[-\beta(H_{\rm cp})] \\ &= \exp\left[z_p \int_V d\vec{r} \exp\left[-\beta \sum_{i=0}^{N_c} v_{\rm cp}(|\vec{R}_i - \vec{r}_j|) \right] \right] \,. \end{aligned} \tag{1.22}$$

Using standard diagrammatic techniques [44] $\beta\Omega$ is expanded in n-body interaction terms, with n=0…N_c

$$\beta\Omega = \sum_{n=0}^{N_c} \beta\Omega_n \,. \tag{1.23}$$

It is possible to give explicit expressions for $\beta\Omega_n$ with n=0, 1, and 2. In particular, the zero-body term reads

$$\beta\Omega_0 = -z_p V,$$

which corresponds to the grand-potential of a pure system of polymer at fugacity z_p in a volume V. The one-body term is

$$\beta\Omega_1 = z_p\eta_c(1+q)^3V,$$

and is related to the volume excluded to a polymer by a single colloid. The pair interaction term reads

$$\beta\Omega_2 = \sum_{i<j}^{N_c} U_{\rm dep}(R_{ij}),$$

with the depletion potential [28, 38, 39, 42]

$$\beta U_{\rm dep}(R_{ij}) = \begin{cases} -\eta_p^r \frac{(1+q)^3}{q^3}\left[1 - \frac{3R_{ij}}{2(1+q)\sigma_c} + \frac{R_{ij}^3}{2(1+q)^3\sigma_c^3}\right] & \sigma_c < R_{ij} < \sigma_c + \sigma_p \\ 0 & R_{ij} > \sigma_c + \sigma_p \end{cases} . \tag{1.24}$$

This Asakura-Oosawa pair potential describes an effective attraction whose depth increases linearly with the polymer packing fraction in the corresponding reservoir η_p^r. The range of the potential is given by σ_p. Terms with $n > 2$, i.e. three- and higher-body interactions, are often neglected. However, it is important to note that for sufficiently large polymer coils, effective three- and higher-body interactions can not always be neglected. More precisely, we expect an increasing number of higher-body interactions to become non-zero when q increases. It was shown [14] that the many-body character of the polymer-mediated effective interactions between the colloids yields a bulk phase diagram that differs substantially from those found for pair-wise simple fluids. However, for size ratios $q < 0.1547$, three- and many-body interactions are identical to zero and the mapping of the binary mixture onto the effective one-component Hamiltonian based on pair-wise additive effective potentials is exact.

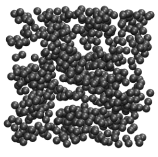

2

The wall-fluid interface of hard spheres and AOV colloid-polymer mixtures

In this chapter we perform a study of the interfacial properties of a model suspension of hard-sphere colloids with diameter σ_c and with the addition of non-adsorbing polymer coils with diameter σ_p, described by the AOV model. We obtain from simulations the wall-fluid interfacial free energy, γ_{wf}, for size ratios $q = \sigma_p/\sigma_c = 0.6$ and 1, using a novel thermodynamic integration method for hard-core potentials, and we study the (excess) adsorption of colloids, Γ_c, and of polymers, Γ_p, at a hard wall. Good agreement is found between the simulation results and those from density functional theory, while the results from scaled particle theory deviate quantitatively but reproduce some essential features.

2.1 Introduction

In Sec. 1.3.3 we explained the origin of the depletion attraction in mixtures of colloids and polymers. When two colloids are close enough, the free volume available to polymers increases, leading to an increase in entropy. Similarly, polymers are excluded from the hard wall, and a colloid close to the wall corresponds to a configuration of higher entropy (see Fig. 2.1(a)). Around each colloid and at the wall we have depletion layers excluded to the polymer chains (dashed lines). When the depletion layers of the wall and a colloid overlap, there is an increase of free volume for the polymer chains, and consequently an increase of entropy. This mechanism can be described by an effective depletion interaction between a colloidal particle and a planar hard wall. The wall-fluid interfacial tension of a hard-sphere fluid in contact with a planar hard wall was calculated by Heni and Löwen [45] using a thermodynamic integration procedure along a path that corresponds to the growth of a wall in a bulk system. Here, we propose a thermodynamic integration approach similar in spirit, to determine the free energy of hard spheres and AOV colloid-polymer mixtures in contact with a planar hard wall, from which we derive the wall-fluid interfacial tension. In addition, we studied the (excess) adsorption of colloids, Γ_c, and of polymers, Γ_p, at the hard wall. The simulation results are checked against the predictions of density functional the-

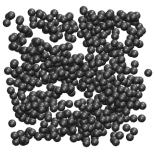

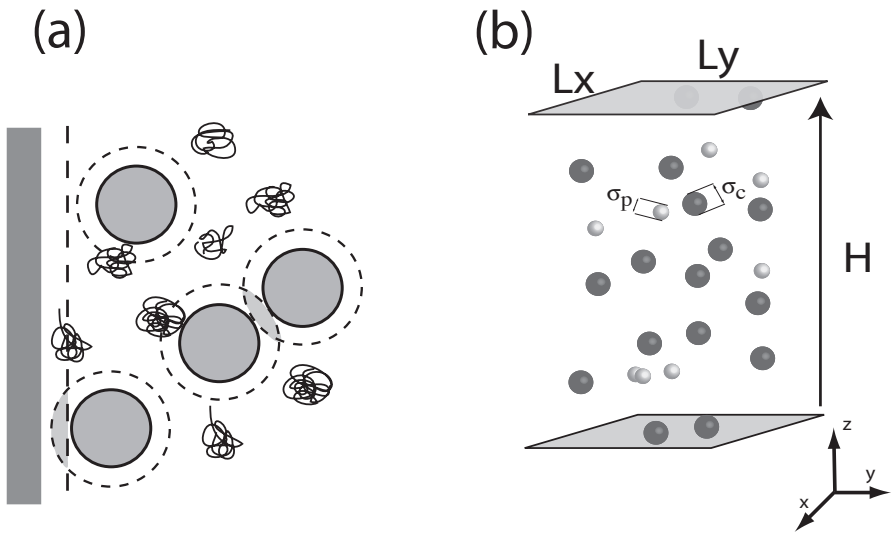

Figure 2.1: (a) Illustration of a mixture of spherical colloids and polymer coils in contact with a hard wall impenetrable to both species. Depletion zones (dashed lines) are inaccessible to polymers. Overlapping depletion zones (light grey) are indicated in two cases, that between two colloids, and between a colloid and a hard wall. (b) Schematic representation of the AOV model colloid-polymer mixtures in the simulation box with two hard walls in the z direction.

ory (DFT) [46, 47] based on an extension of the Rosenfeld functional [48], and of a scaled particle theory (SPT) [47] based on the free volume theory [30]. Technical details about the DFT implementation that also apply to the present study are given in Ref. [49].

2.2 The hard-wall model

Since, it is not possible to simulate a semi-infinite system, we performed simulations in a box with periodic boundary conditions in the x and y directions and two impenetrable hard walls in the z direction (Fig. 2.1(b)). If the separation distance H is large enough capillary effects are negligible. The wall-particle potential acting on particles of species $k = c, p$ reads

$$v_{wk}(z_{k,i}) = \begin{cases} 0 & \text{if } \sigma_k/2 < z_{k,i} < H - \sigma_k/2 \\ \infty & \text{otherwise} \end{cases} , \tag{2.1}$$

where $z_{k,i}$ is the z-coordinate of particle i of species k, and H is the separation distance between the two walls.

2.3 Overview of interfacial thermodynamics

Generally, the interfacial tension in an inhomogeneous system is the grand potential per unit area needed to create an interface in an initially uniform bulk system at fixed chemical potential of colloids, μ_c, and polymers, μ_p, and fixed volume V and temperature T. The grand potential for a bulk mixture of colloids and polymers reads

$$\Omega^{\text{bulk}}(\mu_c, \mu_p, V, T) = -p(\mu_c, \mu_p, T)V, \tag{2.2}$$

where p is the bulk pressure. The system in contact with an interface possesses the grand potential

$$\Omega(\mu_c, \mu_p, V, T, A) = -p(\mu_c, \mu_p, T)V + \gamma(\mu_c, \mu_p, T)A, \tag{2.3}$$

where A is the area of the interface and $\gamma(\mu_c, \mu_p, T)$ is the interfacial tension, which can hence be expressed as

$$\gamma = \frac{\Omega(\mu_c, \mu_p, V, T, A) - \Omega^{\text{bulk}}(\mu_c, \mu_p, V, T)}{A}. \tag{2.4}$$

Besides the liquid-gas interface, where $\gamma = \gamma_{\text{lg}}$, Eqs. (2.2), (2.3), and (2.4) apply also for a fluid adsorbed between two parallel plates (walls), where $\gamma = \gamma_{\text{wf}}$, provided that the wall separation is sufficiently large [50, 51], and that the area A is equal to the total area of the two plates, $A = 2L^2$, with L the linear dimension of the plates. At fixed chemical potentials the number of particles in the inhomogeneous system, N_c and N_p, of colloids and polymers, respectively, will be in general different from those in the bulk, N_c^{bulk} and N_p^{bulk}. The excess number of colloids and polymers per unit area, i.e. the adsorptions Γ_c and Γ_p, respectively, are defined as

$$\Gamma_c(\mu_c, \mu_p, T) = \frac{N_c - N_c^{\text{bulk}}}{A}, \tag{2.5}$$

$$\Gamma_p(\mu_c, \mu_p, T) = \frac{N_p - N_p^{\text{bulk}}}{A}. \tag{2.6}$$

The grand potentials (2.2) and (2.3) in differential form read

$$d\Omega^{\text{bulk}}(\mu_c, \mu_p, V, T) = -N_c^{\text{bulk}} d\mu_c - N_p^{\text{bulk}} d\mu_p - pdV - S^{\text{bulk}} dT\,, \tag{2.7}$$

$$d\Omega(\mu_c, \mu_p, V, T, A) = -N_c d\mu_c - N_p d\mu_p - pdV - SdT + \gamma dA\,. \tag{2.8}$$

Using Eqs. (2.7) and (2.8) and Eq. (2.4) in differential form, it is straightforward to show [52] that the adsorptions are related to the interfacial tension through

$$\Gamma_c = -\left(\frac{\partial \gamma}{\partial \mu_c}\right)_{\mu_p, T} \quad \text{and} \quad \Gamma_p = -\left(\frac{\partial \gamma}{\partial \mu_p}\right)_{\mu_c, T}. \tag{2.9}$$

2.3.1 Wall-fluid interfacial tension for the semi-grand canonical ensemble

To determine, from simulations, the wall-fluid tension γ_{wf} of the AOV model we should apply equation (2.4), as is manifest in the grand canonical ensemble, i.e. for constant colloid

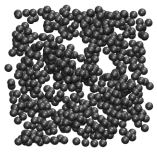

and polymer fugacities. However, in our simulation it is more convenient to use the semi-grand canonical ensemble [1] fixing the number of colloids and the fugacity of the polymers. The reason is twofold. First the interfacial tension as a function of the fugacity of polymers can be directly compared to the DFT results of Ref. [47]. Second, fixing the number of colloids instead of their fugacity allow us to efficiently study state points with high packing fractions of colloids; generally grand ensemble simulations are difficult to perform at high densities due to small particle insertion probabilities. To compute the tension we have to recast Eq. (2.4) in a way that is consistent with the semi-grand canonical ensemble. The grand potentials for the bulk and the inhomogeneous system are related to the corresponding Helmholtz free energies via a Legendre transformation,

$$\Omega^{\text{bulk}}(\mu_c,\mu_p,V,T) = F^{\text{bulk}}(N_c^{\text{bulk}},N_p^{\text{bulk}},V,T)-\mu_c N_c^{\text{bulk}}-\mu_p N_p^{\text{bulk}}, \tag{2.10}$$

$$\Omega(\mu_c,\mu_p,V,T,A) = F(N_c,N_p,V,T,A)-\mu_c N_c-\mu_p N_p. \tag{2.11}$$

We substitute Eqs. (2.10) and (2.11) in Eq. (2.4) to obtain

$$\gamma = \frac{F(N_c,N_p)-F^{\text{bulk}}(N_c^{\text{bulk}},N_p^{\text{bulk}})}{A}-\mu_c\Gamma_c-\mu_p\Gamma_p, \tag{2.12}$$

where we omitted the dependence on the variables V,T,μ_c, and μ_p in the notation. Note that the tension is not only the difference of the Helmholtz free energies, but additional terms, $\mu_c\Gamma_c$ and $\mu_p\Gamma_p$, arise in Eq. (2.12). One can further simplify by Taylor expanding $F(N_c,N_p,V,T,A)$ around N_c^{bulk}:

$$F(N_c,N_p,V,T,A) = F(N_c^{\text{bulk}},N_p,V,T,A)+\frac{\partial F}{\partial N_c}(N_c-N_c^{\text{bulk}})+\mathcal{O}((N_c-N_c^{\text{bulk}})^2). \tag{2.13}$$

Keeping only the first order term, one can approximate the interfacial tension as

$$\gamma \simeq \frac{F(N_c^{\text{bulk}},N_p,V,T,A)-F^{\text{bulk}}(N_c^{\text{bulk}},N_p^{\text{bulk}},V,T)}{A}-\mu_p\Gamma_p. \tag{2.14}$$

The same approximation was employed in Ref. [45] (using $N_p=0$ and $N_p^{\text{bulk}}=0$) to calculate the interfacial free energy of hard spheres in contact with a planar hard wall. To compute the wall tension, we need to perform *two* free energy calculations, one for the bulk and one for the inhomogeneous system.

2.4 Adsorption at a hard wall from scaled-particle theory

For a system of hard spheres the scaled particle theory [53, 54] describes quite accurately the pressure p, the hard wall-fluid interfacial tension γ_{hs}, and the (excess) adsorption Γ_{hs}, given through the expressions

$$\frac{\beta p}{\rho_c} = \frac{1+\eta_c+\eta_c^2}{(1-\eta_c)^3}, \tag{2.15}$$

[1] In the literature, the name semi-grand canonical ensemble is sometimes used to indicate a different ensemble. Namely, a canonical ensemble where the composition can change at fixed chemical potential difference.

$$\beta\hat{\gamma}_{\rm hs}\sigma_c^2 = -9\eta_c^2\frac{(1+\eta_c)}{2\pi(1-\eta_c)^3}, \tag{2.16}$$

$$\Gamma_{\rm hs}\sigma_c^2 = \frac{9\eta_c^2}{\pi(1+2\eta_c)} - \frac{3\eta_c}{\pi}. \tag{2.17}$$

The total wall-fluid tension is defined as

$$\beta\gamma_{\rm hs}\sigma_c^2 = \beta p/2 + \beta\hat{\gamma}_{\rm hs}\sigma_c^2\,. \tag{2.18}$$

In particular, Eq. (2.18) with the SPT pressure (2.15) was shown to compare well with simulation [55] and DFT [56] results.

Recently, an SPT expression for the wall-fluid tension of AOV model colloid-polymer mixtures was derived by Wessels et al. [47] using the bulk free energy for a ternary mixture obtained from free volume theory [30] as an input, and taking the limit of vanishing concentration and infinite size of the third component. Their expression reads

$$\beta\gamma_{\rm wf}\sigma_c^2 = \beta\gamma_{\rm hs}\sigma_c^2 + \eta_p^r f(\eta_c), \tag{2.19}$$

where $f(\eta_c) = 3\alpha(\eta_c)/(q^2\pi)[1+(1+3q+q^2)\tau+(3q+4q^2)\tau^2+3q^2\tau^3]$, $\tau = \eta_c/(1-\eta_c)$ and $\beta\gamma_{\rm hs}\sigma_c^2$ is given by equation (2.16) and (2.18). The polymer free volume is given by the scaled particle theory as $\alpha(\eta_c) = (1-\eta_c)\exp(-(3q+3q^2+q^3)\tau-(9q^2/2+3q^3)\tau^2-3q^3\tau^3)$. Results for $\gamma_{\rm wf}$ from equation (2.19) were found in Ref. [47] to compare reasonably well with those from full numerical density functional calculations. In the next section we will compare these approaches against our simulation data.

In addition, we derive an SPT expression for the adsorption of the AOV model at a hard wall starting from equation (2.19) and building derivatives according to (2.9). The colloid chemical potential obtained from the free volume theory [30] is

$$\beta\mu_c = \beta\mu_{\rm hs}(\eta_c) - \eta_p^r\frac{\alpha'}{q^3}, \tag{2.20}$$

where $\beta\mu_{\rm hs}(\eta_c) = \eta_c(14-13\eta_c+5\eta_c^2)/(2(1-\eta_c)^3) - \log(1-\eta_c) + \log(6\eta_c/\pi)$ is the SPT expression of the chemical potential of a system of pure hard spheres at packing fraction η_c and $\alpha' = \partial\alpha/\partial\eta_c$. We compute the colloidal adsorption using equation (2.9)

$$\Gamma_c\sigma_c^2 = -\frac{\partial\beta\gamma_{\rm wf}(\mu_c,\mu_p)\sigma_c^2}{\partial\beta\mu_c} = -\frac{\partial\beta\gamma_{\rm wf}(\eta_c,\mu_p)\sigma_c^2}{\partial\eta_c}\frac{\partial\eta_c}{\partial\beta\mu_c}, \tag{2.21}$$

where

$$\frac{\partial\eta_c(\mu_c,\mu_p)}{\partial\beta\mu_c} = \left(\frac{\partial\beta\mu_c(\eta_c,\mu_p)}{\partial\eta_c}\right)^{-1}, \tag{2.22}$$

is computed using equation (2.20). The final expression reads

$$\Gamma_c\sigma_c^2 = \Gamma_{\rm hs}\sigma_c^2\left(\frac{1+\eta_p^r\frac{f'}{\beta\gamma'_{\rm hs}\sigma_c^2}}{1-\eta_p^r\frac{\alpha''}{\beta\mu'_{\rm hs}q^3}}\right), \tag{2.23}$$

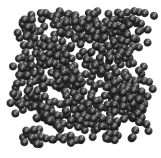

where $f^{'} = \partial f/\partial \eta_c$, $\gamma^{'}_{\rm hs} = \partial \gamma_{\rm hs}/\partial \eta_c$, $\mu^{'}_{\rm hs} = \partial \mu_{\rm hs}/\partial \eta_c$ and $\alpha^{''} = \partial^2 \alpha/\partial \eta_c^2$. We note that the hard-sphere limit is obtained correctly for $\eta_p^r = 0$. We also calculate the polymer adsorption

$$\Gamma_p \sigma_c^2 = -\frac{\partial \beta \gamma_{\rm wf}(\eta_c, \mu_p)\sigma_c^2}{\partial \beta \mu_p} = -\eta_p^r f - \left(\frac{\partial \beta \gamma_{\rm hs}(\eta_c)\sigma_c^2}{\partial \eta_c} + \eta_p^r \frac{\partial f(\eta_c)}{\partial \eta_c} \right) \frac{\partial \eta_c}{\partial \beta \mu_p}. \tag{2.24}$$

Rewriting Eq. (2.20) as

$$\eta_p^r = \frac{\beta \mu_{\rm hs}(\eta_c) - \beta \mu_c}{\alpha^{'}} q^3, \tag{2.25}$$

we arrive at

$$\frac{\partial \eta_c}{\partial \beta \mu_p} = \eta_p^r \left(\frac{\partial \eta_p^r}{\partial \eta_c} \right)^{-1} = \frac{\eta_p^r \alpha'}{q^3 \beta \mu'_{\rm hs} - \eta_p^r \alpha^{''}}. \tag{2.26}$$

The final expression then reads

$$\Gamma_p(\eta_c)\sigma_c^2 = -(\beta \gamma_{\rm wf} - \beta \gamma_{\rm hs})\sigma_c^2 + \eta_p^r \frac{\alpha^{'}}{q^3} \Gamma_c(\eta_c)\sigma_c^2. \tag{2.27}$$

2.5 Thermodynamic integration of hard-core potentials

As explained in section 1.2 the free energy cannot be measured directly in a Monte Carlo simulation. However, there exists indirect methods to evaluate the free energy. In this section we explain one of these methods, called thermodynamic integration [18] that relate the free energy of the system of interest to that of a reference system. Here we introduce a thermodynamic integration method to compute the free energy of hard-core systems, that was inspired by the earlier work of Heni and Löwen [45]. The free energy can be expressed as

$$F(N_c, N_p, V, T, A, \lambda = \lambda_{\rm max}) = F_{id}(N_c, N_p, V, T, \lambda = 0) + \int_{\lambda=0}^{\lambda_{\rm max}} d\lambda \left\langle \frac{\partial F}{\partial \lambda} \right\rangle_\lambda. \tag{2.28}$$

The reference system is chosen to be an ideal gas, so $F_{id}(N_c, N_p, V, T, \lambda = 0)$ is the Helmholtz free energy of N_c ideal colloids and N_p ideal polymers in a volume V at temperature T. We then introduce the suitable auxiliary Hamiltonian for the AOV model

$$H_\lambda = \lambda \left(\sum_{i<j}^{N_c} V_{cc}(R_{ij}) + \sum_{i=1}^{N_c} \sum_{j=1}^{N_p} V_{cp}(|\vec{R}_i - \vec{r}_j|) + \epsilon \sum_{i=1}^{N_c} V_{wc}(z_{c,i}) + \epsilon \sum_{i=1}^{N_p} V_{wp}(z_{p,i}) \right), \tag{2.29}$$

where we approximate the hard-core potentials with penetrable potentials. Note that the method can be applied to pure hard spheres by setting $V_{cp} = 0$, and $V_{wp} = 0$. The interaction potential is switched on adiabatically using the coupling parameter λ. In principle, our system of interest is described by the Hamiltonian (2.29) only in the limit $\lambda_{\rm max} \to \infty$,

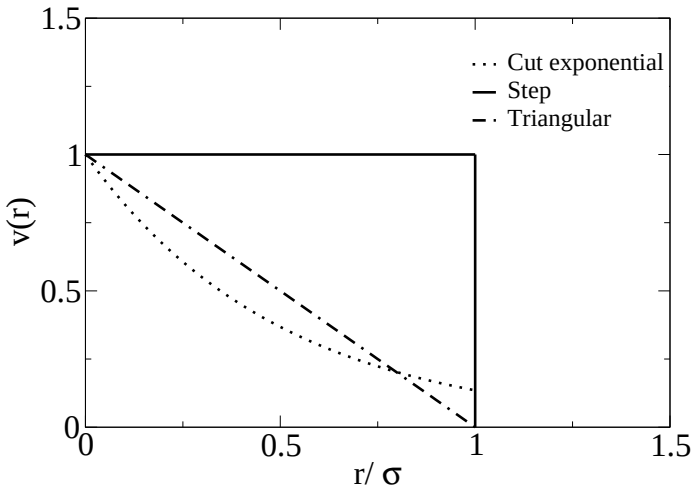

Figure 2.2: Comparison between soft-potential approximations of the hard-core potential.

but also for sufficiently high values of $\lambda_{\max}$ the system reduces to our system of interest with hard-core potentials. Clearly, $\lambda_{\max}$ should be sufficiently large to ensure that the system is indeed behaving as the hard-core system of interest. On the other hand, $\lambda_{\max}$ should not be too large, as this would make the numerical integration less accurate. The integrand function of Eq. (2.28)

$$\left\langle \frac{\partial F}{\partial \lambda} \right\rangle_\lambda = \left\langle \frac{\partial H_\lambda}{\partial \lambda} \right\rangle_\lambda = \left\langle \frac{H_\lambda}{\lambda} \right\rangle_\lambda , \tag{2.30}$$

can now be computed in a MC simulation. For $\lambda = 0$, this system reduces to an ideal gas, while for $\lambda \to \infty$, the system describes the AOV model given by Eqs. (1.15)-(1.17), and Eq. (2.1) in bulk ($\epsilon = 0$) or confined by two walls ($\epsilon = 1$).

There are different choices possible for the penetrable potentials, here we will present three different options, illustrated in Fig. 2.2.

2.5.1 Step function

The simplest approximation for the hard-core potential is the step function. In this approximation the colloid-colloid interaction reads

$$V_{cc}(R_{ij}) = \Theta(\sigma_c - R_{ij}), \tag{2.31}$$

where $R_{ij} = |\vec{R}_i - \vec{R}_j|$ is the distance between two colloidal particles, with $\vec{R}_i$ the position of the centre-of-mass of colloid i, and $\Theta(x)$ is the Heaviside step function. Likewise we

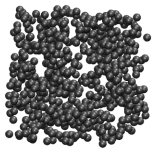

define the interaction potential between the colloids and the polymers as

$$V_{cp}(|\vec{R}_i - \vec{r}_j|) = \Theta\left(\frac{(\sigma_c + \sigma_p)}{2} - |\vec{R}_i - \vec{r}_j|\right), \tag{2.32}$$

with $\vec{r}_j$ the position of the centre-of-mass of polymer j. The interaction between the walls and the particles of species $k = c, p$ is

$$V_{wk}(z_{k,i}) = \Theta\left(\frac{\sigma_k}{2} - z_{k,i}\right) + \Theta\left(\frac{\sigma_k}{2} - (H_k - z_{k,i})\right), \tag{2.33}$$

where $z_{k,i}$ is the z-coordinate of particle i of species k.

2.5.2 Triangular function

For this model the colloid-colloid interaction reads

$$V_{cc}(R_{ij}) = \begin{cases} 1.0 - \frac{R_{ij}}{\sigma_c} & \text{if } R_{ij} < \sigma_c \\ 0 & \text{otherwise} \end{cases}, \tag{2.34}$$

where $R_{ij} = |\vec{R}_i - \vec{R}_j|$ is the distance between two colloidal particles, with $\vec{R}_i$ the position of the centre-of-mass of colloid i. The colloid-polymer interaction reads

$$V_{cp}(|\vec{R}_i - \vec{r}_j|) = \begin{cases} 1.0 - \frac{|\vec{R}_i - \vec{r}_j|}{(\sigma_c + \sigma_p)/2} & \text{if } |\vec{R}_i - \vec{r}_j| < (\sigma_c + \sigma_p)/2 \\ 0 & \text{otherwise} \end{cases}, \tag{2.35}$$

with $\vec{r}_j$ the position of the centre-of-mass of polymer j. The interaction between the walls and the particles of species $k = c, p$ is

$$V_{wk}(z_{k,i}) = \begin{cases} 1.0 - \frac{z_{k,i}}{\sigma_k/2} & \text{if } z_{k,i} < \sigma_k/2 \\ 0 & \text{otherwise} \end{cases}, \tag{2.36}$$

where $z_{k,i}$ is the z-coordinate of particle i of species k.

2.5.3 Cut exponential function

The colloid-colloid interaction reads

$$v_{cc}(R_{ij}) = \begin{cases} \epsilon \exp(-\mathrm{A} R_{ij}) & \text{if } R_{ij} < \sigma_c \\ 0 & \text{otherwise} \end{cases}, \tag{2.37}$$

where $R_{ij} = |\vec{R}_i - \vec{R}_j|$ is the distance between two colloidal particles, with $\vec{R}_i$ the position of the centre-of-mass of colloid i, and A is an adjustable parameter (A is set equal to two in Fig. 2.2). Likewise we define the interaction potential between the colloids and the polymers as

$$V_{cp}(|\vec{R}_i - \vec{r}_j|) = \begin{cases} \epsilon \exp(-\mathrm{B}|\vec{R}_i - \vec{r}_j|) & \text{if } |\vec{R}_i - \vec{r}_j| < (\sigma_c + \sigma_p)/2 \\ 0 & \text{otherwise} \end{cases}, \tag{2.38}$$

with $\vec{r}_j$ the position of the centre-of-mass of polymer j, and B is an adjustable parameter. The interaction between the walls and the particles of species $k = c, p$ is

$$v_{wi}(z_{k,i}) = \begin{cases} \epsilon \exp(-Cz_{k,i}) & \text{if } z_{k,i} < \sigma_k/2 \\ 0 & \text{otherwise} \end{cases} , \tag{2.39}$$

where $z_{k,i}$ is the z-coordinate of particle i of species k, and C is an adjustable parameter.

2.6 Simulation details

The free energy is obtained from Eq. (2.28). The integrals are evaluated using a 21-point Gauss-Kronrod formula, where 5000-15000 MC cycles per particle are used for the sampling of each integration point. The wall-fluid interfacial tension is then computed using equation (2.14). The number of colloids N_c^{bulk}, the chemical potential of the polymers μ_p, and the volume $V = L \times L \times H$ are fixed. We perform semi-grand canonical ensemble simulations of the AOV model in bulk and a separate simulation of the AOV model confined by two walls, and measure the average number of polymer in the bulk, $\langle N_p^{\text{bulk}} \rangle$, and in the confined system, $\langle N_p \rangle$. In the second step, we perform two separate thermodynamic integrations (in the canonical ensemble) to obtain the free energy of the bulk system with N_c^{bulk} colloids and $\langle N_p^{\text{bulk}} \rangle$ polymers in a volume V, and the confined system of volume V with N_c^{bulk} colloids and $\langle N_p \rangle$ polymers. In the canonical ensemble simulations, the chemical potential of the polymers is determined as a consistency check. Typical numbers of the colloids and the polymers are $N_c^{\text{bulk}} = 54-900$ and $N_p^{\text{bulk}} = 0-20000$, while the volume of the simulation box is about $V = (1200-3000)\sigma_c^3$ and $H > 16\sigma_c$. The errors are estimated by calculating the standard deviation from 4 or 5 independent simulations.

To study the (excess) adsorption of colloid-polymer mixtures at a planar hard wall we simulated both the bulk mixture and the mixture in contact with the hard wall in two independent Monte Carlo simulations in the grand canonical ensemble and hence we considered only statepoints of low colloid packing fraction η_c. After discarding 50000 MC steps per particle for equilibration, we take the average of the number of particles for another 50000 MC steps per particle. The differences in particle numbers (per unit area) in the confined system and in the bulk system then give the adsorption of both species via Eqs. (2.5) and (2.6).

2.7 Wall-fluid interfacial tension of hard spheres

In this section we present the results on the interfacial tension of hard spheres from simulation, SPT and DFT. As shown in Fig. 2.3, the tension increases upon increasing packing fraction, as expected since the wall tension is related to the work that needs to be done for inserting the hard wall in the fluid. The agreement between simulations and density functional theory [47, 56] is remarkably good. The equation (2.18) with the SPT pressure overestimates the wall-fluid tension at high density. On the other hand, the prediction of the expression (2.18) with the Carnahan-Starling expression for the pressure [45] underestimates the simulation results at high density.

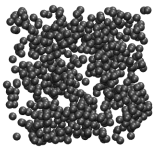

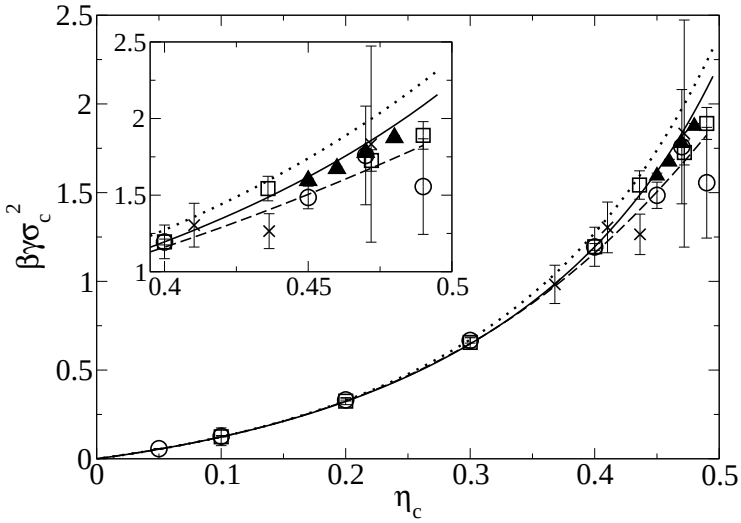

Figure 2.3: The reduced wall-fluid interfacial tension $\beta\gamma\sigma^2$ of hard spheres adsorbed at a hard wall as a function of the colloidal packing fraction η_c. We compare our simulation results for the step potential (open circles), and the exponential cut function (filled triangles), with Monte Carlo simulations of the triangular potential [45] (open squares) and Molecular Dynamics simulations [55] (crosses). The dotted line indicates the result from SPT interfacial tension plus SPT pressure, the dashed line indicate results of SPT interfacial tension plus the Carnahan-Starling pressure, and the solid line denotes the DFT result. Inset: Blow up of the high density region.

We now analyse the differences between the results obtained from using the step function, triangular function and cut-exponential function as penetrable potentials. As shown in Fig. 2.3, the step potential performs very well up to a packing fraction $\eta_c = 0.4$, but for higher densities the error bars are huge. This is due to equilibration problems: the step potential is unable to discriminate between different degrees of overlaps between two spheres, with the result of huge fluctuations in the integration results at high packing fraction. The equilibration problems for the step potential can be solved by using a potential whose value changes as a function of the distance between the colloids. The choice of Heni and Löwen [45] was the triangular potential. The triangular potential equilibrates better than the step potential, but as shown in Fig. 2.3, the performance at high density is not good. This is due to the slow convergence of the triangular function to the real hard-sphere potential. i.e. hard-sphere behaviour is reached only for very high values of the parameter $\lambda_{\max}$. To combine the good convergence of the step potential and the good equilibration of the triangular potential we use the cut exponential function. As shown in Fig. 2.3, the statistical error of the integration with this potential remains small also at very high density. In fact, the limit is set by the onset of prefreezing [57] for $\eta_c \simeq 0.485$, where the thermodynamic integration fails.

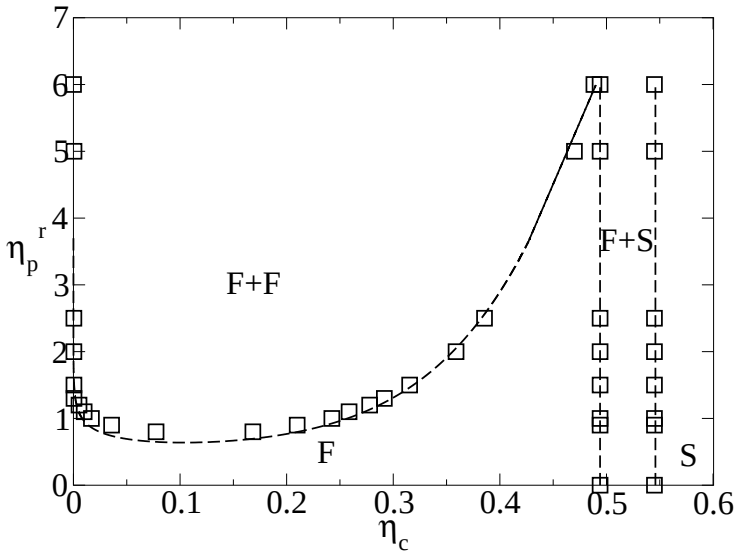

Figure 2.4: Phase diagram of the AOV model for size ratio $q = 1$ as obtained from simulations, taken from Refs. [14] (symbols), and free volume theory [30] (dashed line) as a function of the colloid packing fraction η_c and the polymer reservoir packing fraction η_p^r. F and S denote the stable fluid and solid (fcc) phase. F+F and F+S denote, respectively, the stable fluid-fluid, and fluid-solid coexistence region.

2.8 Wall-fluid interfacial tension of model colloid-polymer mixtures

We determined the wall-fluid interfacial tension for AOV colloid-polymer mixtures of size ratio $q = 0.6$ and $q = 1$ for different values of the polymer reservoir packing fraction η_p^r and of the colloid packing fraction η_c. Since we are interested in the low-density regions, we applied the thermodynamic integration with the step potential.

The addition of nonadsorbing polymers to a colloidal suspension of hard spheres can induce a phase separation. In Fig. 2.4 we show the bulk phase diagram for size ratio $q = 1$ from previous simulations [14] in the (η_p^r,η_c) representation. For comparison, we also plot the phase diagram obtained from free volume theory, which is equivalent to our DFT phase diagram [30]. At $\eta_p^r = 0$ we find the freezing transition of the pure hard-sphere system with packing fractions $\eta_c^f \simeq 0.494$ and $\eta_c^s \simeq 0.545$ for the coexisting fluid and solid phase, respectively. The critical point is estimated to be at $\eta_{p,crit}^r = 0.86$, while DFT, equivalent to the free-volume theory predicts $\eta_{p,crit}^r = 0.638$. For $\eta_p^r < \eta_{p,crit}^r$, we recover the hard-sphere freezing transition, i.e. there is a stable fluid phase for $\eta_c < 0.494$, a fluid-solid coexistence region for $0.494 < \eta_c < 0.545$, and a stable solid phase (fcc crystal) for $\eta_c > 0.545$. For $\eta_p^r > \eta_{p,crit}^r$, a fluid-fluid coexistence region appears where the system

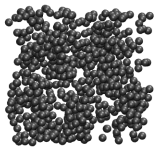

demixes in a colloidal liquid phase, rich in colloids and poor in polymers, and a colloidal gas phase, that is poor in colloids and rich in polymers. The triple point, where the gas, the liquid, and the solid are in coexistence, is located at $\eta^r_{p,\text{triple}} = 6$. For $\eta^r_p > \eta^r_{p,\text{triple}}$, the fluid-fluid coexistence region disappears, and a wide crystal-fluid coexistence region appears. The overall phase diagram is analogous to that of a simple fluids upon identifying η^r_p with the inverse temperature. Despite differences near the critical point, DFT and simulations results are in good agreement for state points at $\eta^r_p > 1.5$. In Fig. 2.5(a) and Fig. 2.5(c) we show the wall-fluid tension for state points below the gas-liquid critical point for size ratio $q = 0.6$ and $q = 1$, respectively. For comparison, we also plot the results for pure hard spheres ($\eta^r_p = 0$). The addition of non-adsorbing polymers to a suspension of hard-sphere colloids (i.e. increasing η^r_p) increases the wall-fluid interfacial tension. For $\eta_c = 0$, the wall-tension is the work done to introduce an impenetrable wall in an ideal gas of polymers divided by the total area: $\beta\gamma(\eta_c = 0) = \beta P^{id}\sigma_p/2$, where $\beta P^{id} = \rho^r_p$ is the bulk pressure of the ideal gas of polymer and $\sigma_p/2$ is the thickness of the depletion layer of the polymer at the wall. For small η_c, the slope of the tension is smaller than in the hard sphere case and for $\eta^r_p \geq 0.4$ it is negative. This is due to the attractive interaction that arises between the colloidal particles and the walls. For large η_c the interfacial tension approaches that of pure hard spheres as at high colloid density the number of polymers in the mixture rapidly approaches zero. Simulations and DFT are in good agreement for all state points that we considered. The SPT predicts correctly the value at $\eta_c = 0$, but it systematically overestimates the wall-fluid tensions for all values of $\eta_c > 0$. One can show that the low η_c expansion violates an exact wall sum rule [58]. The deviation increases with increasing η^r_p. In Fig. 2.5(b) we show the results for size ratio $q = 0.6$ for state points that are at higher η^r_p than the DFT gas-liquid critical point. We did not calculate the binodal with computer simulation, but the system was still in the one phase region of the phase diagram for $\eta^r_p = 0.5$ and 0.6. For comparison, we also plot the results from DFT and SPT. Note that DFT results are only shown in the stable gas and liquid regimes and are hence disconnected from each other, showing the biphasic region at intermediate η_c. In Fig. 2.5(d) we show the results for the size ratio $q = 1$ for state points that are at higher η^r_p than the DFT gas-liquid critical point. For small η_c the SPT fails to reproduce the slope of the curves, due to the absence of colloid correlations (layering) near the hard wall in SPT theory.

We now turn our attention to the adsorption of colloids and polymers at a hard wall, as defined by Eqs. (2.5), and (2.6). We compare the simulation results with those from DFT and SPT. In Figs. 2.6(a) and 2.6(c), we show the results on the colloidal adsorption while in Figs. 2.6(b), and 2.6(d), we show the results on polymer adsorption for size ratio q=0.6 and q=1, respectively. We notice that increasing the number of polymers in the system (i.e. increasing η^r_p) the adsorption of colloids increases; the colloids are attracted at the hard wall by the depletion interaction. As shown by the polymer adsorption the increase in number of colloidal particles at the walls is followed by a decrease of the number of adsorbed polymers while increasing the total number of polymers in the system. The agreement between simulations and DFT is good. This is not surprising since the DFT is known to provide an accurate description of the colloid-polymer mixture at a planar hard wall [59]. The SPT equations reproduce the η_c=0 limit correctly. For $\eta_c \neq 0$ the essential features are reproduced but with low accuracy. We also note that the differences in SPT

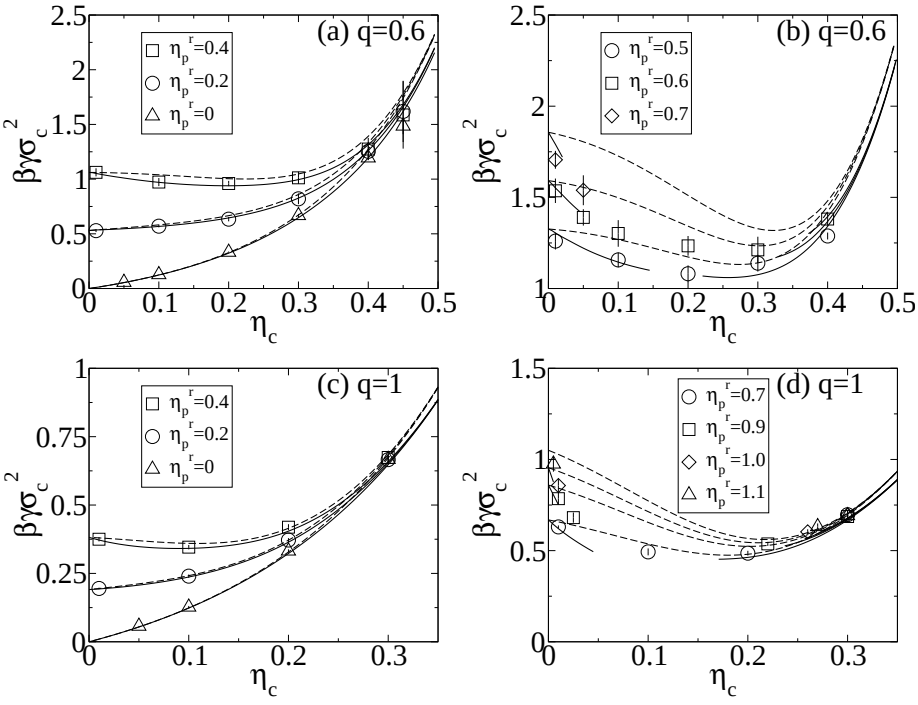

Figure 2.5: The wall-fluid interfacial tension of the model colloid-polymer mixture adsorbed against a hard wall. The symbols denote simulation results, dotted curves denote SPT results [47], the solid curves denote DFT results [47]. (a) Size ratio $q = 0.6$ and η_p^r =0, 0.2, and 0.4; (b) size ratio $q = 0.6$ and η_p^r =0.5, 0.6, and 0.7; (c) size ratio $q = 1$ and η_p^r =0, 0.2, and 0.4; (d) size ratio $q = 1$ and η_p^r =0.7, 0.9, and 1.0.

are larger for increasing polymer reservoir packing fraction and for size ratio q=0.6. The SPT performance is worse when the number of polymers in the mixture is relatively high compared to the number of colloids.

2.9 Conclusions

In conclusion we investigated the wall-fluid tension of the AOV model colloid-polymer mixtures of size ratio $q = 0.6$ and $q = 1$ using Monte Carlo computer simulations. We used a thermodynamic integration method to determine the free energy of the bulk system and the inhomogeneous system. The wall-fluid interfacial tension is the surface excess free energy per unit area, and is in good agreement with the DFT results. The SPT wall-fluid interfacial tension is in overall agreement with simulations, but the comparison is worse for increasing polymer reservoir packing fraction. We also investigated the colloid and polymer adsorption of the colloid-polymer mixture at a planar hard wall and we found good agreement with DFT results. We derived a SPT expression for the adsorption

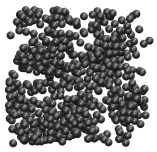

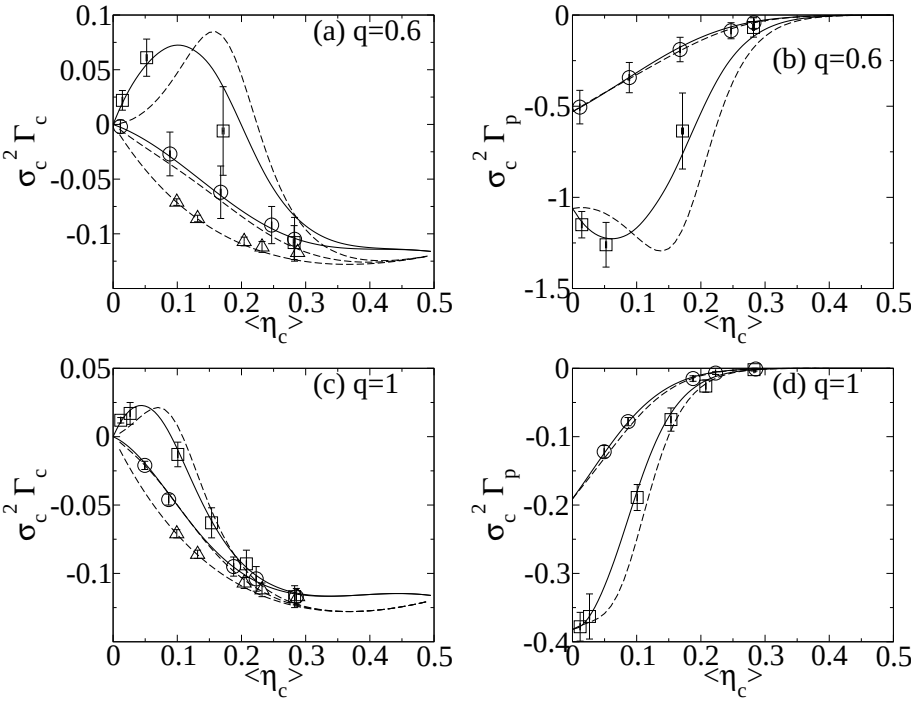

Figure 2.6: The adsorption $\Gamma\sigma_c^2$ of the colloid-polymer mixture at a hard wall as a function of the average colloid packing fraction $\langle\eta_c\rangle$. Simulation results for polymer reservoir packing fraction η_p^r = 0 (open triangles), η_p^r = 0.2 (open circles), and η_p^r = 0.4 (open squares) are compared with results from DFT (solid lines) and SPT (dashed lines). The DFT results for η_p^r = 0 are omitted for clarity. a) Colloid adsorption for size ratio q=0.6; b) Polymer adsorption for q=0.6; c) Colloid adsorption for q=1; d) Polymer adsorption for q=1.

of colloid-polymer mixtures at a hard wall. The expression reproduces the essential features of the adsorption, but with low accuracy. Our thermodynamic integration technique is well suited to determine the free energy of confined crystals and will be used in the next chapter to predict the full phase behaviour of confined hard spheres.

Acknowledgements: The DFT calculations presented in this chapter were carried out by Paul P. F. Wessels and Matthias Schmidt.

3

Hard spheres confined between two hard walls

In this chapter we study the phase behaviour of hard spheres confined between two parallel hard plates. We determine the full equilibrium phase diagram for arbitrary densities and plate separations from one to five hard-sphere diameters using free energy calculations. We find a first-order fluid-solid transition, which corresponds to either capillary freezing or melting depending on the plate separation. The coexisting solid phase consists of crystalline layers with either triangular (△) or square (□) symmetry. Increasing the plate separation, we find a sequence of crystal structures from $\cdots n\triangle \rightarrow (n+1)\square \rightarrow (n+1)\triangle \cdots$, where n is the number of crystal layers, in agreement with experiments on colloids. At high densities, the transitions between square to triangular phases are intervened by intermediate structures, e.g., prism, buckled, and rhombic phases.

3.1 Introduction

The physics of confined systems is important in different fields of modern technology, like lubrication, adhesion and nanotechnology. The study of simple models is instrumental in understanding the behaviour of complex systems. As such the hard-sphere system plays an important role in statistical physics; it serves as a reference system for determining the structure and phase behaviour of complex fluids, both in theory and simulations. The bulk phase behaviour of hard spheres is now well understood. At sufficiently high densities, the spheres can maximise their entropy by forming an ordered crystal phase [4, 60]. The insertion of a hard wall in such a fluid decreases the number of hard-sphere configurations. The system can increase its entropy by the spontaneous formation of crystalline layers with triangular symmetry, the (111) plane, at the wall, while the bulk is still a fluid [57]. It is induced by the presence of a single wall and should not be confused with capillary freezing. Capillary freezing denotes the phenomenon of confinement-induced freezing of the whole fluid in the pore at thermodynamic state points where the bulk is still a fluid. This transition depends strongly on the plate separation. The opposite phenomenon, called capillary melting, can also occur. The capillary induces melting for thermodynamic state points that correspond to a crystal in the bulk. Confinement can also change dramatically

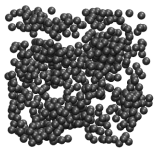

the equilibrium crystal structure. In 1983 Pieranski [61] reported a sequence of layered solid structures with triangular and square symmetry for colloidal hard spheres confined in a wedge. The buckling phase was later observed by Weiss et al. [62], but the sequence of high density structures is determined more accurately in recent experiments [63, 64], with the observation of prism phases with both square and triangular symmetry. Recently Cohen [65] studied configurations of confined hard spheres under shear, demonstrating the importance of the equilibrium configurations in the rheological properties. Despite the great number of theoretical and simulation studies on confined hard spheres [66–68], the full *equilibrium* phase behaviour is yet unknown. In fact, many of the previous studies were based on an order parameter analysis, which fails dramatically in discriminating the different structures at high densities and large plate separations. More importantly, free energy calculations of confined hard spheres are prohibited so far due to the lack of an efficient thermodynamic integration path which relates the free energy of interest to that of a reference system, while a further complication arises from the enormous number of possible solid phases that has to be considered. Hence, it is unresolved whether the experimentally observed phases are stabilised kinetically or are thermodynamically stable.

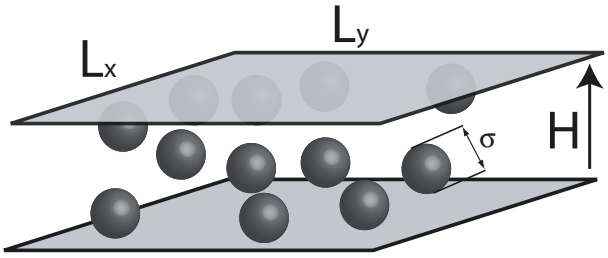

Figure 3.1: Illustration of hard spheres with diameter σ, confined between parallel hard plates of area $A = L_x L_y$ and a separation distance H.

In this chapter, we use an efficient thermodynamic integration path that enable us to calculate the free energy of *densely packed and confined* hard spheres, with high accuracy close to the fluid-solid transition. This method allow us to determine the stability of the structures found in experiments. To this end we perform explicit free energy calculations to map out the full phase diagram for plate separations from 1 to 5 hard-sphere diameters. We report a high number of *thermodynamically stable* crystal structures including triangular, square, buckling, rhombic, and prism phases, and a cascade of corresponding solid-solid transformations. In addition, the free energy calculations allow us to determine the chemical potential at coexistence, that was inaccessible in previous simulations. From

the analysis of the chemical potential, we find an intriguing sequence of capillary freezing and melting transitions coupled to a structural phase transition of the confined crystal. We note that our new method and results are also relevant for confined simple fluids [69–71] and self-assembled biological systems [72]. In addition, the structure of dense packings of spheres explains the shape of for instance snowflakes, bee honeycombs, and foams, and it is of great importance for fundamental research, e.g., solid state physics and crystallography, and for applications like communication science or powder technology [73, 74].

3.2 Model and Method

Our model system consists of N hard spheres with diameter σ, confined between two parallel hard plates of area $A = L_x L_y$ (Fig. 3.1). In each layer we used approximately 200 particles. We use the packing fraction $\eta = \pi\sigma^3 N/(6AH)$ as a dimensionless density, where H is the distance between two plates.

We first determined the trial structures carrying out Monte Carlo (MC) simulations in a box, which was allowed to change its shape to accommodate different types of crystals. The ratio L_x/L_y could vary while H and A were fixed. Trial solid structures were obtained from crystals with triangular or square symmetry relaxed with MC moves while slowly increasing the density by expanding the spheres. The free energy F for the resulting equilibrated structures was calculated as a function of η and H. We used the standard thermodynamic integration technique [18], but with a new and efficient path based on the cut-exponential function introduced in section 2.5 (see also Fig. 2.2). Neither the step function nor the triangular function have the necessary accuracy to compute the free energy at the coexisting densities. The sphere-sphere potential reads

$$v_{ij}(R_{ij}) = \begin{cases} \epsilon \exp(-\mathrm{A}R_{ij}) & \text{if } R_{ij} < \sigma_c \\ 0 & \text{otherwise} \end{cases}, \tag{3.1}$$

and the wall-fluid potential

$$v_{wi}(z) = \begin{cases} \epsilon \exp(-\mathrm{B}z_i) & \text{if } z_i < \sigma_c/2 \\ 0 & \text{otherwise} \end{cases}, \tag{3.2}$$

where R_{ij} is the distance between spheres i and j, z_i is the distance of sphere i to the nearest wall, A and B are adjustable parameters that are kept fixed during the simulations, and ϵ is the integration parameter. This penetrable potential enabled us to change gradually from a non-interacting system to the confined hard-core system of interest. The limit $\epsilon \to \infty$ yields the hard-core interaction defined by equation (1.5), but convergence of the thermodynamic integration was already obtained for $\epsilon \sim 70 k_B T$. The reference states ($\epsilon = 0 k_B T$) are the ideal gas and the Einstein crystal for the fluid and solid phase, respectively. We used a 21-point Gaussian quadrature for the numerical integrations and the ensemble averages are calculated from runs with 40000 MC cycles (attempts to displace each particle once), after first equilibrating the system during 20000 MC cycles. We determined phase coexistence by equating the grand potentials $\Omega = F - \mu N$ [50].

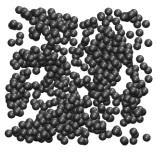

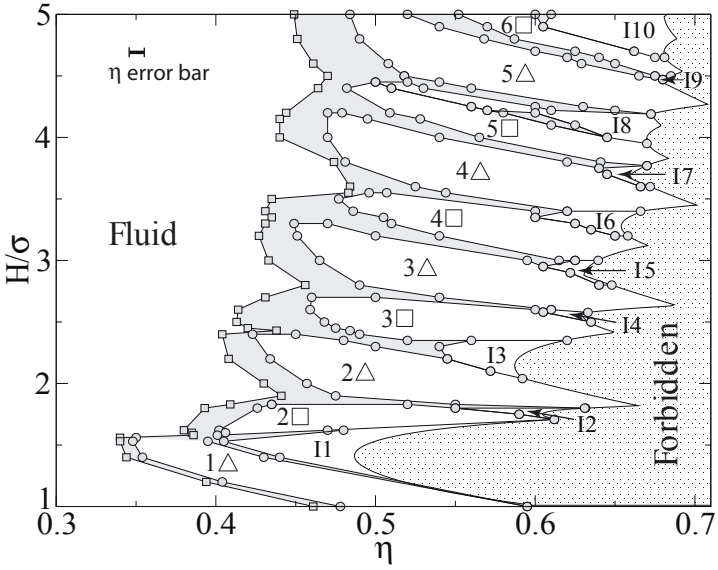

Figure 3.2: The equilibrium phase diagram of hard spheres with diameter σ confined between two parallel hard walls in the plate separation H - packing fraction η representation. The white, shaded and dotted regions indicate the stable one-phase region, the two-phase coexistence region, and the forbidden region, respectively.

3.3 Results

To validate the approach described in the previous section, we perform simulations of a bulk system of hard spheres and we find that the packing fractions of the coexisting fluid and face-centered-cubic (fcc) solid phase are given by $\eta_f = 0.4915 \pm 0.0005$ and $\eta_s = 0.5428 \pm 0.0005$, respectively. The pressure and the chemical potential at coexistence are $\beta P\sigma^3 = 11.57 \pm 0.10$ and $\beta\mu = 16.08 \pm 0.10$. These results are in good agreement with earlier results [60, 75]. Furthermore, to validate the approach for confined systems, we determine at bulk coexistence the wall-fluid interfacial tension $\beta\gamma_{\rm wf}\sigma^2 = 1.990 \pm 0.007$, and the wall-solid interfacial tension for the (111) and (100) planes of the fcc phase, $\beta\gamma_{\rm ws}^{111}\sigma^2 = 1.457 \pm 0.018$ and $\beta\gamma_{\rm ws}^{100}\sigma^2 = 2.106 \pm 0.021$. As already shown in Fig. 2.3 these results are in agreement with previous simulations [45], but the statistical error is one order of magnitude smaller due to our new thermodynamic integration path.

Employing this approach we determine the phase behaviour of confined hard spheres for plate separations $1 < H/\sigma \leq 5$. Fig. 3.2 displays the full phase diagram based on free energy calculations in the $H-\eta$ representation. The white regions of the phase diagram denote the stable one-phase regions. The shaded regions indicate coexistence between fluid and solid or two solid phases, and the dotted region is forbidden as it exceeds the maximum packing fraction of confined hard spheres. At low densities, we observe a stable fluid phase followed by a fluid-solid transition upon increasing the density. The os-

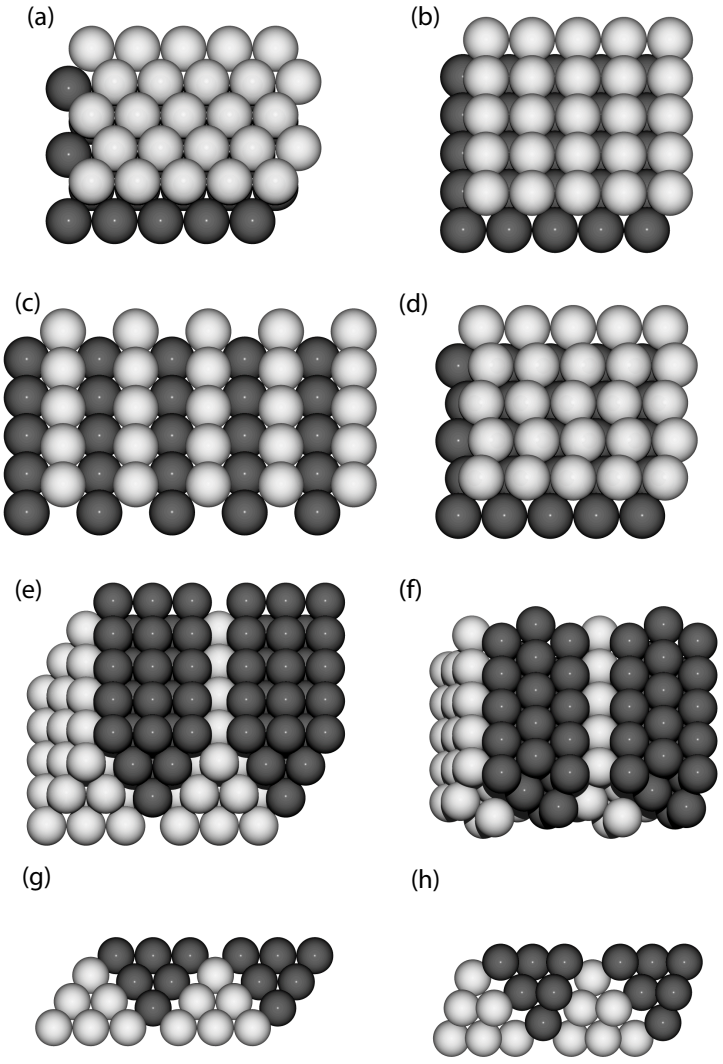

Figure 3.3: Stable solid structures of confined hard spheres. (a) The triangular phase $2\triangle$ (b) The square phase $2\square$ (c) The buckling phase $2\mathscr{B}$ (d) The rhombic phase $2\mathscr{R}$ (e),(g) The prism phase with square symmetry $3\mathscr{P}_{\square}$ (f),(h) The prism phase with triangular symmetry $3\mathscr{P}_{\triangle}$. In (a)-(f) the point of view is at an angle of 30° to the z direction. In (g),(h) the point of view is at an angle of 90°. Different shades indicate particles in different planes ((a)-(d)) or particles belonging to different prism structures ((e)-(h)).

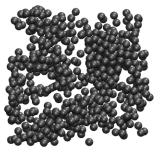

Table 3.1: List of intermediate structures In as found in our simulations and in the experiments of Fontecha [64].

Phase	Transition	Simulation[1]	Experiment
I1	$1\triangle \to 2\square$	$2\mathscr{B}$	$2\mathscr{B}$
I2	$2\square \to 2\triangle$	$2\mathscr{R}$	$2\mathscr{R}$
I3	$2\triangle \to 3\square$	$2\mathscr{P}_\triangle + 2\mathscr{P}_\square$	$2\mathscr{P}_\triangle + 2\mathscr{P}_\square$
I4	$3\square \to 3\triangle$	$3\mathscr{R} + 3\mathscr{P}_\square$	$3\mathscr{R} + 3\mathscr{P}_\square + 3\mathscr{P}_\triangle$
I5	$3\triangle \to 4\square$	$3\mathscr{P}_\triangle + 4\mathscr{B}$	$3\mathscr{P}_\square$
I6	$4\square \to 4\triangle$	$4\mathscr{P}_\square + 4\mathscr{R} + 4\mathscr{P}_\triangle$	$4\mathscr{P}_\square + 4\mathscr{P}_\triangle$
I7	$4\triangle \to 5\square$	$4\mathscr{P}_\triangle$	$4\mathscr{P}_\triangle$, $4\mathscr{P}_\square$, H^2
I8	$5\square \to 5\triangle$	$5\mathscr{P}_\square$+$4\mathscr{P}_\triangle$+$5\mathscr{R}$	$5\mathscr{P}^3$
I9	$5\triangle \to 6\square$	$5\mathscr{P}_\triangle$	no data
I10	$6\square \to 6\triangle$	$5\mathscr{P}_\square + 5\mathscr{P}_\triangle$	no data

cillations in the freezing and melting lines reflect the (in)commensurability of the crystal structures with the available space between the walls. For the crystal phases, we follow the convention introduced by Pieranski [61], where $n\triangle$ denotes a stack of n triangular layers, and $n\square$ a stack of n square layers. For $H/\sigma \to 1$, the stable crystal phase consists of a single triangular layer $1\triangle$, which packs more efficiently than the square layer. As the gap between the plates increases, crystal slabs with triangular (Fig. 3.3(a)) and square packings (Fig. 3.3(b)) are alternately stable. We find the characteristic sequence $\cdots n\triangle \to (n+1)\square \to (n+1)\triangle$, which consists of an $n\triangle \to (n+1)\square$ transformation where both the number of layers and the symmetry change followed by an $(n+1)\square \to (n+1)\triangle$ transformation where only the symmetry changes. This sequence is driven by a competition of a smaller height of n square layers compared to n triangular layers and a more efficient packing of triangular layers w.r.t. square layers. When the available gap is larger than required for the $n\triangle$ structure, but smaller than for $(n+1)\square$, intermediate structures may become stable. Similar arguments can be used for the intervention of intermediate structures in the $(n+1)\square \to (n+1)\triangle$ transformation. Especially at high packing fractions, the spheres can increase their packing by adopting interpolating structures. In Fig. 3.2 we report the boundaries of the interpolating regions In. Each region represents one or more interpolating structures, that are listed in Tab. 3.1, according to the standard notation. Within the resolution of our simulations, it is difficult to draw the phase boundaries of all the intermediate structures in In, but in Tab. 3.1 the *thermodynamically stable* structures are listed in the order they appear upon increasing H and η. We also compare our sequence of structures with the experimental one [64]. The experiments considered charged particles, but we do not expect that the soft repulsion has a strong effect on the observed structures at high densities. The agreement is excellent at small plate separations. The buckling phase $2\mathscr{B}$ (Fig. 3.3(c)) interpolates between the $1\triangle$ and $2\square$ phases. In the $2\mathscr{B}$ phase, the $1\triangle$ structure is split into two sublayers consisting of rows that are displaced in height and which can transform smoothly into $2\square$ structure upon increasing the gap. The rhombic phase $2\mathscr{R}$ (Fig. 3.3(d)) is found between the $2\square$ and $2\triangle$ phases. The rhombic phase is also stable between the $n\square$ and $n\triangle$ phases for $n \leq 5$, but not in the whole region. In addition, we find that at higher n the interpolating structures are mainly

prism phases. In agreement with experiments, we find two types of prisms, one with a square base $n\mathscr{P}_{\square}$ (Fig. 3.3(e)), and one with a triangular base $n\mathscr{P}_{\triangle}$ (Fig. 3.3(f)), where n indicates the number of particles in the lateral dimension of the prism base. As shown in Fig. 3.3(g),(h), these structures display large gaps as a result of periodically repeated stacking faults in the packing which, nevertheless, allow particles to pack more efficiently, than a phase consisting of parallel planes of particles. For $n > 3$, differences between simulations and experiments emerge. We find that the stability region of interpolating structures between $n\triangle$, and $(n+1)\square$ decreases for larger H, becoming invisible on the scale of Fig. 3.2 for $I9 = 5\triangle \rightarrow 6\square$. On the other hand, the region of stability of the interpolating structures between $n\square$ and $n\triangle$ increases while increasing the wall separation, becoming stable also at low packing fractions for the transitions $I8 = 5\square \rightarrow 5\triangle$, and possibly $I10 = 6\square \rightarrow 6\triangle$. We also note that the solid-solid transitions are first-order with a clear density jump at low η, but they get weaker (and maybe even continuous) upon approaching the maximum packing limit. In addition, the rhombic and buckling phases are highly degenerate as we find zig-zag and linear buckling or rhombic phases, and a combination of those.

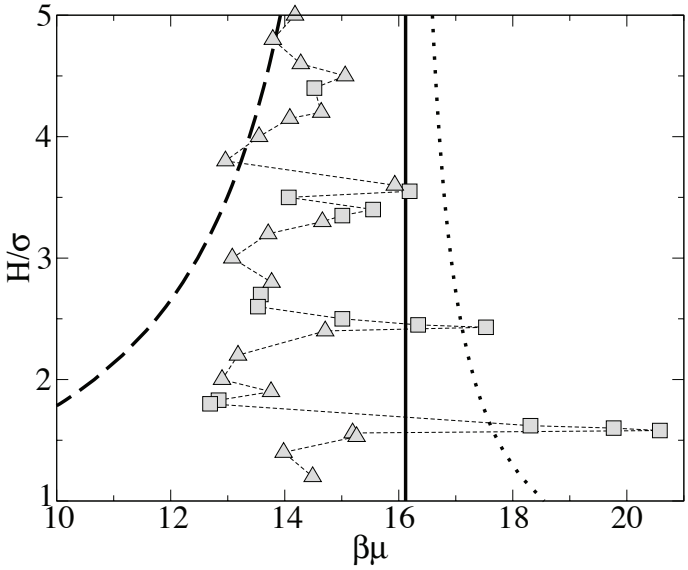

Figure 3.4: Chemical potential $\beta\mu$ at fluid-solid coexistence, for different wall separations H/σ. The symbols are the simulation results for the triangular ($\triangle$) and square structures ($\square$). The thin dashed line is a guide to the eye. The thick continuous line indicate the value of the bulk freezing chemical potential $\beta\mu = 16.08$. The thick dashed and dotted curves are the prediction of the Kelvin equation for the (111), and (100) planes parallel to the walls, respectively.

We now turn our attention to the fluid-solid transition. In Fig. 3.4, we plot the chemical potential $\beta\mu^{\text{cap}}$ at the freezing transition of the confined system as a function of H. The freezing for crystal slabs with a triangular symmetry are denoted by triangles, while the square symmetry is displayed by squares. We find strong oscillations in the chemical

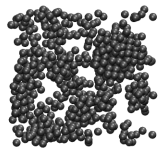

potential reminiscent to the (in)commensurability of the crystal structures with plate separation. The highest values for $\beta\mu^{\text{cap}}$ are reached at the transition region $n\triangle \rightarrow (n+1)\square$, corresponding to plate separations where both structures are incommensurate and hence unfavourable. In this regime, $\beta\mu^{\text{cap}}$ can reach values that are higher than the bulk freezing chemical potential $\beta\mu^{\text{bulk}}$ (the black vertical line in Fig. 3.4), corresponding to capillary melting, while the freezing transitions with $\beta\mu^{\text{cap}}$ lower than the bulk value correspond to capillary freezing. Hence, we find a re-entrant capillary freezing/melting behaviour for wall separations $1 < H/\sigma < 3.5$. In addition, we compare our results with the predictions of the Kelvin equation[52]: $\beta\mu^{\text{cap}} = \beta\mu^{\text{bulk}} - \pi\sigma^3/3H(\gamma_{wf} - \gamma_{ws})/(\eta_s - \eta_f)$ using the parameters determined in our simulations. The thick dashed line in Fig. 3.4 is the prediction of the Kelvin equation for the (111) crystal plane (triangular order) at the walls, while the dotted line is that for the (100) plane (square order). The Kelvin equation predicts capillary freezing for the triangular structure and capillary melting for the square structures. The Kelvin equation predictions are in reasonable agreement with our simulations for triangular order for wall separation as small as $H/\sigma \sim 4$, but deviates for smaller H, while the prediction for the square structure is in agreement only at very small H. It is surprising to find qualitative agreement at small H since the Kelvin equation is valid in the limit $H/\sigma \rightarrow \infty$.

3.4 Conclusion

In summary, we have calculated the equilibrium phase diagram of confined hard spheres using free energy calculations with a novel integration path. The high density sequence of structures is in good agreement with experimental results. We find that the prism phases are thermodynamically stable also at lower densities, and this work will, hopefully, stimulate further experimental investigations, for a quantitative comparison at intermediate packing fractions. In addition, our results show an intriguing sequence of melting and freezing transitions upon increasing the distance between the walls of a slit which is in contact with a bulk reservoir. The mechanical behaviour is therefore very sensitive on the degree of confinement, and the knowledge of the phase diagram can help the understanding and fabrication of new materials. The transition from confined to bulk behaviour, and the interface between different solid structures (studied in lower dimensions in Ref. [76]) represent interesting directions for future investigations.

4

Colloid-polymer mixtures confined between two parallel planar walls

We investigate the fluid-fluid demixing transition in inhomogeneous AOV colloid-polymer mixtures confined between two parallel plates with separation distances between one and ten colloid diameters. Two different types of confinement induced by a pair of parallel walls are considered, namely either through two hard walls or through two semi-permeable walls that repel colloids but allow polymers to freely penetrate. For hard (semi-permeable) walls we find that the capillary binodal is shifted towards higher (lower) polymer fugacities and lower (higher) colloid fugacities as compared to the bulk binodal; this implies capillary condensation (evaporation) of the colloidal liquid phase in the slit. A macroscopic treatment is provided by a novel symmetric Kelvin equation for general binary mixtures, based on the proximity in chemical potentials of statepoints at capillary coexistence and the reference bulk coexistence. Results for capillary binodals compare well with those obtained from the classic version of the Kelvin equation due to Evans and Marini Bettolo Marconi [J. Chem. Phys. **86**, 7138 (1987)], and are quantitatively accurate away from the fluid-fluid critical point, even at small wall separations. However, the significant shift of the critical polymer fugacity towards higher values upon increasing confinement, as found in simulations, is not reproduced. For hard walls the density profiles of polymers and colloids inside the slit display oscillations due to packing effects for all statepoints. For semi-permeable walls either similar structuring or flat profiles are found, depending on the statepoint considered.

4.1 Introduction

Capillary effects that are induced by the confinement of a system are crucial to a variety of phenomena. An everyday example is the capillary rise, against gravity, of the meniscus of a free gas-liquid interface at the wall of a container that encompasses the fluid. The contact angle at which the gas-liquid interface hits the wall is described by Young's equation [52], $\gamma_{\mathrm{lg}}\cos\theta = \gamma_{\mathrm{wg}} - \gamma_{\mathrm{wl}}$, where the relevant interfacial tensions are those between the coexist-

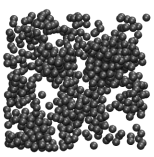

ing liquid and gas phase, γ_{lg}, the wall and the gas phase, γ_{wg}, and the wall and the liquid phase, γ_{wl}. When the contact angle is finite, $0 < \theta < \pi$, the liquid phase partially wets the wall; for $\theta = 0$ a macroscopic layer of liquid grows between the wall and the gas phase far away from the wall, hence the liquid completely wets the wall; for $\theta = \pi$ a correspondingly reversed situation occurs: a macroscopic layer of gas grows between the wall and the liquid phase far away from the wall, hence the wall is completely "wet" by the gas phase and drying occurs. All these phenomena are driven by the influence of a *single* wall on the fluid.

Different, but related effects occur under confinement of fluids in pores, e.g. between *two* parallel planar walls. The phase diagram of such a confined system can differ significantly from that in bulk [77, 78]. Depending on the nature of the interactions between fluid particles and the walls, the bulk gas with chemical potential $\mu < \mu_{sat}$, where μ_{sat} is the value at saturation, can condense inside the pore and form a dense confined liquid phase. This capillary phase transition is accompanied by a jump in the adsorption isotherm at a given value of $\mu < \mu_{sat}$. Confinement may lead to stabilization of a phase that is unstable (or at least metastable) in bulk for a given statepoint. As opposed to capillary condensation the opposite effect, referred to as capillary evaporation, is also feasible: A fluid with chemical potential $\mu > \mu_{sat}$ forms a liquid in bulk, but evaporates inside the capillary. A simple, yet powerful, way to quantitatively describe capillary phase transitions is based on the Kelvin equation, derived from a macroscopic treatment of the thermodynamics of the inhomogeneous system. For capillaries with planar slit-like geometries [50], it predicts that liquid-gas coexistence inside the slit will occur at $\mu = \mu_{sat} + \gamma_{lg}\cos(\theta)/h$, where h is the separation distance between the two walls. Hence, contact angles $0 \leq \theta < \pi/2$ correspond to capillary condensation, while $\pi/2 < \theta \leq \pi$ corresponds to capillary evaporation. In this chapter we investigate capillary phenomena occurring on a mesoscopic scale using a simple model for a mixture of sterically-stabilized colloidal particles and non-adsorbing polymer coils confined between two parallel planar walls. As explained in section 1.3.3, polymers induce an attractive interaction between two colloids, and between colloids and a hard wall. This attractive interaction is responsible for the complete wetting of the colloidal liquid phase at a hard wall [14, 59, 79–81]. Complete wetting of the colloidal liquid is actually observed in experimental realizations of colloid-polymer mixtures in contact with glass substrates [82, 83] or glass substrates that possess the same coating with an organophilic group as the colloidal particles do [13]. On the other hand, experiments [84] with polymer-grafted substrates (of the same chemical nature as the dissolved polymers) showed that the contact angle is larger than $\pi/2$. Although the structure of the polymer coating was not studied in detail, Wijting et al. [84] expect the polymers to form a fluffy layer with a distribution of loops and tails. Such a layer is known to diminish the depletion interaction between colloidal particles and the substrate [85]. Wessels et al. [47] modelled this type of substrate using a semi-permeable wall, that is completely penetrable to the polymers but act like a hard wall on the colloids. Using DFT they predict complete drying. More recently the behavior of the mixtures in contact with porous walls was investigated, and both wetting of the surface and drying into the porous matrix depending on the precise path in the phase diagram were found [86]. Porous walls are wet by the liquid phase, with a transition from partial to complete wetting at a polymer fugacity z_p almost independent on the porosity of the wall.

Although much research has been devoted to the understanding of the behavior of the

mixture in contact with a single wall, few studies have been reported on the effect of confinement on the phase behavior of the mixture. Computer simulations and theory were used to study porous matrices. When impenetrable to both components they were found to induce capillary condensation, whereas matrices penetrable to the polymers, but not to the colloids, induce capillary evaporation [87, 88]. Furthermore laser induced confinement [89] was found to induce capillary condensation. The only experimental result on capillary condensation that we are aware of is that by Aarts and Lekkerker [83]. These authors found capillary condensation for colloid-polymer mixtures confined in a wedge formed by a glass bead placed on a glass substrate.

The aim of the present chapter is to determine the phase behavior and the structure of colloid-polymer mixtures confined between two parallel planar walls for a complete range of wall separation distances. We focus on the fluid part of the phase diagram, and present results for hard walls and semi-permeable walls, obtained from computer simulations and density functional theory. We also investigate the structure of the mixtures inside the pore, and derive and test a generalized Kelvin equation for binary mixtures confined in slit-like pores and compare its predictions with our simulation results.

4.2 Model

The mixture of colloids and polymers is described by the AOV model we introduced in section 1.3.3.

The hard walls are modelled such that neither polymers nor colloids can penetrate the walls. The wall-particle potential acting on species $k = \mathrm{c}, \mathrm{p}$ is

$$v_{\mathrm{wk}}(z) = \begin{cases} 0 & \text{if } -(H-\sigma_k)/2 < z < (H-\sigma_k)/2 \\ \infty & \text{otherwise,} \end{cases} \tag{4.1}$$

where z is the coordinate normal to the walls, and H is the wall separation distance. We define the volume of the system as $V = AH$, where A is the (lateral) area of the confining walls. Fig. 4.1(a) shows an illustration of the model.

Semi-permeable walls are defined by the external potential

$$v_{\mathrm{wk}}(z) = \begin{cases} 0 & \text{if } -(H_k-\sigma_k)/2 < z < (H_k-\sigma_k)/2 \\ \infty & \text{otherwise,} \end{cases} \tag{4.2}$$

where H_c is the wall separation distance that the colloids experience, while H_p is the wall separation distance that the polymers feel; the latter can be interpreted as the distance between substrate walls. We define the volume as $V = AH_\mathrm{c}$. Fig. 4.1(b) shows an illustration of this model. Any choice of $H_\mathrm{p} > H_\mathrm{c} + 2\sigma_\mathrm{p}$ leads to decoupling of the (inner) colloid and (outer) polymer wall, since the ideal gas of polymers cannot mediate correlations from the substrate to the interior of the system.

4.3 Simulation method

We perform Gibbs Ensemble Monte Carlo (GEMC) simulations to determine the phase behavior of the AOV model in bulk and confined between two parallel planar walls. The num-

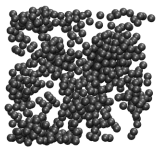

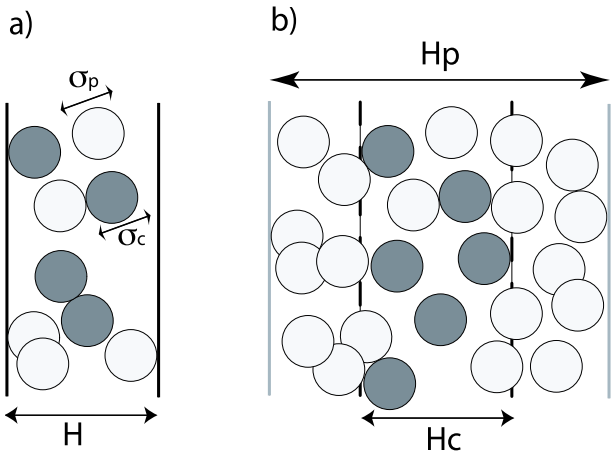

Figure 4.1: (a) Illustration of the AOV model of hard-sphere colloids (dark-grey circles) of diameter σ_c and ideal polymers (light-grey circles) of diameter σ_p confined between parallel hard walls of area A and separation distance H. Colloids behave as hard spheres, polymers cannot penetrate colloids, and polymers may freely overlap. The walls are impenetrable to both components. The z-axis is perpendicular to both walls, and the origin is located in the middle of the slit. (b) Same as in (a) but for walls that are penetrable for polymers and impenetrable for colloids (semi-permeable walls) of area A and separation distance H_c. Polymers are confined between parallel hard walls (continuous line) with separation distance H_p. This is a model for substrates at distance H_p coated with a polymer brush (not shown) of thickness $(H_p - H_c)/2$; the free distance between both polymer brushes is H_c. Solute polymers (light-grey circles) are able to penetrate the brush (dashed lines) but not the substrate; the brush acts like a hard wall to the colloids.

ber of colloids N_c, the number of polymers N_p, and the volume V are kept fixed and are divided into two separate subsystems a and b with volume V^a and V^b, respectively, with the constraints that $V = V^a + V^b$, $N_c = N_c^a + N_c^b$ and $N_p = N_p^a + N_p^b$. The two subsystems are allowed to exchange both particles and volume in order to satisfy the conditions for phase equilibrium, i.e., equality in both phases of the chemical potentials of the two species and of the pressure. The method can be applied to bulk as well as to confined systems [90, 91], and will be described briefly below; for more details, we refer the reader to Ref. [18].

The bulk equilibrium conditions between two coexisting phases require equal temperature T, equal chemical potential μ_i for each species i ($i = c, p$ in our case) and equal pressure P. In our model, the temperature T is irrelevant; because of the hard-core nature of the interaction potentials it acts only as a scaling factor setting the thermal energy scale. In the GEMC method, the two coexisting phases are simulated simultaneously in two separate (cubic) boxes with standard periodic boundary conditions. The acceptance probability for a trial move to displace a randomly selected particle is

$$\mathscr{P} = \min\{1, \exp[-\beta(U_{new} - U_{old})]\}, \tag{4.3}$$

where

$$\exp[-\beta(U_{\rm new}-U_{\rm old})] = \begin{cases} 1 & \text{if } \beta U_{\rm new} = 0 \\ 0 & \text{if } \beta U_{\rm new} = \infty \end{cases} \tag{4.4}$$

with $U_{\rm new}$ and $U_{\rm old}$ the energy of the new and old generated configuration, and $\beta = 1/(k_B T)$ the inverse temperature with k_B being the Boltzmann constant. Note that $U_{\rm old} = 0$ as configurations with $U_{\rm old} = \infty$ are excluded by a vanishing Boltzmann factor (regardless of the temperature). Transfer of (single) particles between the two boxes is used to satisfy equal chemical potential for both species. We select at random which subsystem is the donor and which is the recipient as well as the species (colloid or polymer) of the particle transfer. Subsequently, a specific particle is randomly selected in the donor box and transferred to a random position in the recipient box with probability

$$\mathscr{P} = \min\left\{1, \frac{\mathrm{N_i^a V^b}}{(\mathrm{N_i^b}+1)\mathrm{V^a}} \exp[-\beta(\mathrm{U_{new}}-\mathrm{U_{old}})]\right\}, \tag{4.5}$$

where $i = \mathrm{c,p}$ is the species of the selected particle, $V^{\rm a}$ is the volume of the donor box and $V^{\rm b}$ is the volume of the recipient box.

In addition, volume changes of the boxes are used to satisfy the condition of equal pressure in both subsystems. We hence perform a random walk in $\ln(V_a/V_b)$ with the acceptance probability

$$\mathscr{P} = \min\left\{1, \mathscr{R}\exp[-\beta(\mathrm{U_{new}}-\mathrm{U_{old}})]\right\}, \tag{4.6}$$

where

$$\mathscr{R} = \left(\frac{V^{\rm a}_{\rm new}}{V^{\rm a}_{\rm old}}\right)^{N^{\rm a}_{\rm c}+N^{\rm a}_{\rm p}+1} \left(\frac{V^{\rm b}_{\rm new}}{V^{\rm b}_{\rm old}}\right)^{N^{\rm b}_{\rm c}+N^{\rm b}_{\rm p}+1}, \tag{4.7}$$

and with the condition that the total volume $V = V^{\rm a}_{\rm old} + V^{\rm b}_{\rm old} = V^{\rm a}_{\rm new} + V^{\rm b}_{\rm new}$ is constant , where the subscript old (new) marks quantities before (after) the trial move.

Phase equilibria in confined geometries, like e.g. inside slit pores as considered here, can be determined by either determining the adsorption isotherm in simulation or by employing the GEMC simulation method extended to a slit pore [91]. In the first method, the pore is coupled to a reservoir of bulk fluid. The adsorption of the fluid inside the pore is then measured at constant temperature for different bulk densities of the reservoir, i.e. the chemical potentials of the various species are fixed. A jump in the adsorption isotherm corresponds to capillary condensation or evaporation in the slit pore. However, this method is inaccurate for determining phase coexistence due to hysteresis.

In order to determine the binodal lines, we hence employ the GEMC method adapted to a slit pore [91]: Two separate simulation boxes are simulated, one containing the confined gas and one containing the confined liquid. Each box has periodic boundary conditions in both directions parallel to the walls. Capillary coexistence implies equality of temperature, chemical potentials for both species as well as equality of the wall-fluid interfacial tension. Fulfilling the first two conditions is performed similar to the procedure for determining bulk phase equilibria, i.e. using particle displacements with acceptance probability given by Eq. (4.3) and particle transfers with acceptance probability given by

Eq. (4.5). We satisfy the third requirement of equal wall-fluid interfacial tension in both phases by exchanging wall area (and hence volume) between the two boxes, while fixing both the wall separation distance H in each box as well as the total lateral area of both boxes $A^{\mathrm{a}} + A^{\mathrm{b}} = A$ is constant, with A^{a} and A^{b} the area of the subsystems a and b, respectively. A random walk in $\ln(A^{\mathrm{a}}/A^{\mathrm{b}})$ is then performed with an acceptance probability given by

$$\mathscr{P} = \min\left\{1, \mathscr{R}\exp[-\beta(\mathrm{U}_{\mathrm{new}} - \mathrm{U}_{\mathrm{old}})]\right\}, \tag{4.8}$$

with

$$\mathscr{R} = \left(\frac{A^{\mathrm{a}}_{\mathrm{new}}}{A^{\mathrm{a}}_{\mathrm{old}}}\right)^{N^{\mathrm{a}}_{\mathrm{c}}+N^{\mathrm{a}}_{\mathrm{p}}+1} \left(\frac{A^{\mathrm{b}}_{\mathrm{new}}}{A^{\mathrm{b}}_{\mathrm{old}}}\right)^{N^{\mathrm{b}}_{\mathrm{c}}+N^{\mathrm{b}}_{\mathrm{p}}+1}. \tag{4.9}$$

We determine the fugacities of the colloids and of the polymers by applying the GEMC version of the particle insertion method [92]

$$z_k^{\mathrm{a,b}} = \left\langle \frac{V^{\mathrm{a,b}}}{N_k^{\mathrm{a,b}}+1}\exp[-\beta\Delta U]\right\rangle^{-1} \quad k = \mathrm{c,p} \tag{4.10}$$

where a, b label the two simulation boxes and ΔU is the energy defined by the acceptance rule of Eq. (4.5). We determine the densities of the two coexisting phases by sampling histograms of the probability density $P(\eta_{\mathrm{c}}, \eta_{\mathrm{p}})$ to observe the packing fractions η_{p} and η_{c} for the polymers and colloids, respectively. The two maxima of $P(\eta_{\mathrm{c}}, \eta_{\mathrm{p}})$ correspond to the coexisting packing fractions in the thermodynamic limit [92]. Statistical uncertainties of the sampled quantities were determined by performing three or four independent sets of simulations. The standard deviation of the results from the simulation sets was used as the error estimate.

4.4 Kelvin equation for binary mixtures

We derive expressions for the shift in chemical potentials for the gas-liquid binodal of a binary mixture confined between parallel plates assuming knowledge of bulk quantities like the bulk coexisting densities, the chemical potentials at bulk coexistence, and the liquid-wall and gas-wall interfacial tensions, γ_{wl} and γ_{wg}, respectively. Using a macroscopic picture we employ the grand potential of the mixture confined in a slit of two parallel walls with area A and separation distance h between the two walls [1]

$$\Omega(\mu_{\mathrm{c}}, \mu_{\mathrm{p}}) = Ah\omega(\mu_{\mathrm{c}}, \mu_{\mathrm{p}}) + 2A\gamma(\mu_{\mathrm{c}}, \mu_{\mathrm{p}}, h), \tag{4.11}$$

where μ_{c} and μ_{p} are the chemical potentials of colloids and polymers, respectively, ω is the bulk grand potential density (per unit volume), and 2γ is the interfacial tension of the mixture and the plates at distance h. For large h, we can approximate the latter quantity by twice the interfacial tension of the mixture in contact with a single wall, e.g., $2\gamma_{\mathrm{w}\alpha}(\mu_{\mathrm{c}}, \mu_{\mathrm{p}})$,

[1] We will discuss the relationship of h to our model parameter H (see Sec. 4.2) in more detail in Sec. 4.5.5.

where α=l,g are for the liquid and the gas phase, respectively. The aim is to predict the grand potential in the capillary given the knowledge of the thermodynamics of the bulk at coexistence, i.e. at a statepoint specified through the bulk values of the chemical potentials μ_c^* and μ_p^*. Hence, we can reexpress the chemical potentials of both species for the confined fluid as $\mu_c = \mu_c^* + \Delta\mu_c$ and $\mu_p = \mu_p^* + \Delta\mu_p$. Quantities at coexistence carry a superscript $\alpha = l, g$, where l, g indicate liquid and gas respectively.

The thermodynamic relations for the bulk densities of the colloids and polymers, ρ_c and ρ_p, respectively, read

$$\rho_c = -\left.\frac{\partial\omega}{\partial\mu_c}\right|_{\mu_p}, \quad \rho_p = -\left.\frac{\partial\omega}{\partial\mu_p}\right|_{\mu_c}, \tag{4.12}$$

while the (excess) adsorption of the colloids and the polymers, Γ_c and Γ_p, are given by

$$\Gamma_c = \left.\frac{\partial\gamma_{w\alpha}}{\partial\mu_c}\right|_{\mu_p}, \quad \Gamma_p = \left.\frac{\partial\gamma_{w\alpha}}{\partial\mu_p}\right|_{\mu_c}. \tag{4.13}$$

Using Eqs. (4.12) and (4.13), we can perform a Taylor expansion of the right hand side of Eq. (4.11)

$$\begin{aligned}\frac{1}{Ah}\Omega(\mu_c,\mu_p) \approx \quad & \omega(\mu_c^*,\mu_p^*) - \rho_c^\alpha\Delta\mu_c - \rho_p^\alpha\Delta\mu_p \\ & + \frac{2}{h}\Big[\gamma_{w\alpha} + \Gamma_c^\alpha\Delta\mu_c + \Gamma_p^\alpha\Delta\mu_p\Big],\end{aligned} \tag{4.14}$$

where the bulk densities, ρ_c^α and ρ_p^α, and the (excess) adsorptions, Γ_c^α and Γ_p^α, are evaluated in one of the coexisting phases $\alpha = l, g$ at the statepoint given by μ_c^* and μ_p^*.

We next consider the capillary to be at phase coexistence, i.e. we might envisage *two* capillaries in contact with each other, one being filled with gas, the other being filled with liquid. Phase equilibrium between both capillaries implies equality of the chemical potential of each species and of the grand potential in both phases,

$$\Omega_g(\mu_c,\mu_p) = \Omega_l(\mu_c,\mu_p), \tag{4.15}$$

where Ω_g and Ω_l is the grand potential of the gas and the liquid phase, respectively. Using the approximation (4.14) in (4.15) yields

$$\begin{aligned}& \Big(\rho_c^l - \rho_c^g - \frac{2}{h}(\Gamma_c^l - \Gamma_c^g)\Big)\Delta\mu_c \\ + \quad & \Big(\rho_p^l - \rho_p^g - \frac{2}{h}(\Gamma_p^l - \Gamma_p^g)\Big)\Delta\mu_p \\ = \quad & \frac{2}{h}\Big(\gamma_{wl}(\mu_c^*,\mu_p^*) - \gamma_{wg}(\mu_c^*,\mu_p^*)\Big).\end{aligned} \tag{4.16}$$

In the limit h is large compared with the microscopic lengths and that the adsorptions remain finite, we can neglect the terms proportional to $(\Gamma_i^l - \Gamma_i^g)/h$. Hence, Eq. (4.16) simplifies to

$$\big(\rho_c^l - \rho_c^g\big)\Delta\mu_c + \big(\rho_p^l - \rho_p^g\big)\Delta\mu_p = \frac{2}{h}\Big(\gamma_{wl} - \gamma_{wg}\Big), \tag{4.17}$$

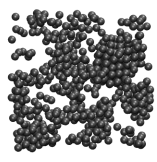

which constitutes a single equation for the two unknown shifts in the chemical potentials, $\Delta\mu_c$ and $\Delta\mu_p$. In order to obtain a closed system of equations one requires another assumption. We will present three different approaches in the following. Each approach can be viewed as a different choice of an "optimal" bulk reference state as illustrated in Fig. 4.2. A comparison with the numerical results will be presented in Sec. 4.5.5.

4.4.1 Constant Polymer Chemical Potential

The bulk reference state is chosen to be at the same polymer chemical potential. This requirement is similar to imposing the same temperature in a simple substance. The optimal bulk reference state with the same chemical potential of polymers leads to

$$\Delta\mu_p = 0. \tag{4.18}$$

Eqs. (4.17) and (4.18) readily yield a one-component Kelvin equation

$$\Delta\mu_c = \frac{2}{h}\frac{\gamma_{wl} - \gamma_{wg}}{\rho_c^l - \rho_c^g}. \tag{4.19}$$

Clearly this result can be obtained with less labour by directly dealing with the effective one-component system of colloids interacting with a depletion potential, and rather serves as a illustration for the validity of the reasoning leading to Eq. (4.17).

4.4.2 Constant Pressure

This reference state was used by Evans and Marini Bettolo Marconi in Ref. [50]. The bulk reference state is chosen to possess the same pressure. In order to derive a corresponding condition consider the (finite difference version of the) Gibbs-Duhem relation

$$(S/V)\Delta T - \Delta P + \rho_c\Delta\mu_c + \rho_p\Delta\mu_p = 0, \tag{4.20}$$

where S is the entropy. Clearly, for athermal systems $\Delta T = 0$. We use (4.20) to compare the statepoint at capillary coexistence with the reference statepoint at bulk coexistence that possesses the same pressure, i.e. $\Delta P = 0$, hence

$$\Delta\mu_p = -\frac{\rho_c^\alpha}{\rho_p^\alpha}\Delta\mu_c, \quad \alpha = g, l. \tag{4.21}$$

As shown in Fig. 4.2 the constant pressure paths (for which the Gibbs-Duhem relation is a good approximation close to the bulk binodal) have a discontinuity at bulk coexistence. To predict the capillary phase behavior for statepoints that lie on the gas side of the bulk gas-liquid binodal (hence to predict capillary *condensation*), the correct reference state is the coexisting *gas phase*, and we use (4.21) with $\alpha = g$. Together with (4.17) we obtain the classic result for capillary condensation,

$$\begin{aligned} \Delta\mu_c &= \frac{2}{h}\frac{\gamma_{wl} - \gamma_{wg}}{\rho_c^l - (\rho_c^g/\rho_p^g)\rho_p^l}, \\ \Delta\mu_p &= \frac{2}{h}\frac{\gamma_{wl} - \gamma_{wg}}{\rho_p^l - (\rho_p^g/\rho_c^g)\rho_c^l}. \end{aligned} \tag{4.22}$$

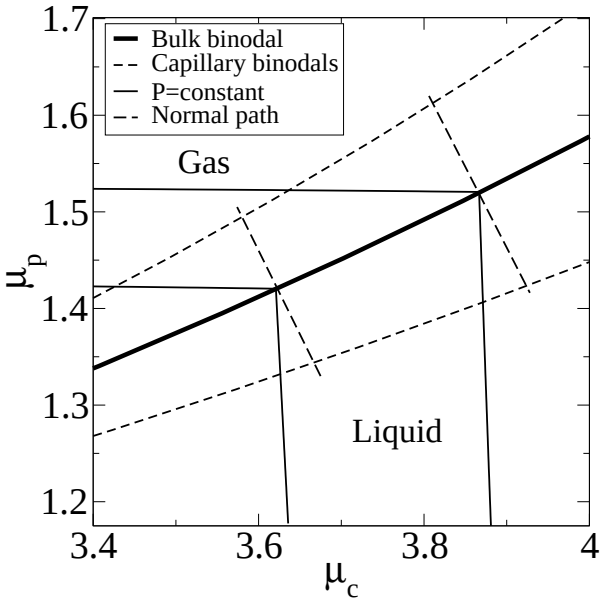

Figure 4.2: Phase diagram of the AOV model with size ratio $q = \sigma_p/\sigma_c = 1$ as a function of the colloidal chemical potential μ_c and the polymer chemical potential μ_p. The bulk binodal from free volume theory (thick continuous curve) is shown along with isobaric lines (thin continuous curves) for two bulk reference points. The thick dashed curves indicate the normal paths for the same reference points. The thin dashed curves are an illustration of the possible prediction of the Kelvin equation for the capillary binodals. For clarity we omitted the paths with constant polymer chemical potential.

Alternatively, predicting the capillary phase behavior for statepoints that lie on the liquid side of the bulk gas-liquid binodal (and to predict capillary *evaporation*), we choose the coexisting *liquid phase* as a reference. Eq. (4.21) with $\alpha = \mathrm{l}$ together with Eq. (4.17) leads to the following result for capillary evaporation

$$\begin{aligned} \Delta\mu_c &= -\frac{2}{h}\frac{\gamma_{wl}-\gamma_{wg}}{\rho_c^g-(\rho_c^l/\rho_p^l)\rho_p^g}, \\ \Delta\mu_p &= -\frac{2}{h}\frac{\gamma_{wl}-\gamma_{wg}}{\rho_p^g-(\rho_p^l/\rho_c^l)\rho_c^g}. \end{aligned} \tag{4.23}$$

The derivation presented here yields the same results as given in Ref. [50], where a single capillary is considered in contact with a bulk reservoir. We note that this procedure leads to two different equations for the two phenomena of capillary condensation and evaporation.

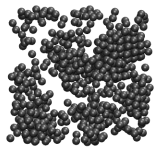

4.4.3 Normal Path Relation

As a third and novel alternative we choose the reference state such that the statepoint of interest lies on a path in the phase diagram that crosses the bulk liquid-gas binodal in perpendicular (or normal) direction in the plane of chemical potentials. This implies optimizing proximity in the $\mu_c - \mu_p$ plane between both statepoints.

The corresponding relation can readily be established starting from the relation of the slope of the bulk binodal to the difference in coexisting densities,

$$\left.\frac{d\mu_{\rm c}}{d\mu_{\rm p}}\right|_{\rm coex} = -\frac{\rho_{\rm p}^{\rm l} - \rho_{\rm p}^{\rm g}}{\rho_{\rm c}^{\rm l} - \rho_{\rm c}^{\rm g}}. \tag{4.24}$$

Hence a path normal to the bulk binodal is given by

$$\left.\frac{d\mu_{\rm c}}{d\mu_{\rm p}}\right|_{\rm normal} = \frac{\rho_{\rm c}^{\rm l} - \rho_{\rm c}^{\rm g}}{\rho_{\rm p}^{\rm l} - \rho_{\rm p}^{\rm g}}, \tag{4.25}$$

from which we deduce the finite-difference version

$$\Delta\mu_{\rm p} = \frac{\rho_{\rm p}^{\rm l} - \rho_{\rm p}^{\rm g}}{\rho_{\rm c}^{\rm l} - \rho_{\rm c}^{\rm g}}\Delta\mu_{\rm c}, \tag{4.26}$$

which, together with Eq. (4.17) yields

$$\begin{aligned}
\Delta\mu_{\rm c} &= \frac{2}{h}(\gamma_{\rm wl} - \gamma_{\rm wg})\frac{\rho_{\rm c}^{\rm l} - \rho_{\rm c}^{\rm g}}{(\rho_{\rm c}^{\rm l} - \rho_{\rm c}^{\rm g})^2 + (\rho_{\rm p}^{\rm l} - \rho_{\rm p}^{\rm g})^2}, \\
\Delta\mu_{\rm p} &= \frac{2}{h}(\gamma_{\rm wl} - \gamma_{\rm wg})\frac{\rho_{\rm p}^{\rm l} - \rho_{\rm p}^{\rm g}}{(\rho_{\rm c}^{\rm l} - \rho_{\rm c}^{\rm g})^2 + (\rho_{\rm p}^{\rm l} - \rho_{\rm p}^{\rm l})^2},
\end{aligned} \tag{4.27}$$

valid both for capillary condensation and evaporation. As shown in Fig. 4.2 the normal paths are symmetric with respect to the gas and liquid side of the bulk binodal. The somewhat subtle choice of the reference state, which is different for the two phenomena in section 4.4.2, resulting in using either Eq. (4.22) or Eq (4.23) is now avoided. The procedure described here leads to one equation, which can be used for both phenomena. This might be advantageous for mixtures where the corresponding phases are less obvious, like e.g. confined liquid crystals.

4.5 Results

In this section, we focus on AOV colloid-polymer mixtures with a size ratio $q = 1$, a previously well-studied and also experimentally accessible case. We have performed GEMC simulations with 4×10^8 steps discarding the initial 10^8 steps for equilibration. The acceptance probability of particle displacement was kept around 10% to 20%, the acceptance probability for volume exchanges was around 50%, while the acceptance probability for transfer of particles was strongly dependent on the statepoint and varied between 50% and

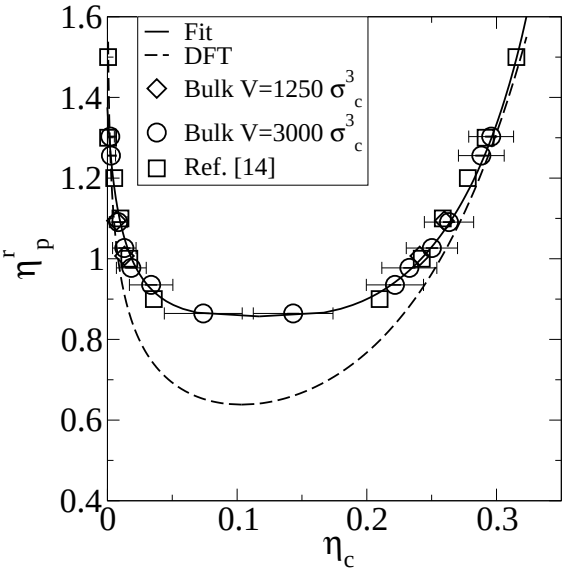

Figure 4.3: Bulk phase diagram of the AOV model with size ratio $q = \sigma_p/\sigma_c = 1$ as a function of the colloidal packing fraction η_c and the polymer reservoir packing fraction η_p^r. Coexistence is along the horizontal tie lines (not shown). Shown are GEMC simulation results for volumes $V = 3000\sigma_c^3$ (circles) and $V = 1250\sigma_c^3$ (diamonds), as well as the simulation results from Ref. [14] (squares). We also display the result of the fit of Eqs. (4.28) and (4.29) (solid line) to the simulation data to and the binodal obtained from DFT, or, equivalently, free volume theory (dashed line).

5% for the polymers and from 10% to less than 0.1% for the colloids. Fig. 4.3 shows the bulk phase diagram obtained from simulations with a simulation box of volume $V = 3000\sigma_c^3$. Simulation runs with smaller system sizes display negligible finite size effects. In the η_c-η_p^r representation, the shape of the binodal is similar to that of a simple fluid upon identifying η_p^r with inverse temperature. The tielines, connecting the coexisting phases, are horizontal (not shown) as η_p^r possesses the same value in the two coexisting phases. We have checked that our results agree well with those obtained by Dijkstra and van Roij [14] who performed simulations of an effective one component system, which was obtained by formally integrating out the degrees of freedom of the polymers in the partition function.

To estimate the location of the critical point, we fitted the binodals using the scaling law

$$\eta_c^l - \eta_c^g = A\left(\frac{1}{(\eta_p^r)_{crit}} - \frac{1}{\eta_p^r}\right)^\beta \tag{4.28}$$

and the law of rectilinear diameter

$$\eta_c^l + \eta_c^g = 2(\eta_c)_{crit} + B\left(\frac{1}{(\eta_p^r)_{crit}} - \frac{1}{\eta_p^r}\right), \tag{4.29}$$

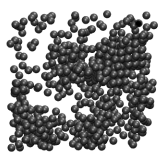

where η_c^l is the colloid packing fraction of the coexisting liquid phase, η_c^g is the colloid packing fraction of the coexisting gas phase and the subscript "crit" indicates the value at the critical point. A and B are two free parameters determined from the fit, and $\beta = 0.32$ is the three-dimensional Ising critical exponent. We used the standard functional form of the two laws [18] but replaced the temperature by the inverse of the polymer reservoir packing fraction. The continuous curve in Fig. 4.3 is the result of the fit of Eqs. (4.28) and (4.29). The fit is remarkably good, but we point out that this only gives an estimate of the critical point. To get a more precise value of the critical packing fractions, it would be necessary to carry out simulations in a region of the phase diagram much closer to the critical point than is possible with GEMC.

In Fig. 4.3, we also compare our results with those obtained from density functional theory (DFT). We use the approximation for the Helmholtz excess free energy for the AOV model as given in [46]. For given external potential, the density functional is numerically minimized using a standard iteration procedure. The discrepancies between theory and simulation can be understood by considering that the DFT for homogeneous (bulk) fluid states of the AOV model is equivalent to the free volume theory of Lekkerkerker et al. [30]. Dijkstra et al. [43] showed that this theory is equivalent to a first order Taylor expansion of the free energy around $\eta_p^r = 0$

$$\begin{aligned} \beta F(N_c, V, \eta_p^r) &= \beta F(N_c, V, \eta_p^r = 0) + \int_0^{\eta_p^r} d(\eta_p^r)' \left(\frac{\partial \beta F(N_c, V, (\eta_p^r)')}{\partial (\eta_p^r)'} \right)_{(\eta_p^r)'} \\ &\simeq \beta F(N_c, V, \eta_p^r = 0) - \frac{6}{\pi \sigma_p^3} \eta_p^r < V_{\text{free}} >_{\eta_p^r = 0}, \end{aligned} \tag{4.30}$$

neglecting terms $\mathcal{O}((\eta_p^r)^2)$ and where $\langle V_{\text{free}} \rangle_{\eta_p^r = 0}$ is the free volume available for the polymer in the pure hard-sphere reference system. It is evident in Fig. 4.3 that the theory (dashed curve) performs better at high η_c where the system is so crowded that it resembles the reference hard-sphere system and $\langle V_{\text{free}} \rangle_{(\eta_p^r)' = 0} \simeq \langle V_{\text{free}} \rangle_{(\eta_p^r)' = \eta_p^r}$. For very small η_c the free volume is close to the total volume of the system V for both the pure hard-sphere reference system and the actual mixture. For high η_p^r, the gas-liquid coexistence is very broad and quantitatively well-predicted by the theory. The critical point of the AOV mixture for size ratio $q = 1$ is in the region of $\eta_c \sim 0.1$ and the theory underestimates the critical value of η_p^r. Furthermore, the discrepancy in location of the critical point arises from the mean-field critical exponent of the theory against the 3D Ising critical exponent of the simulation [93].

4.5.1 Phase diagrams

First we present the results for the colloid-polymer mixtures confined between two smooth, planar hard walls at distance H. In Fig. 4.4(a) we show a set of phase diagrams for $H/\sigma_c = \infty$ (bulk), 10, 5, 3, and 2, in the η_c-η_p^r representation. Upon decreasing the plate separation distance H/σ_c, the critical value of η_p^r shifts to higher values, in accordance with the decrease in critical temperature of simple fluids. The theoretical binodals agree well with those from simulation, except close to the critical point. The theory underestimates for

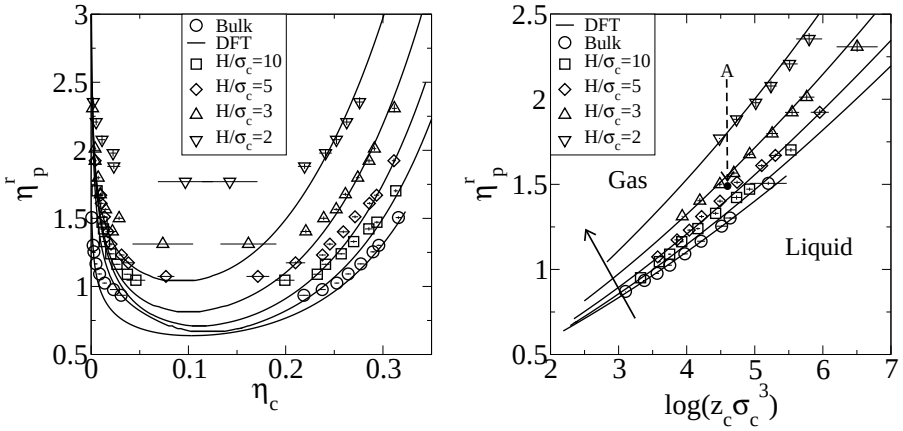

Figure 4.4: Capillary phase diagram of the AOV model with size ratio $q = \sigma_p/\sigma_c = 1$ confined between parallel hard walls with separation distance H/σ_c=2, 3, 5, 10 and ∞. (a) As a function of colloid packing fraction η_c and polymer reservoir packing fraction η_p^r. Shown are results from simulation (symbols) and DFT (continuous lines).(b) As a function of colloid fugacity $z_c\sigma_c^3$ and polymer reservoir packing fraction η_p^r. Statepoint A is in the gas region of the phase diagram for wall separation distances $H/\sigma_c = \infty$, 10, and 5 and in the liquid region of the phase diagram for wall separation distances H/σ_c = 3 and 2. The arrow indicates the direction of the binodal shift upon increasing confinement (decreasing values of H/σ_c) of the mixture between parallel hard walls.

all plate separations the critical value of η_p^r, as it does for the bulk system [14]. We observe that the deviation increases upon decreasing H/σ_c. In Tab. 4.1 we show the critical packing fractions obtained from the fit of Eqs. (4.28) and (4.29) and from DFT. We used the 3-dimensional Ising critical exponent for all wall separations. Although recent studies [94] suggests a critical behavior for small wall separations that is neither three-dimensional, nor two-dimensional, the difference is likely to be negligible at the level of precision of our GEMC simulations.

In Fig. 4.4(b) we show a set of phase diagrams for $H/\sigma_c = \infty$, 10, 5, 3, and 2 in the z_c-η_p^r representation. The coexistence gap in colloid packing fractions collapses to a line since two phases at coexistence possess the same colloid fugacity. Note that the system is in the gas phase for fugacity $z_c < z_c^{sat}$, while it is in the liquid phase for $z_c > z_c^{sat}$, where z_c^{sat} denotes the colloid fugacity at bulk coexistence. Statepoint A is gas-like for $H/\sigma_c \geq 5$, but is liquid-like for $H/\sigma_c \leq 3$. Hence, planar slits with $H/\sigma_c \leq 3$ are filled with liquid phase, while the bulk reservoir is in the gas phase, proving the occurrence of capillary condensation upon reducing the width of the slit that is in contact with a bulk gas. Figs. 4.5(a),(b) shows typical colloid-polymer configurations of a coexisting colloidal liquid and gas phase confined between parallel hard walls at a distance H/σ_c=10.

We now turn our attention to colloid-polymer mixtures confined between two smooth, planar semi-permeable walls at distance H_c. In Fig. 4.6(a) we show a set of phase diagrams for $H_c/\sigma_c = \infty$, 10, 4, and 2 in the η_c-η_p^r representation. Upon increasing the confinement

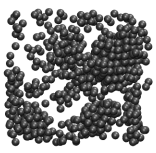

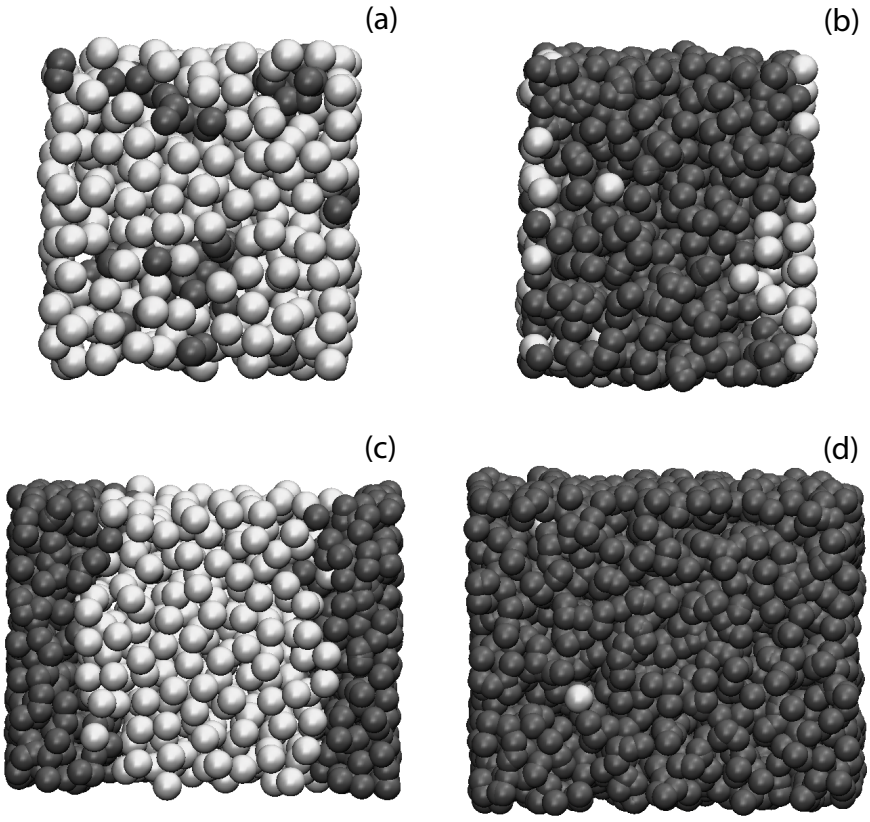

Figure 4.5: Snapshots from computer simulations of the model colloid-polymer mixture with a polymer-colloid size ratio $q = \sigma_p/\sigma_c = 1$. Colloids (light grey) and polymers (dark grey) are immersed between two parallel plates. (a), (b) Hard walls with separation distance $H/\sigma_c = 10$ and orientation perpendicular to the horizontal axis. Shown is the confined colloidal liquid phase (a) in coexistence with the confined colloidal gas phase (b). The polymer reservoir packing fraction is $\eta_p^r = 1.088$. (c), (d) Semi-permeable walls with separation distance $H_c/\sigma_c = 10$, and orientation perpendicular to the horizontal axis. Shown is the confined colloidal liquid phase (c) in coexistence with the confined colloidal gas phase (d). The polymer reservoir packing fraction is $\eta_p^r = 1.394$.

Table 4.1: Capillary critical points of the AOV model between parallel hard walls with separation distance $H/\sigma_c = \infty, 10, 5, 3$, and 2 obtained from simulations using the fit of Eqs. (4.28) and (4.29), and from DFT.

H/σ_c	$(\eta_p^r)_{crit}$	$(\eta_c)_{crit}$	DFT $(\eta_p^r)_{crit}$	DFT $(\eta_c)_{crit}$
∞	0.86(1)	0.117(2)	0.638	0.103
10	1.00(1)	0.124(1)	0.670	0.120
5	1.09(1)	0.123(2)	0.710	0.111
3	1.27(2)	0.116(3)	0.815	0.100
2	1.76(2)	0.119(1)	1.044	0.091

(via reduction of H_c/σ_c), the critical value of η_p^r shifts to higher values. The trend is similar to the behavior of the slit with hard walls, although we find a smaller shift of the critical point (see Tab. 4.2). In Fig. 4.6(b) we show a set of phase diagrams for $H/\sigma_c = \infty, 10, 4$, and 2 in the z_c-η_p^r representation. Statepoint B is liquid-like for $H_c/\sigma_c \geq 10$, but is gas-like for $H_c/\sigma_c \leq 2$. Hence, planar slits with $H_c/\sigma_c \leq 2$ are filled with gas, while the bulk reservoir is in the liquid phase, indicating the occurrence of capillary evaporation. Typical colloid-polymer configurations of the colloidal liquid phase in coexistence with the colloidal gas phase immersed between two parallel semi-permeable walls with H_c/σ_c=10, are shown in Fig. 4.5(c),(d).

Table 4.2: Capillary critical points of the AOV model between parallel semi-permeable plates with separation distance $H/\sigma_c = \infty, 10, 4$, and 2 obtained from simulations using the fit of Eqs. (4.28) and (4.29), and from DFT.

H/σ_c	$(\eta_p^r)_{crit}$	$(\eta_c)_{crit}$	DFT $(\eta_p^r)_{crit}$	DFT $(\eta_c)_{crit}$
∞	0.86(1)	0.117(2)	0.638	0.103
10	1.09(2)	0.13(1)	0.660	0.075
4	1.11(4)	0.10(3)	0.699	0.076
2	1.29(1)	0.11(4)	0.818	0.092

4.5.2 Structure at coexistence

We next analyze the density profiles of both species at capillary coexistence of gas and liquid phases. Such fluid states are translationally invariant against lateral displacements, and the density distributions (of both species) depend solely on the (perpendicular) distance from the walls. We compare theoretical and simulation results for coexistence states at the same values for η_p^r. In practice, we have used the result for η_p^r from the simulations, and have calculated the corresponding DFT profiles. The value for z_c used in the DFT calculations was adjusted according to the respective theoretical capillary binodal. Recall that the quantitative differences in results for the capillary binodals from simulation and theory are small.

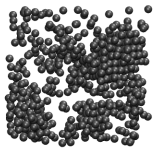

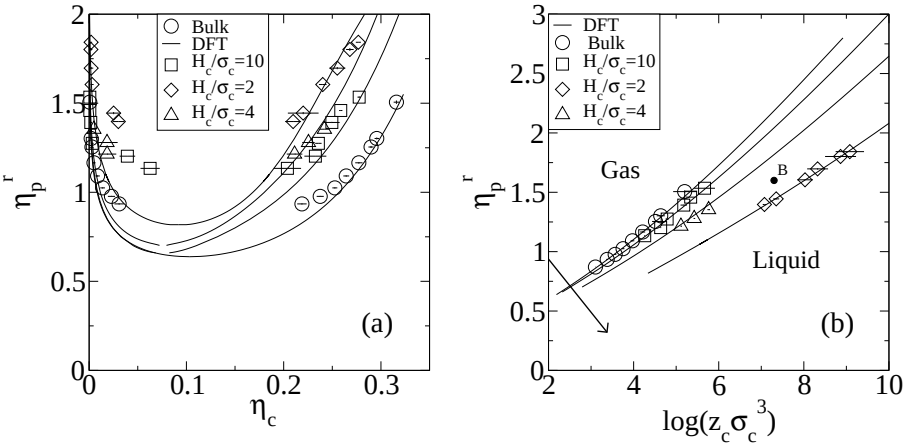

Figure 4.6: Capillary phase diagram showing the gas-liquid binodal for the AOV model with $q = \sigma_p/\sigma_c = 1$ between two parallel semi-permeable walls with separation distances H_c/σ_c=2, 4, 10, ∞. (a) As a function of colloid packing fraction η_c and polymer reservoir packing fraction η_p^r. Shown are results from simulations (symbols) and DFT (lines). (b) As a function of colloid fugacity $z_c\sigma_c^3$ and polymer reservoir packing fraction η_p^r. The arrow indicates the direction of the shift of the binodal upon increasing confinement of the mixture (decreasing values of H_c/σ_c) between two parallel semi-permeable walls.

The results for a slit of hard walls are shown in Fig. 4.7. The colloidal profiles in the liquid phase display strong layering at either wall. For a wall separation $H/\sigma_c = 10$, at $\eta_p^r = 1.23 \pm 0.01$, and $z_c\sigma_c^3 = 66.3 \pm 0.1$ these oscillations decay to flat, bulk-like behavior in the center of the slit. For smaller wall separations, namely $H/\sigma_c = 5$, at $\eta_p^r = 1.39 \pm 0.01$, and $z_c\sigma_c^3 = 99.4 \pm 0.3$, $H/\sigma_c = 3$, at $\eta_p^r = 1.68 \pm 0.01$, and $z_c\sigma_c^3 = 128 \pm 2$, and $H/\sigma_c = 2$, at $\eta_p^r = 2.23 \pm 0.01$, and $z_c\sigma_c^3 = 228 \pm 10$, we observe the presence of 5, 3, and 2 well-defined layers of particles, respectively. Although their density is much lower, the polymers in the liquid phase display similar behavior. The layering is weaker, but we can observe that a maximum in the colloid profile corresponds also to a maximum in the polymer profile. This result suggests that for such low concentrations polymers behave as hard spheres as packing effects are concerned. In the gas phase, for wall separations $H/\sigma_c = 10$ and 5, we find strong adsorption of the colloids at both walls, (see also the snapshot in Fig. 4.5(b)), and a tendency of the polymers to desorb from the walls. In the center of the slit almost no colloids are present and the polymers display flat density profiles with a packing fraction very similar to the polymer reservoir packing fraction. For wall separation distances $H/\sigma_c = 3$ and 2, we observe an almost flat polymer density profile, while the density of the colloids is very low throughout the slit. Different from the liquid profiles, a maximum in the colloidal profile corresponds to a minimum of the polymer profiles.

Fig. 4.8 displays density profiles for the slit of semi-permeable walls. For wall separation distance of $H_c/\sigma_c = 10$, at $\eta_p^r = 1.39 \pm 0.01$, and $z_c\sigma_c^3 = 167 \pm 5$, we clearly observe for the liquid state points the presence of a gas layer between the wall and the liquid phase

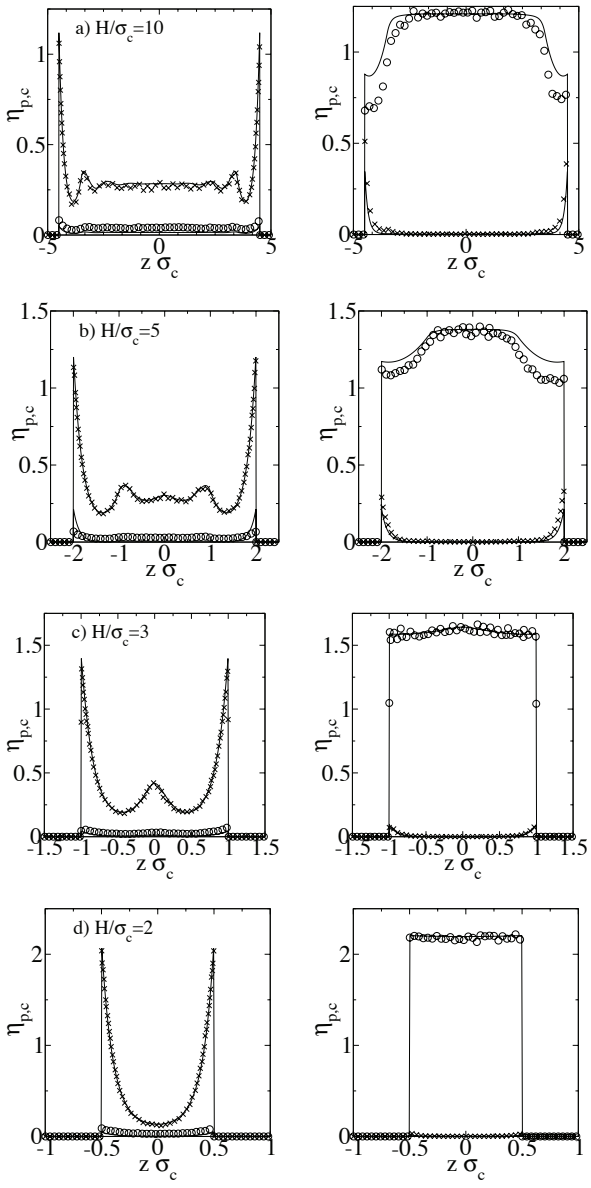

Figure 4.7: Density profiles of the coexisting liquid (left) and gas (right) phases of the AOV model confined between parallel hard walls with separation distance: a) H/σ_c=10, at η_p^r=1.23(1), $z_c\sigma_c^3$=66.3(1), b) H/σ_c=5 at η_p^r=1.39(1), $z_c\sigma_c^3$=99.4(3), c) H/σ_c=3, at η_p^r=1.68(1), $z_c\sigma_c^3$=128(2), and d) H/σ_c=2, at η_p^r=2.23(1), $z_c\sigma_c^3$=228(10). Shown are results from simulations for the density profiles of the colloids (crosses) and polymers (circles), along with results from DFT (full lines).

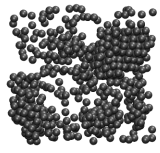

centered in the slit. For wall separation $H_c/\sigma_c = 4$, at $\eta_p^r = 1.35 \pm 0.01$, and $z_c\sigma_c^3 = 318 \pm 10$ the gas layers at the walls disappear and indications of layering effects appear. For wall separation $H_c/\sigma_c = 2$, at $\eta_p^r = 1.61 \pm 0.01$, and $z_c\sigma_c^3 = 2950 \pm 200$ the colloid density profile displays very significant peaks at both walls. Moreover, we do find layering at larger wall separations, for statepoints well inside the liquid phase. We will discuss this in more detail in the next section. In the gas phase, the density of colloids is very low throughout the slit, while the polymer density profile is almost flat with a packing fraction close to the polymer reservoir packing fraction.

The comparison between DFT and simulation indicates good agreement of results from both approaches. Differences in structure can be traced back to differences in the phase diagrams. For fixed η_p^r the DFT predicts higher colloid densities and smaller polymer densities, and these differences are reflected by the discrepancies in the profiles. For wall separations where the statepoint is close to the critical point the agreement is worse, especially close to the walls. Such discrepancies between simulation and DFT were present also for the wall-fluid tension and the adsorption of colloid-polymer mixtures studied in chapter 2.

4.5.3 Structure off-coexistence

We next consider density profiles for a fixed statepoint off-coexistence. For slits with hard walls we chose statepoint A (η_p^r=1.49 and $\ln(z_c\sigma_c^3)$=4.6) of Fig. 4.4(b), that lies in the stable gas region of the bulk phase diagram. We carried out simulations for wall separation distances $H/\sigma_c = 10, 5, 3$, and 2. Fig. 4.9 shows that for wall separations $H/\sigma_c = 10$ and 5 the slit is filled with gas. However, for wall separation of $H/\sigma_c = 3$ we observe that the capillary fills with liquid. Hence, for this particular statepoint, the critical wall separation distance for capillary condensation lies between 3 and 5 colloid diameters, consistently with the findings of Sec. 4.5.1. Reducing the wall separation to $H/\sigma_c = 2$, the liquid phase remains stable. The density profiles in the gas phase possess adsorption peaks in the colloid profile, and corresponding desorption peaks in the polymer profiles. In the liquid phase we observe strong layering of the colloids, and, to a lesser extent, of the polymers. The agreement between simulation and DFT results is good. The differences seem to be related to the vicinity of statepoint A to the critical point. The critical point for wall separation $H/\sigma_c = 3$, and 5, is much closer to statepoint A than the critical points for wall separations $H/\sigma_c = 10$, and 2, where we find a better agreement between simulation and theory profiles.

We next discuss the structure of the mixture inside the slit with semi-permeable walls (Fig. 4.10). We fix the fugacities of both species to those at statepoint B (η_p^r=1.60 and $\ln(z_c\sigma_c^3)$=7.3), see Fig. 4.6(b). The statepoint B is in the liquid part of the bulk phase diagram phase. The liquid fills slits with wall separations $H_c/\sigma_c = 10$, and 4, while for $H_c/\sigma_c = 2$ the slit is filled with gas. This is an indication of capillary evaporation consistent with the findings of Sec. 4.5.1. The liquid phase is characterized by structureless polymer profiles, and a layering of colloids for both $H_c/\sigma_c = 10$, and 4. Note that we did not observe such layering for the statepoints at coexistence (see previous section). Simulation and theory are in good agreement at all wall separations.

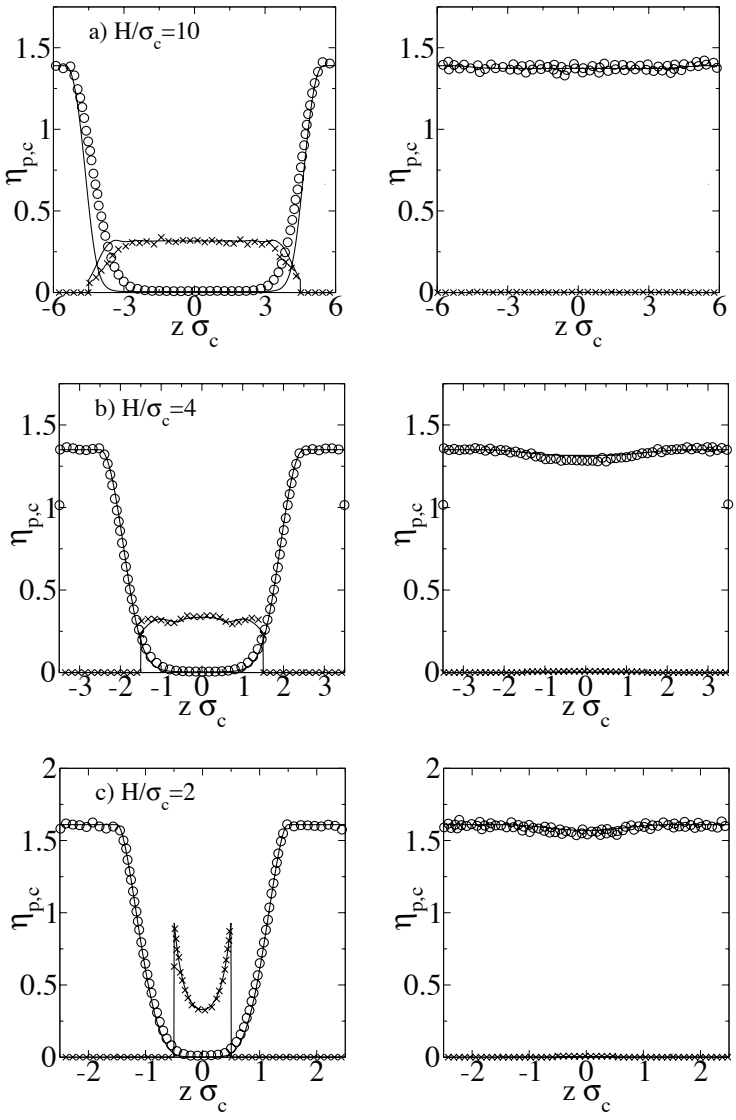

Figure 4.8: Density profiles of the coexisting liquid (left) and gas (right) phases of the AOV model confined between two parallel semi-permeable walls with varying separation distance: a) H_c/σ_c=10, at η_p^r=1.39(1), $z_c\sigma_c^3$=167(5), b) H_c/σ_c=4, at η_p^r=1.35(1), $z_c\sigma_c^3$=318(10), and c) H_c/σ_c=2, at η_p^r=1.61(1), $z_c\sigma_c^3$=2950(200). Shown are results from simulations for the density profiles of the colloids (crosses) and polymers (circles), and results from DFT (full lines).

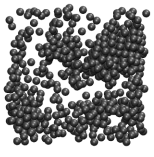

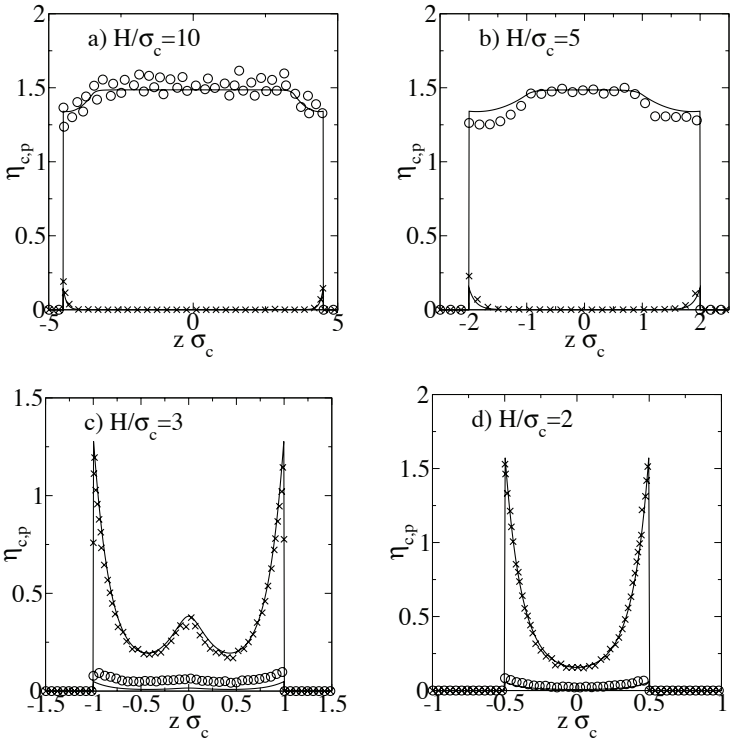

Figure 4.9: Density profiles of the AOV model with $q = 1$ between parallel hard walls with varying separation distance: a) H/σ_c=10, b) H_c/σ_c= 5, c) H_c/σ_c=3, and d) H_c/σ_c=2 at statepoint A of the phase diagram of Fig. 4.4(b), i.e., for polymer reservoir packing fraction $\eta_p^r = 1.49$ and colloid fugacity $\ln(z_c\sigma_c^3) = 4.6$. Shown are results from simulations for the density profiles of the colloids (crosses) and polymers (circles), and results from DFT (full lines).

4.5.4 Two dimensional limit

We next analyze the dimensional crossover from three to two spatial dimensions by reducing the distance of the hard walls towards $H/\sigma_c \to 1$. The two-dimensional system encountered for $H/\sigma_c = 1$ is identical to a two-dimensional mixture of colloidal hard discs and ideal polymer discs. Two-dimensional mixtures were previously studied with both theory [95, 96], and experiments [97]. For H very close to σ_p the polymer reservoir packing fraction scales as

$$\eta_p^r \sim \frac{\pi}{6}\frac{N_p\sigma_p^3}{A(H-\sigma_p)}. \tag{4.31}$$

We eliminate the divergence using scaled variables for the polymer reservoir packing fraction $\eta_p^r(H-\sigma_p)/H$ and for the colloidal fugacity $z_c(H-\sigma_c)/H$. Effectively, we map the

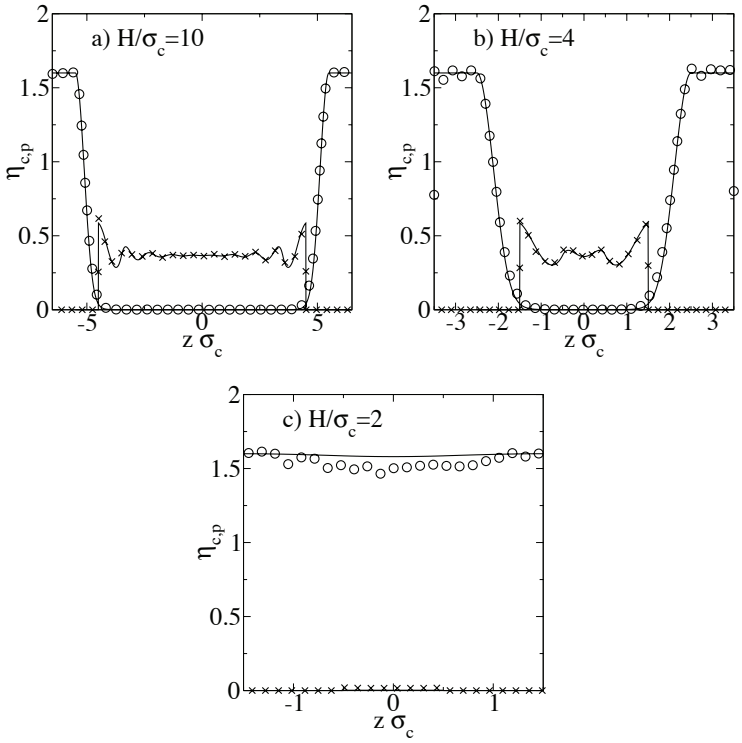

Figure 4.10: Density profiles of the AOV model between two parallel semi-permeable walls with varying separation distance: a) H_c/σ_c=10, b) H_c/σ_c=4, and c) H_c/σ_c=2 at statepoint B of the phase diagram of Fig. 4.6(b), i.e., for polymer reservoir packing fraction $\eta_p^r = 1.60$ and colloid fugacity $\ln(z_c\sigma_c^3) = 7.3$. Shown are results from simulations for the density profiles of the colloids (crosses) and polymers (circles), and results from DFT (full lines).

three-dimensional system with packing fractions $\eta_i = \pi\sigma_i^3 N_i/(6AH)$ to the two-dimensional system with packing fractions $\eta_i = \pi\sigma_i^2 N_i/(4A)$, where $i = c, p$.

In Fig. 4.11(a) we plot the phase diagrams in the scaled $\eta_p^r - \eta_c$ representation and we observe that the binodals for $H/\sigma_c = 1.01$ and $H/\sigma_c = 1.005$ are superimposed, demonstrating that this is a reliable estimate for the binodals of the 2-dimensional system. The comparison with a two-dimensional DFT [96] equivalent to a two-dimensional free volume theory [95] indicates poorer agreement as in the three-dimensional case. The discrepancy in the critical polymer reservoir packing fraction is substantial. We also find that in this representation the binodals of the three-dimensional system of the slits collapse over the bulk binodal, indicating a scaling of the critical value of η_p^r as $(\eta_p^r)_{crit} \sim 1/(H-\sigma_p)$. In Fig. 4.11(b) we see that the collapse of the binodals onto a master curve in the scaled η_p^r– scaled z_c representation is not as good as in the other representation, moreover the sequence of binodals is inverted, indicating that the critical value of the colloid fugacity

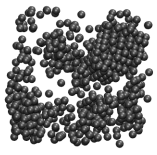

scales differently.

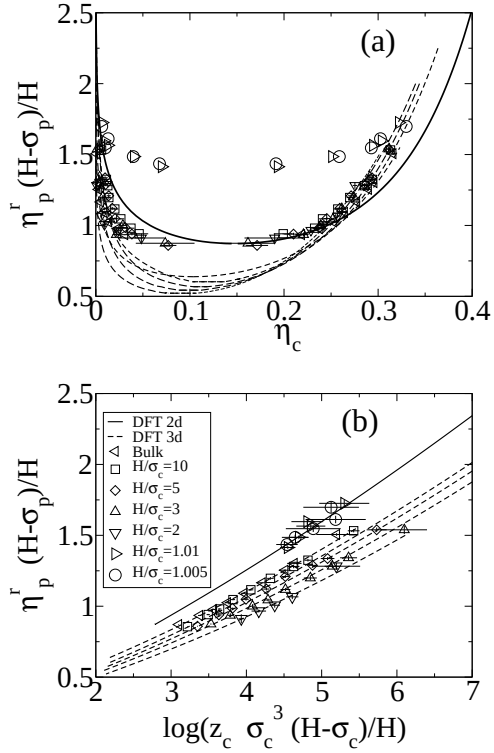

Figure 4.11: Phase diagrams showing the binodals for the AOV model between parallel hard walls with separation distance $H/\sigma_c = \infty, 10, 5, 3, 2, 1.01$, and 1.005. Shown are results from simulation (symbols), from three-dimensional DFT (dashed curves), and from DFT for the AOV model in two dimensions (full lines). (a) The gas-liquid binodal as a function of the scaled variable $\eta_p^r(H-\sigma_p)/H$ and η_c; (b) The gas-liquid binodals as a function of the scaled variables $z_c\sigma_c^3(H-\sigma_c)/H$ and $\eta_p^r(H-\sigma_p)/H$.

4.5.5 Kelvin equation

In this section, we compare the simulation results with the predictions of the Kelvin equations that we derived in section 4.4. First, we address the relationship of the parameter h, we used in the Kelvin equations, to our model parameter H. There are two, a priori equivalent, choices that we investigate, namely $h = H$, and $h = H - \sigma_c$. Second, the Kelvin equations need, as an input, the difference of the gas and liquid tensions at the wall interface. Since this data are not readily available we will assume, in the case of capillary condensation, the relation $\gamma_{wg} - \gamma_{wl} = \gamma_{lg}$, strictly valid only in the complete wetting regime, to hold at all state points considered. Likewise, for the capillary evaporation case, we assume

$\gamma_{wl} - \gamma_{wg} = \gamma_{lg}$, valid in the complete drying regime to hold at all state points. For the liquid-gas interfacial γ_{lg} tension we use DFT data from Ref. [98].

Figs. 4.12(a) and 4.12(c) display the simulation results for the hard wall slit together with the predictions of the Kelvin equations (4.18), (4.22), and (4.27) for $h = H - \sigma_{\mathrm{c}}$, and $h = H$ respectively. The Kelvin equation (4.18), derived from the path with constant polymer chemical potential, is superimposed at all separation distances with the Kelvin equation (4.22) derived using the constant pressure path. This is consistent with the observation of Aarts and Lekkerker [83]. Now we can offer an alternative explanation. As shown in Fig 4.2, for the capillary condensation case the bulk in the gas phase (polymer rich phase), and the path with constant polymer chemical potential is almost equivalent to the constant pressure path. In other words, the bulk reference point for Eq. (4.18) and Eq. (4.22) is very similar in the case of capillary condensation. The Kelvin equation (4.27) derived using a normal path, predict a smaller shift with respect to Eq. (4.22). To estimate the error introduced by the complete wetting approximation ($\gamma_{wg} - \gamma_{wl} = \gamma_{lg}$), we show a few points (filled diamonds) predicted by Eq. (4.22) using the actual difference in wall tensions, as published in our previous work [99].

The Figs. 4.12(b) and 4.12(d) display the simulation results for the semi-permeable wall slit together with the predictions of the Kelvin equations (4.18), (4.23), and (4.27) for $h = H - \sigma_{\mathrm{c}}$, and $h = H$ respectively. The prediction of Eq. (4.23) and (4.27) are superimposed at all separation distances considered. This is surprising since they are derived from very different "paths", as shown in Fig. 4.2.

We can conclude that the Kelvin equation we derived using a novel approach, gives predictions that are consistent, and in quantitative agreement with the prediction of the classic equation. In addition our equation is the same for capillary condensation and evaporation, and the choice of reference state, which is different for both phenomena, is avoided. As the Kelvin equation is based on macroscopic arguments, it is surprising that we find reasonable quantitative agreement for nearly two-dimensional systems. The shift of the critical polymer fugacity towards higher values upon increasing confinement, as found in simulations, is not reproduced, because the Kelvin equation is entirely based on properties of the (semi)infinite system. Finally, the two choices of h we presented give essentially the same results for wall separations H/σ_c as small as 4.

4.6 Conclusions

In conclusion, we have studied the effect of strong confinement provided by two parallel walls on the phase behavior and structure of model mixtures of colloids and polymers of size ratio $q = 1$. The densities of the gas and liquid phases at coexistence, as well as the chemical potentials were computed by GEMC simulations and DFT. Two different models of confining walls were investigated: i) Hard walls, impenetrable to both colloids and polymers, as a model for glass walls in contact with colloid-polymer mixtures were found to stabilize the liquid phase for statepoints that lie in the gas part of the bulk phase diagram; this effect is referred to as capillary condensation. ii) Semi-permeable walls, impenetrable to colloids but penetrable to polymers, could be experimentally realized using polymer coated substrates [84]. If the coating density is not too high the polymer brushes can act

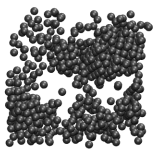

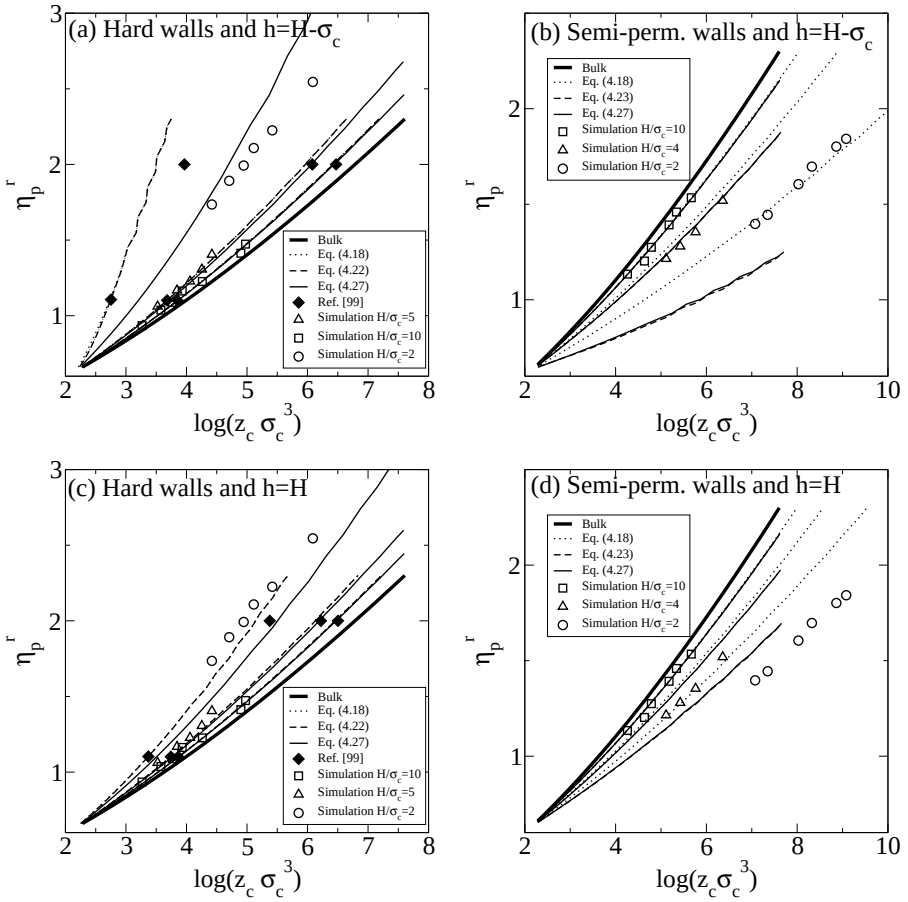

Figure 4.12: Phase diagram of colloid-polymer mixtures in the colloidal chemical potential $\log(z_c\sigma_c^3)$ and the polymer reservoir packing fraction η_p^r representation. (a) Results for slits with hard walls, and $h = H - \sigma_c$. (b) Results for the slit with semi-permeable walls , and $h = H - \sigma_c$. (c) Results for the slits with hard walls, and $h = H$. (d) Results for the slit with semi-permeable walls, and $h = H$. In (a) and (c) the simulation results (symbols) are compared with the prediction of the Kelvin equations (4.18), (4.22), and (4.27) assuming complete wetting ($\gamma_{wg} - \gamma_{wl} = \gamma_{lg}$). The filled diamonds are results from Eq. (4.22) using the difference in wall tensions $\gamma_{wg} - \gamma_{wl}$ taken from Ref. [99]. In (b) and (d) the simulation results (symbols) are compared with the prediction of the Kelvin equations (4.18), (4.23), and (4.27) assuming complete drying ($\gamma_{wl} - \gamma_{wg} = \gamma_{lg}$). For the liquid-gas interfacial tension γ_{lg} we used DFT data from Ref. [98]. Few lines are superimposed, see text for the explanation.

as impenetrable for colloids while being penetrable for polymers. We find that the effect of semi-permeable walls is to stabilize the gas phase for statepoints in the liquid part of the bulk phase diagram; this effect is referred to as capillary evaporation. Both capillary evaporation and condensation are consistently predicted by GEMC simulations and DFT. The differences between simulations and DFT in the vicinity of the critical point are confirmed for bulk mixtures and were found to be larger for the confined mixtures. The differences reach a maximum in the limit of two-dimensional colloid-polymer mixtures.

We have studied the structure of the mixture between parallel walls by measuring the density profiles in the direction normal to the confining walls. For the liquid phase, rich in colloids and poor in polymers, we found layering of colloids with an oscillation period roughly equal to the diameter of the particles for all wall separations and statepoints considered. In the case of semi-permeable walls, the structure, i.e. the layering of colloids and the adsorption or desorption of gas layers at the semi-permeable walls, depends strongly on the statepoint and on the lengthscale of the confinement. For the gas phase, rich in polymers and poor in colloids, we found flat polymer profiles with moderate desorption of polymers from the hard walls. We found that density oscillations for colloids and polymers are correlated in the liquid phase and anti-correlated in the gas phase. This can be understood by the following argument. In the liquid phase the fraction of polymers is small and a polymer is always surrounded by other colloids to which it interacts with an hard-core potential. Clearly the polymer structure must be similar to that of the colloids. In the gas phase the fraction of polymers is large with respect to the colloids and the entropy is increased by segregation of colloids, so if a region is locally denser in polymer than the average polymer density, it will be more dilute in colloids. The comparison between simulation and DFT is overall good, with small differences in the vicinity of the critical point. Our findings of capillary condensation for hard walls and capillary evaporation for semi-permeable walls are consistent with the experimental findings by Aarts and Lekkerker [83] and Wijting *et al.* [13, 84]. In the next chapter we will study confinement effects by including excluded volume interactions between polymer coils. The model has given accurate results for the bulk phase diagram [100].

Acknowledgements: The DFT calculations presented in this chapter were carried out by Matthias Schmidt.

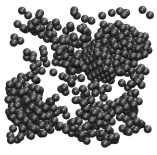

5

Effect of excluded volume interactions on colloid-polymer mixtures confined between two parallel planar walls

We study bulk and confined colloid-polymer mixtures using grand canonical Monte Carlo simulations. Colloidal particles are treated as hard spheres, while the polymer chains are described as soft repulsive spheres. The polymer-polymer, colloid-polymer, and wall-polymer interactions are described by the potential derived by Bolhuis and Louis [101]. We compared our results with those of the Asakura-Oosawa-Vrij model, that treats the polymers as ideal particles. We find that the number of polymers needed to drive the demixing transition is larger for the interacting polymers, and the gas-liquid interfacial tension is smaller. When the system is confined between two hard parallel plates, we find capillary condensation. This effect is slightly suppressed by the interactions between the polymers.

5.1 Introduction

In the previous chapter we studied confined colloid-polymer mixtures modelled by the Asakura-Oosawa-Vrij model (AOV) [27, 28, 38]. The polymer chains were described as spheres with a radius equal to the radius of gyration of the polymer coils. Polymer spheres could freely overlap, while they were excluded by a centre of mass distance from the colloidal particles. The AOV model has been extensively studied in the past years, and it was shown that it can qualitatively describe the bulk [30, 32, 35, 43, 46, 96, 102–104], and interfacial phase behaviour [13, 14, 81, 82, 84, 105], of mixtures of colloids and polymers. A similar level of agreement was found for the interfacial tension of the gas-liquid [104, 106, 107] and wall-fluid interfaces [47, 49, 107], and for the phase behaviour of confined systems [83, 97, 99, 108–110].

The quantitative discrepancies between experimental results and the AOV model results can arise from a number of reasons, like non-ideal solvent conditions [111], colloid-induced polymer compression [112], effect of charges on the colloidal surface [113, 114],

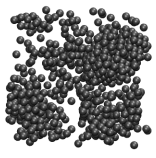

or polymer excluded volume interactions. In this chapter, we will concentrate on the latter aspect. The simplest inclusion of polymer interactions was done by introducing a step function interaction between the polymers, i.e. an energy penalty for the overlaps of two polymers. The step potential was used to study the bulk phase diagram and interfacial tension [115, 116], the contact angle of the colloidal liquid-gas interface and a hard wall [49], as well as the stability of the floating liquid phase in sedimenting colloid-polymer mixtures [117]. This approach gives results that are in better agreement with experiments when compared against the AOV model, but the height of the step potential must be introduced as an additional free parameter. Furthermore, we expect the polymer-colloid interaction to be modified as well when considering excluded volume interactions between polymers.

Aarts et al. [118] extended the free volume theory [30] to include polymer interactions, while a well studied theoretical approach for the gas-liquid interfacial tension is the square gradient approximation [98, 118–120].

Another approach is to describe the polymers as soft spheres [101], with effective interactions derived from inversion of the centre of mass (CM) correlation functions in lattice Self-Avoiding-Walk (SAW) polymer simulations. This approach generates soft density-dependent potentials for the polymer-polymer and colloid-polymer interactions, that give accurate results in the determination of the bulk phase behaviour [100]. In a similar approach, proposed by Jusufi et al. [121], the effective potentials are derived from off-lattice molecular dynamics simulations of SAW polymer chains. These potentials were used to study the bulk phase behaviour [122, 123], and the gas-liquid interfacial tension [124] of colloid-polymer mixtures, leading to results in quantitative agreement with experiments.

A one component perturbative DFT that uses the potentials of Bolhuis and Louis [101] was developed by Moncho-Jorda et al. [125] to study confined systems and the gas-liquid tension. In this chapter, we study the influence of excluded volume interactions on the phase behaviour of confined colloid-polymer mixtures with Monte Carlo computer simulations. We treat the interactions according to those derived by Bolhuis and Louis [101].

5.2 Model

The colloids are treated as hard spheres and the corresponding pair potential reads

$$v_{\rm cc}(R_{ij}) = \begin{cases} \infty & \text{if } R_{ij} < \sigma_{\rm c} \\ 0 & \text{otherwise,} \end{cases} \tag{5.1}$$

where $R_{ij} = |\vec{R}_i - \vec{R}_j|$ is the distance between two colloidal particles, with $\vec{R}_i$ the position of the centre of mass of colloid i. For the polymer-polymer, colloid-polymer, and wall-polymer potentials we utilise the expressions obtained by Bolhuis and Louis [101] fitting their simulation results of a system of SAW polymer chains on a lattice, with 500 segments, and radius of gyration R_g=16.83 lattice units at zero concentration. We introduce the overlap concentration ρ^* defined by the equation $4/3\pi\rho^* R_g^3 = 1$, and the polymer reservoir packing fraction $\eta_p^r = \rho_{\rm p}^r/\rho^*$, with $\rho_{\rm p}^r$ the density in the reservoir of pure polymers in osmotic equilibrium with the two-component system of interest.

The density dependent polymer-polymer effective interaction, originally derived by Bolhuis and Louis [101], reads

$$v_{\rm pp}(r_{ij},\eta_p^r) = \sum_{k=1}^{3} a_k(\eta_p^r)\exp(-r_{ij}/b_k(\eta_p^r))^2, \tag{5.2}$$

where $r_{ij} = |\vec{r}_i - \vec{r}_j|$ is the distance between two polymers, with $\vec{r}_i$ the position of the centre of mass of polymer i. The density-dependent parameters are linear in the density $a_k = a_k^0 + a_k^1\eta_p^r$, and $b_k = b_k^0 + b_k^1\eta_p^r$. All coefficients, with the exclusions of b_k^3, are given in table 5.1. The coefficients b_k^3 are fixed by imposing the equality of the mean field equation of state

$$P/\rho_p = 1 + \rho_p\hat{v}(0;\rho_p)/2\,, \tag{5.3}$$

for the fitted potentials and the SAW simulations, where the function

$$\hat{v}(0;\rho_p) = 4\pi\int r^2 v_{\rm pp}(r,\rho_p)dr \tag{5.4}$$

is the $k=0$ component of the Fourier transform of the polymer-polymer pair potential. In practice, the condition is satisfied by imposing the equality between

$$\hat{v}(0;\eta_p^r) = \pi^{3/2}\sum_{i=1}^{3} a_i(\eta_p^r)b_i(\eta_p^r)^3\,, \tag{5.5}$$

derived from Eq. (5.2) and

$$\hat{v}(0;\eta_p^r) = 4\pi(1.2902 + 0.28132\eta_p^r + 0.13676(\eta_p^r)^2 - 0.040892(\eta_p^r)^3) \tag{5.6}$$

derived using Eq. (5.3) and the potentials obtained from the inversion of the radial distribution function from SAW simulations.

Table 5.1: Coefficients for the density dependent parameters of the polymer-polymer interaction potential $v_{\rm pp}$ defined in Eq. (5.2).

	k=1	k=2	k=3
a_k^0	1.47409	-0.23210	0.63897
a_k^1	-0.07689	0.03132	0.24193
b_k^0	0.98137	0.42123	/
b_k^1	-0.05681	-0.02628	/

The concentration dependent colloid-polymer potential reads [100]

$$v_{\rm cp}(|\vec{R}_i - \vec{r}_j|,\eta_p^r) = \sum_{k=1}^{2} c_k(\eta_p^r)\exp(-((|\vec{R}_i - \vec{r}_j| - e_k(\eta_p^r))/d_k(\eta_p^r))^2), \tag{5.7}$$

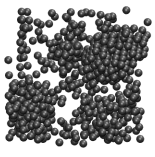

Table 5.2: Coefficients for the density dependent parameters of the colloid-polymer interaction potential v_{cp} defined in of Eq. (5.7).

	k=1	k=2
c_k^0	5.5610	1.8477
c_k^1	-0.8042	1.4759
d_k^0	0.7751	1.2720
d_k^1	-0.1151	0.1052
e_k^0	0.4082	0.0
e_k^1	0.1410	0.0

where $|\vec{R}_i - \vec{r}_j|$ is the distance between colloid i and polymer j. The density-dependent parameters are linear in density, i.e., $c_k = c_k^0 + c_k^1 \eta_p^r$, $d_k = d_k^0 + d_k^1 \eta_p^r$, and $e_k = e_k^0 + e_k^1 \eta_p^r$. The coefficients are given in table 5.2.

The interaction between colloidal particles and the hard wall is hard-sphere-like, that is the colloidal particles can not penetrate the walls. The interaction between polymers and the hard wall [101] reads

$$v_{\mathrm{wp}}(z, \eta_p^r) = f_0(\eta_p^r) \exp[f_1(\eta_p^r) z + f_2(\eta_p^r) z^2 + f_3(\eta_p^r) z^3], \tag{5.8}$$

where z is the distance between the wall and the centre of mass of the polymer. The parameters have a quadratic density dependence $f_k(\eta_p^r) = f_k^0 + f_k^1 \eta_p^r + f_k^2 (\eta_p^r)^2$, with k=0, 1, 2, 3. The coefficients are given in table 5.3.

Table 5.3: Coefficients for the density dependent parameters of the wall-polymer interaction potential v_{wp} defined in Eq. (5.8).

	k=0	k=1	k=2	k=3
f_k^0	62.7242	-6.4093	2.5081	-0.6904
f_k^1	56.4595	-3.8880	5.1562	-1.5519
f_k^2	-29.9283	2.0442	-2.1336	0.5973

5.3 Method

We carried out Monte Carlo simulations in the grand canonical ensemble, i.e. with fixed volume, temperature, and chemical potentials μ_c and μ_p, of colloids and polymers, respectively. We determine the potentials given in the previous section, at the polymer reser-

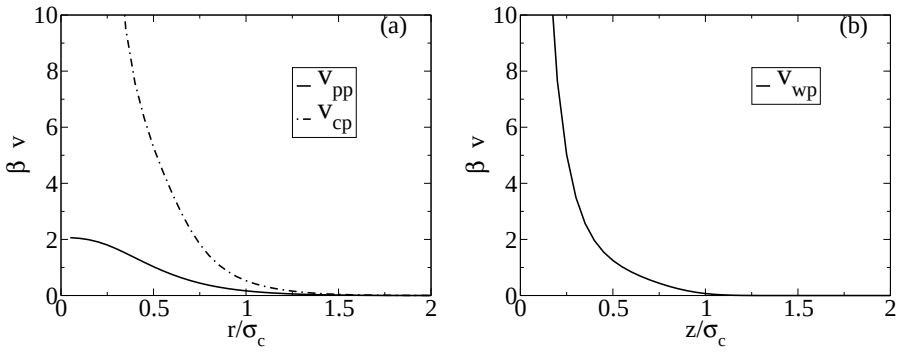

Figure 5.1: Interaction potentials for the polymer density $\eta_p^r = 1.02995$. (a) Pair potential between polymers $\beta v_{\rm pp}$ (full line), and between polymers and colloids $\beta v_{\rm cp}$ (dashed line). (b) Wall-polymer potential $\beta v_{\rm wp}$ as a function of the distance z/σ_c of the polymer centre of mass from the wall.

voir packing fraction $\eta_p^r(\mu_p)$ calculated by inversion of the equation of state

$$\mu_p / k_B T = \log(\rho_p^r R_g^3) + 0.04658 + 11.05\rho_p^r R_g^3 + 35.48(\rho_p^r R_g^3)^2 - 15.71(\rho_p^r R_g^3)^3 \,. \tag{5.9}$$

This chemical potential was derived by integration of the Gibbs-Duhem equation with the pressure given by Eq. (5.3) and Eq. (5.6).

To study phase coexistence, we sample the probability $P(N_c)|_{z_c,\eta_p^r}$ of observing N_c colloids in a volume V at fixed colloid fugacity z_c and fixed polymer reservoir packing fraction η_p^r, using the successive umbrella sampling [126]. We use the histogram reweighting technique to obtain the probability distribution for any z_c' once $P(N_c)|_{z_c,\eta_p^r}$ is known for a given z_c:

$$\ln P(N_c)|_{z_c',\eta_p^r} = \ln P(N_c)|_{z_c,\eta_p^r} + \ln\left(\frac{z_c'}{z_c}\right) N_c. \tag{5.10}$$

At phase coexistence, the distribution function $P(N_c)$ becomes bimodal with two separate peaks of equal area for the colloidal liquid and gas phases. We determine which z_c' satisfies the equal area rule

$$\int_0^{\langle N_c\rangle} P(N_c)|_{z_c',\eta_p^r} dN_c = \int_{\langle N_c\rangle}^{\infty} P(N_c)|_{z_c',\eta_p^r} dN_c, \tag{5.11}$$

with the average number of colloids

$$\langle N_c\rangle = \int_0^{\infty} N_c P(N_c)|_{z_c,\eta_p^r} dN_c, \tag{5.12}$$

using the histogram reweighting equation (5.10). The simulations are carried out in a cubic box $V = L \times L \times H$, and the sampling of the probability ratio $P(N)/P(N+1)$ is done, in each window, until the difference between two successive samplings of the probability ratio is smaller than 5×10^{-4}.

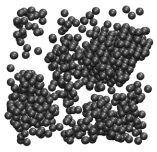

The liquid-gas interfacial tension $\gamma_{\rm lg}$ is obtained from $P(N_c)|_{z_c',\eta_p^r}$ at coexistence [127]

$$\gamma_{\rm lg} = \frac{1}{2L^2}\left[\ln\left(\frac{P(N^g_{c,\max})+P(N^l_{c,\max})}{2}\right) - \ln(P(N_{c,\min}))\right] \tag{5.13}$$

where $P(N^g_{c,\max})$ and $P(N^l_{c,\max})$ are the maxima of the gas and liquid peaks, respectively, and $P(N_{c,\min})$ is the minimum between the two peaks.

5.4 Results

In Sec. 5.2 we explained the straightforward, but nontrivial procedure for generating the interaction potentials. It is therefore important to check the internal consistency of our calculations. Fig. 5.2 shows the predictions of the equation of state (5.9) plotted against simulations results of a grand canonical simulation of pure polymers interacting with the potential (5.2). In the range of chemical potentials that are relevant for the gas-liquid separation the simulation results are consistent with the equation of state.

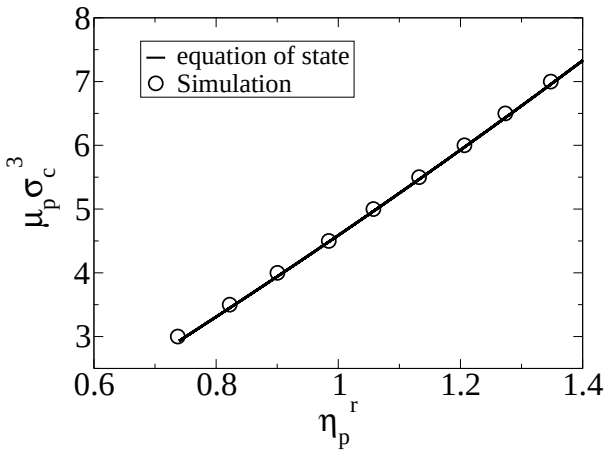

Figure 5.2: The chemical potential $\mu_p\sigma_c^3$ as a function of the polymer packing fraction η_p^r, in a system of pure polymers. The equation of state (5.9) (line) is compared with the results of a grand canonical simulation (circles) of pure polymers interacting with the potential (5.2).

5.4.1 Bulk phase behaviour and gas-liquid interfacial tension

In Fig. 5.3 we present the bulk phase diagram obtained from the grand canonical simulations with successive umbrella sampling and histogram reweighting. In particular, Fig. 5.3(a) shows the phase diagram in the polymer packing fraction η_p, colloid packing fraction η_c representation. These results are consistent with the findings of Bolhuis et al. [100]. The free volume theory [128] extended to include excluded volume polymer in-

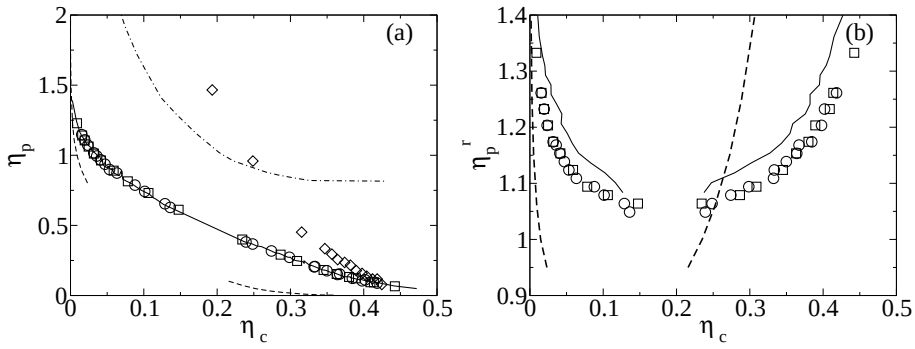

Figure 5.3: Phase diagram of bulk colloid-polymer mixtures with size ratio q=1.05 for volume V=516 σ_c^3 (circles) and V=2304 σ_c^3 (squares). Also shown are the binodals of the AOV model with size ratio $q = 1.0$ (dashed lines). (a) Polymer packing fraction η_p, colloid packing fraction η_c representation. Shown are also the results of Bolhuis et al. [100] (continuous line), the results of the free volume theory with polymer interactions [118] (dashed line) and the experimental results of de Hoog and Lekkerkerker [102] (diamonds). (b) Polymer reservoir packing fraction η_p^r, colloid packing fraction η_c representation.

teractions [118], overestimates the simulation results by almost a factor two. This result may be explained by the renormalisation group theory expression used to evaluate the polymer interactions, that underestimates the correlation length of the polymers. Also shown are the experimental results of de Hoog and Lekkerkerker [102]. The experimental polymer concentration is much larger than our simulation results. This discrepancy can be explained by considering the measurements of Wijting et al. [129] on depletion forces in the same colloid-polymer system used in Ref. [102]. They found that the depletion forces are much smaller then expected, probably due to adsorption of the polymers on the colloidal surface.

Fig. 5.3(b) shows the phase diagram in the polymer reservoir packing fraction η_p^r, colloids packing fraction η_c representation. The discrepancy between our results and those of Bolhuis et al. [100] are due to a slightly different equation of state used for the conversion of the chemical potential μ_p at coexistence to the polymer packing fraction in the reservoir η_p^r. The binodal has a critical point at lower η_p^r, and the density difference between the gas and liquid phases increases for increasing η_p^r. This phase diagram is equivalent to the temperature-density phase diagram of a simple fluid, with the polymer reservoir packing fraction playing the role of an inverse temperature.

In Fig. 5.4, we present the simulation results of the dimensionless interfacial tension $\beta\gamma_{gl}\sigma_c^2$ for the gas-liquid interface, as a function of the difference in packing fraction between the gas and the liquid phases. The excluded volume interactions lead to a lower interfacial tension than in the case of ideal polymers. The comparison between our results and the experiments of Aarts et al. [82] is quantitatively better than the results of the AOV model, although de Hoog and Lekkerkerker [102] show that it is difficult to obtain accurate interfacial tension measurements. In addition, we compare our results with the predictions of the extended free volume theory plus a square gradient approximation to

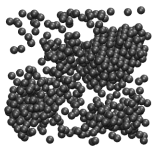

evaluate the tension [120], and the density functional theory (DFT) of Moncho-Jorda et al. [125]. The DFT uses the same interaction potentials used in this work but restricted to the effective pairwise potential between colloids. The predictions of the two theories are very close to each other and to the simulation results.

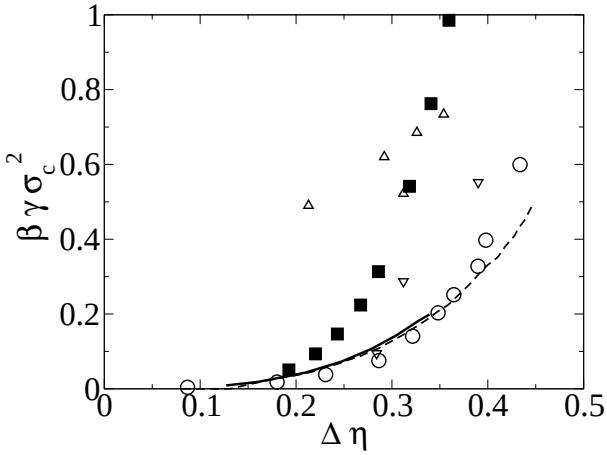

Figure 5.4: Dimensionless interfacial tension $\beta\gamma\sigma_c^2$ between the gas and liquid phases, as a function of the difference $\Delta\eta = \eta_l - \eta_g$ between the packing fractions of the coexisting liquid (η_l) and gas (η_g) phases. Results for the interacting polymers with size ratio $q = 1.05$ (circles) are compared with the results for the AOV model with size ratio $q = 1.0$ (square). Triangles denote experimental results of de Hoog and Lekkerkerker [102] (triangles up) and Aarts et al. [82] (triangles down). The thick continuous line indicates the predictions of the DFT of Moncho-Jorda et al. [125], while the dashed lines are the predictions of the square gradient approximation theory of Aarts et al. [120].

5.4.2 Confined system: Capillary condensation

Fig. 5.5 shows the phase diagram of colloid-polymer mixtures confined between hard walls with separation distance $H/\sigma_c = \infty$, 16, 8, 4, 2. In particular, Fig. 5.5(a) shows the phase diagram of colloid-polymer mixtures in the polymer reservoir packing fraction η_p, colloid packing fraction η_c representation, and Fig. 5.5(b) shows the phase diagram of colloid-polymer mixtures in the polymer packing fraction η_p^r, colloid packing fraction η_c representation. The critical points of the confined systems shift towards higher η_p^r for decreasing wall separation. The density difference for the AOV model at fixed η_p^r, decreases for decreasing separation distance.

Fig. 5.6 displays the phase diagram in the polymer chemical potential μ_p, colloid chemical potential μ_c representation. The binodals collapse to a single line because of the condition of gas-liquid coexistence. Regions above the binodal are gas like, while regions below the binodal are liquid like. We find a shift of the binodals towards higher polymer chemical potential and smaller colloid chemical potential indicating the occurrence of capillary condensation.

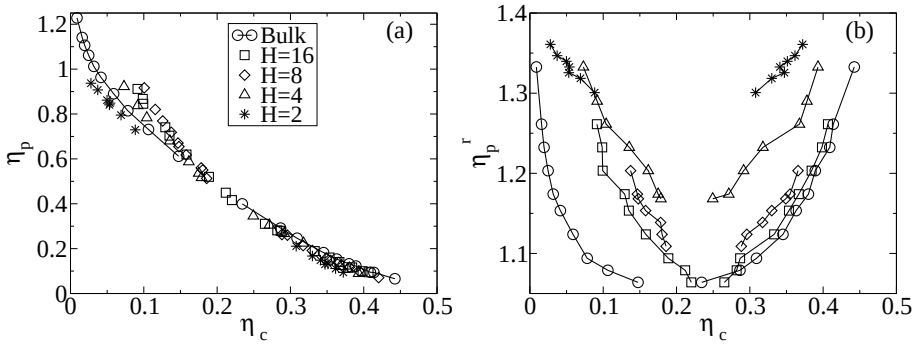

Figure 5.5: Phase diagram of colloid-polymer mixtures confined between model walls with distance $H/\sigma_c = \infty$, 16, 8, 4, 2. (a) Polymer packing fraction η_p, colloid packing fraction η_c representation. (b) Polymer reservoir packing fraction η_p^r, colloid packing fraction η_c representation.

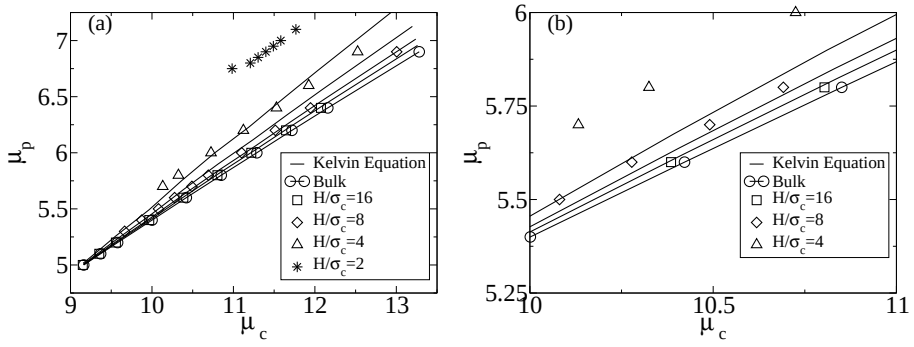

Figure 5.6: Phase diagram of colloid-polymer mixtures confined between model walls with distance $H/\sigma_c = \infty$, 16, 8, 4, 2, in the polymer chemical potential μ_p, colloid chemical potential μ_c representation. In (b) we show a blow-up of the phase diagram. For clarity the results of $H/\sigma_c = 2$ are not shown.

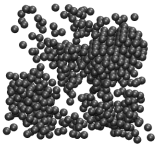

Also shown in Fig. 5.6 are the predictions of the Kelvin equation [109]

$$\begin{aligned}\mu_c &= \mu_c^{\text{Bulk}} + \frac{2}{h}(\gamma_{wl} - \gamma_{wg})\frac{\rho_c^l - \rho_c^g}{(\rho_c^l - \rho_c^g)^2 + (\rho_p^l - \rho_p^g)^2}, \\ \mu_p &= \mu_p^{\text{Bulk}} + \frac{2}{h}(\gamma_{wl} - \gamma_{wg})\frac{\rho_p^l - \rho_p^g}{(\rho_c^l - \rho_c^g)^2 + (\rho_p^l - \rho_p^l)^2},\end{aligned} \tag{5.14}$$

The predictions of the Kelvin equation are in good agreement with the simulation results for H/σ_c =16, and 8, but underestimates the shift for H/σ_c =4, and 2.

5.5 Conclusions

In this chapter, we have investigated bulk and confined colloid-polymer mixtures, using Monte Carlo computer simulations. Colloids behaved as hard spheres, while polymers were described as soft repulsive spheres. Colloid-polymer, polymer-polymer, and wall-polymer density dependent interactions were described by the potentials derived by Bolhuis and Louis [101]. We find a bulk phase behaviour consistent with the findings of Bolhuis et al. [100]. The behaviour is also similar to the prediction of the AOV model, but the binodal line lies at higher polymer packing fractions, i.e., the number of polymers needed for the demixing transition is larger. These results are in agreement with the findings of other authors [100, 119, 120, 124]. The comparison of our phase diagram with experiments [102] is found to be poor for the size ratio $q = 1.05$ considered here. This is surprising, since the same interaction potentials provided good agreement with experiments at a smaller size ratio [101]. In fact, this discrepancy can be explained by considering the results of Wijting et al. [129] on depletion potential measurements on the same colloid-polymer mixtures used in the phase behaviour experiments. These measurements concluded that the depletion attraction was smaller than expected, probably due to polymer adsorption on the surface of the colloids.

On the other hand, better agreement is found for the gas-liquid interfacial tension when compared to the experiments of Aarts et al. [82] for the same system. Our results show that the gas-liquid interfacial tension is smaller for the interacting polymers than for the AOV model. This is in agreement with the works of other authors, on colloid-polymer mixtures with interacting polymers [116, 120, 124, 125]. Both the square gradient approximation and the DFT provide a good description of the simulation results.

In addition, we studied the phase behaviour of the mixture confined between parallel walls with separation distance H/σ_c =16, 8, 4, and 2. We find that the hard walls induce capillary condensation, and that the theoretical predictions of the Kelvin equation are in reasonable agreement with the simulation results for H/σ_c =16 and 8, but underestimate the binodal shifts for H/σ_c =4 and 2.

Acknowledgements: I want to thank Arturo Moncho Jordá and Dirk G. A. L. Aarts for sending me their interfacial tension data.

6

Phase behaviour of model charged colloid-polymer mixtures

We study the stability of mixtures of highly screened repulsive charged spheres and non-adsorbing ideal polymer chains with Monte Carlo computer simulations and free volume theory. The effective interaction between charged colloids is described by a screened-Coulomb pair potential. In the free volume theory the ideal polymer chains are treated as spheres that are excluded from the colloids by a hard-core interaction, whereas the interaction between two ideal chains is set to zero. In computer simulations we use the two-body (Asakura-Oosawa pair potential) approximation to the effective one-component Hamiltonian of the charged colloids. Both our results obtained from simulations and from free volume theory show similar trends. We find that the screened-Coulomb repulsion counteracts the effect of the *effective* polymer-mediated attraction. For mixtures of small polymers and relatively large charged colloidal spheres, the fluid-crystal transition shifts to significantly larger polymer concentrations with increasing range of the screened-Coulomb repulsion. For relatively large polymers, the effect of the screened-Coulomb repulsion is weaker. The resulting fluid-fluid binodal is only slightly shifted towards larger polymer concentrations upon increasing the range of the screened-Coulomb repulsion. Our results show that the miscibility of dispersions containing charged colloids and neutral non-adsorbing polymers increases upon increasing the range of the screened-Coulomb repulsion, or upon lowering the salt concentration, especially when the polymers are small compared to the colloids.

6.1 Introduction

Many stable dispersions containing spherical colloids consist of particles that can be characterised by a pair potential containing an additional soft repulsive tail. An example is a stable dispersion of charged colloids in an aqueous salt solution for which the interactions are described by the Derjaguin-Landau [23], and Verwey-Overbeek [24] (DLVO) theory that we introduced in section 1.3.2. This theory predicts that the effective pair interaction be-

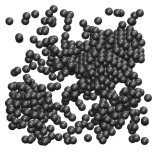

tween charged colloids consists of a hard-core repulsion due to the finite size of the colloids and a screened-Coulomb (Yukawa) repulsion with the screening length given by the Debye length κ^{-1} of the solvent. The screening length κ^{-1} defines the thickness of the double layer of opposite charge surrounding each colloid. The range κ^{-1} of the screened-Coulomb repulsion is a function of the salt concentration of the solvent, the dielectric constant and the temperature. Adjusting the salt concentration may influence the stability of a dispersion of charged colloids mixed with a neutral depletion agent in a common aqueous salt solution [36, 130–132]. Hebert [130] studied the precipitation of the charged, rod-like tobacco mosaic virus (TMV) by adding the neutral polymer polyethylene glycol (PEG). At similar PEG concentrations, precipitation of TMV was enhanced by adding salt. Patel and Russel [133] studied the phase behaviour of mixtures of charged polystyrene latex colloids and dextran as (neutral) polymer chains and reported a significant shift towards higher polymer concentrations of the fluid-fluid binodal curve as compared to predictions for neutral polymer chains mixed with hard spheres. Grinberg and Tolstoguzov [36] presented generalised phase diagrams of proteins mixed with neutral non-adsorbing polysaccharides in aqueous salt solutions. The miscibility was shown to increase when the ionic strength of the solvent was lowered. Finet and Tardieu [131] studied the stability of solutions of the lens protein crystalline. Adding an excess of salt to this system does not destabilise the protein dispersion. Hence, it follows that the effective attractions between the proteins are absent or are very weak in the case of screened charges. Adding PEG however induces significant attractions [131], and results in a shift of the liquid-liquid phase transition to higher temperatures [134]. Adding excess salt and PEG induces instant phase separation [131]. A similar synergetic effect of salt and PEG was found in aqueous solutions of (spherical) brome mosaic virus particles [132]. In conclusion, the trend found in experimental studies on mixtures of charged 'colloids' plus neutral polymers is that the miscibility is increased upon decreasing the salt concentration, i.e., increasing the range of the screened-Coulomb repulsion.

In the light of these findings it is important to study theoretically mixtures of colloids with a screened-Coulomb repulsion mixed with neutral polymer chains and to investigate whether the trend found in many experimental studies is recovered. The amount of theoretical work performed so far is rather limited. Ferreira *et al.* [135] made a polymer reference interaction site model (PRISM) analysis up to the level of the pair interaction and computed gas-liquid spinodal curves from the effective colloid-colloid structure factor. Denton and Schmidt [113] proposed a simple theory yielding the gas-liquid binodal curve. The fluid-solid coexistence curves were not considered and none of these theories were tested against computer simulations. Here we study the effect of a screened-Coulomb interaction on the total effective colloid-colloid interaction and on the resulting gas-liquid and fluid-solid phase transitions in a charged colloid dispersion with added non-adsorbing polymers. We demonstrate the fluid-solid coexistence is especially sensitive to the screened-Coulomb repulsion.

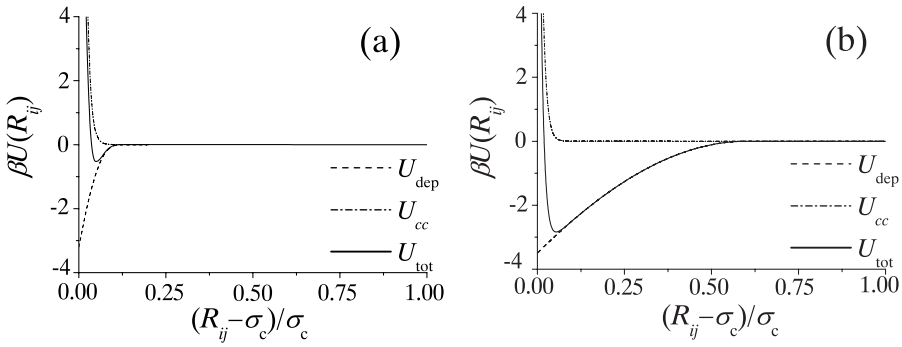

Figure 6.1: Pair interaction between two colloidal spheres with hard-core diameter σ_c interacting with a Yukawa pair potential $U_{\rm cc}$ (equation 6.1) and an effective depletion interaction $U_{\rm dep}$ (equation 6.5) due to the presence of non-adsorbing polymer coils with an effective diameter σ_p. The total effective interaction $U_{\rm tot}$ (equation 6.4) is denoted by the full curve. The Yukawa repulsion is characterised by $\beta\epsilon = 20$ and $\kappa\sigma_c = 100$. The depletion interactions are: (a) for a size ratio $q = \sigma_p/\sigma_c = 0.1$ and polymer reservoir packing fraction ϕ_p^r=0.2, (b) $q = 0.6$ and ϕ_p^r=1.

6.2 The model

We consider a suspension of charged colloidal spheres immersed together with non-adsorbing polymer in a common solvent. The effective pair interaction between the charged colloidal spheres with hard-core diameter σ_c, reads

$$U_{\rm cc}(R_{ij}) = \begin{cases} \infty & \text{for} \quad R_{ij} < \sigma_c \\ \epsilon\left(\frac{\exp(-\kappa\sigma_c(R_{ij}/\sigma_c-1))}{R_{ij}/\sigma_c}\right) & \text{otherwise} \end{cases}, \tag{6.1}$$

where $R_{ij} = |\mathbf{R}_i - \mathbf{R}_j|$ and $\mathbf{R}_i$ are the positions of the centres of the colloids. The range of the repulsive tail is set by the inverse Debye screening length $\kappa\sigma_c = \sqrt{8\pi\lambda_B\sigma_c^2\rho_s^r}$, which is related to the salt concentration ρ_s^r in the reservoir, and to the Bjerrum length $\lambda_B = e^2/\epsilon_s k_B T$ with k_B Boltzmann's constant, T the temperature, and ϵ_s the dielectric constant of the solvent. The strength of the repulsion of the repulsive Yukawa interaction is determined by the parameter $\epsilon = (Z/(1+\kappa\sigma_c/2))^2\lambda_B/\sigma_c$. In figure 6.1 an example of a typical Yukawa repulsion is given by the dot-dashed curves for $\beta\epsilon = 20$ and $\kappa\sigma_c = 100$. Here $\beta = 1/k_B T$.

Different procedures [136–140] exist that give the same functional form of the effective potential (6.1), but with a density dependent $\tilde{\kappa}\sigma_c = \sqrt{(4\pi\lambda_B\sigma_c^2(Z\rho_c + 2\rho_s))}$, where ρ_c and ρ_s are, respectively, the densities of colloidal particles and added salt ion pairs, in the system. The density ρ_s depends on the colloidal density and is smaller then the reservoir density due to salt exclusion or Donnan equilibrium [141–143]. For typical values of the parameters used in this work, $\beta\epsilon = 20$ and $\kappa\sigma_c = 50$, the effective $\tilde{\kappa}$ differ from the reservoir $\kappa\sigma_c = \sqrt{8\pi\lambda_B\sigma_c^2\rho_s^r}$ by less than 1% for a colloid density near close-packing $\rho_s = 1.4\sigma_c^{-3}$ when one applies Donnan equilibrium. Hence salt partitioning is hardly perceptible for the salt conditions considered here.

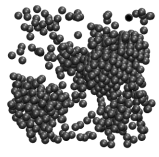

The polymers are described by the AOV model [28, 38, 39] framework, described in section 1.3.3. The colloid-polymer potential U_{cp}, and the polymer-polymer potential U_{pp} reads

$$U_{cp}(\mathbf{R}_i - \mathbf{r}_j) = \begin{cases} \infty & \text{for} \quad |\mathbf{R}_i - \mathbf{r}_j| < (\sigma_c + \sigma_p)/2 \\ 0 & \text{otherwise} \end{cases} \tag{6.2}$$

$$U_{pp}(r_{ij}) = 0\,, \tag{6.3}$$

where $\mathbf{R}_i$ and $\mathbf{r}_j$ are the positions of the centres of the colloids and the polymer coils, respectively, and $r_{ij} = |\mathbf{r}_i - \mathbf{r}_j|$. The full AOV model is recovered by setting ϵ to zero in the effective potential (6.1).

Monte-Carlo simulations are carried out with the Hamiltonian

$$U_{\rm tot}(R_{ij}) = U_{\rm cc}(R_{ij}) + U_{\rm dep}(R_{ij}). \tag{6.4}$$

where the depletion potential $U_{\rm dep}$, is the effective Hamiltonian derived for the AOV model in Sec. 1.3.3, and truncated at the pairwise term. It reads

$$\begin{aligned} \beta U_{\rm dep}(R_{ij},\mu_p) &= -\frac{\pi\sigma_p^3\rho_p^r}{6}\frac{(1+q)^3}{q^3}\left[1 - \frac{3R_{ij}}{2(1+q)\sigma_c} + \frac{R_{ij}^3}{2(1+q)^3\sigma_c^3}\right] \\ &\qquad \text{for} \quad \sigma_c < R_{ij} < \sigma_c + \sigma_p \\ &= 0 \qquad \text{for} \quad R_{ij} > \sigma_c + \sigma_p \end{aligned} \tag{6.5}$$

where we define the size ratio $q = \sigma_p/\sigma_c$. This Asakura-Oosawa pair potential describes an effective attraction whose depth increases linearly with the polymer density in the corresponding reservoir ρ_p^r. For convenience, we define the relative polymer concentration $\phi_p^r \equiv \pi\sigma_p^3\rho_p^r/6$. Hence, $\phi_p^r = 1$ defines the overlap concentration of the polymer solution. The range of the potential is given by σ_p. The depletion interaction $U_{\rm dep}(R_{ij})$ is plotted as the dashed curves for $q = 0.1$ and ϕ_p^r=0.2 in figure 6.1(a), for $q = 0.6$ and $\phi_p^r = 1$ in figure 6.1(b). By adjusting q and ϕ_p^r one can manipulate the range and strength of the depletion interaction. We chose ϕ_p^r such that $\beta U_{\rm dep}(\sigma_c) = -3.5$ for every value of q.

Examples of $U_{\rm tot}(R_{ij})$ are plotted in figure 6.1 as the full curves, which are the sums of equations (6.1) and (6.5), denoted by the dot-dashed and dashed lines, respectively. For $q = 0.1$ (figure 6.1(a)) there is a significant effect of the repulsive tail on the effective interaction as compared to the pure depletion contribution $U_{\rm dep}(R_{ij})$. There is, however, still some attraction in the $U_{\rm tot}(R_{ij})$ curve between the charged repulsive spheres though it is significantly reduced as compared to the pure $U_{\rm dep}(R_{ij})$ result. In figures 6.1(b) the main part of the pair interaction curve $U_{\rm tot}(R_{ij})$ is identical to the pure depletion part $U_{\rm dep}(R_{ij})$ for $q = 0.6$ and $q = 1$. Only the attraction at short interparticle distances is affected.

6.3 Simulation details

This section describes the technical details of the simulations. We consider the total effective one-component Hamiltonian of the colloids at fixed polymer fugacity z_p

$$H(z_p) = H_{\rm cc} + H_{\rm dep}(z_p) \tag{6.6}$$

where the Hamiltonian $H_{\rm cc}$ consists of a sum of colloid-colloid pair potentials $U_{\rm cc}$, which can be split into a sum of hard-sphere potentials $U_{\rm HS}$ and a sum of repulsive Yukawa potentials:

$$H_{\rm cc} = \sum_{i<j}^{N_c} U_{\rm cc}(R_{ij}) = \sum_{i<j}^{N_c} U_{\rm HS}(R_{ij}) + \sum_{i<j}^{N_c} U_{\rm Yuk}(R_{ij}) \tag{6.7}$$

with

$$U_{\rm Yuk}(R_{ij}) = \epsilon \frac{\exp(\kappa\sigma_c(R_{ij}/\sigma_c - 1))}{R_{ij}/\sigma_c} \qquad \text{for} \qquad R_{ij} > \sigma_c \tag{6.8}$$

and $H_{\rm dep}$ a sum of depletion potentials $U_{\rm dep}$ (6.5):

$$H_{\rm dep}(z_p) = \sum_{i<j}^{N_c} U_{\rm dep}(R_{ij}; z_p). \tag{6.9}$$

The equation of state for charged hard spheres was obtained with MC simulations in the constant pressure ensemble. We carried out simulations in a cubic box with $N = 350$ colloids for the fluid phase, and $N = 576$ colloids for the solid f.c.c. phase. We used 250000 sweeps per particle for equilibration, and the average density was sampled for 250000 sweeps per particle.

To determine the free energy we carried out thermodynamic integration. The contribution of the Yukawa potential, for the fluid phase, was calculated by introducing the auxiliary Hamiltonian

$$H_{cc,\lambda}^{fluid} = \sum_{i<j}^{N_c} U_{\rm HS}(R_{ij}) + \lambda \sum_{i<j}^{N_c} U_{\rm Yuk}(R_{ij}) \tag{6.10}$$

where $0 \le \lambda \le 1$ is a dimensionless coupling parameter: at $\lambda = 0$ the auxiliary Hamiltonian is that of a pure system of N_c hard spheres, while at $\lambda = 1$ it is the Hamiltonian of N_c charged spheres. The free energy is determined by applying the standard λ-integration technique [18]

$$f_c(N_c, V) = f_{\rm HS}(N_c, V, \lambda = 0) + \frac{v_c}{V} \int_0^1 d\lambda \left\langle \sum_{i<j}^{N_c} \beta U_{\rm Yuk}(R_{ij}) \right\rangle_{N_c,V,\lambda}. \tag{6.11}$$

The angular brackets denote a canonical average over a system of N_c particles interacting with the Hamiltonian $H_{cc,\lambda}^{fluid}$, while $f_{\rm HS}(N_c, V, \lambda = 0)$ is the free energy of a system of hard spheres, for which we use the Carnahan-Starling expression [144]. We start the canonical simulations from a random, non-overlapping configuration, and use 15000 MC sweeps per particle for equilibration and typically 15000 production moves for each value of the coupling parameter λ. In principle, the free energy of the solid phase can be computed with the same technique using the Hall expression for the free energy of the hard-sphere crystal [145]. However the latter is only properly defined for packing fractions larger than the value at hard sphere freezing $\eta_c = 0.545$, while charged spheres can yield crystal phases

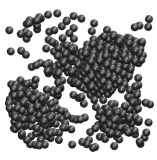

at lower packing fractions. A different technique is used for the solid phase by introducing the auxiliary Hamiltonian

$$H_{cc,\lambda}^{solid} = \sum_{i<j}^{N_c} U_{\rm cc}(R_{ij}) + \lambda k_B T \sum_{i=1}^{N_c} (\mathbf{r}_i - \mathbf{r}_{o,i})^2/\sigma_c^2 , \tag{6.12}$$

where $\mathbf{r}_{o,i}$ denote the ideal lattice position of particle i in a fcc crystal. The free energy is computed by applying the integration technique introduced by Frenkel and co-workers [146, 147]

$$\begin{aligned} f_c(N_c,V) &= f_{ein}^{CM}(N_c,V,\lambda=\lambda_{max}) + f_{corr}(N_c,V) \\ &\quad - \frac{\nu_c}{V}\int_0^{\lambda_{max}} d\lambda \left\langle \sum_{i=1}^{N_c} (\mathbf{r}_i - \mathbf{r}_{o,i})^2/\sigma_c^2 \right\rangle_\lambda^{CM} , \end{aligned} \tag{6.13}$$

where the angular brackets denote a canonical average of the mean square displacement of N_c particles interacting with the Hamiltonian $H_{cc,\lambda}^{solid}$, while the superscript CM denotes that it is calculated for a crystal with fixed centre of mass. The parameter λ_{max} is chosen such that for $\lambda = \lambda_{max}$ the system behaves like a non-interacting Einstein crystal with fixed centre of mass and Madelung energy $U_{\rm Yuk}(\mathbf{r}_0^{N_c})$, i.e., the potential energy of a crystal with all particles at their ideal lattice positions. Typical values for λ_{max} range from 1000 to 100000 for high densities. The free energy of a non-interacting Einstein crystal with fixed centre of mass reads

$$\begin{aligned} f_{ein}^{CM}(N_c,V,\lambda=\lambda_{max}) &= \frac{\nu_c}{V}\beta U_{\rm Yuk}(\mathbf{r}_0^{N_c}) - \frac{3(N_c-1)\nu_c}{2V}\ln\left[\frac{\pi}{\lambda_{max}}\right] \\ &\quad + \frac{(N_c-1)\nu_c}{V}\ln\left[\frac{\Lambda_c^3}{\sigma_c^3}\right] \end{aligned} \tag{6.14}$$

The correction term f_{corr} arises when the constraint on the centre of masses is released, i.e., the Helmholtz free energy difference between the unconstrained and constrained crystal:

$$f_{corr}(N_c,V) = \frac{\nu_c}{V}\ln\left[\frac{\Lambda^3}{VN_c^{1/2}}\right]. \tag{6.15}$$

The equilibration is done for 15000 MC steps per particle, and the averages are taken for 15000 MC steps per particle.

To determine the free energy contribution of the AOV depletion potential $f_{\rm dep}$ we employ a second thermodynamic integration for the solid and fluid phase:

$$\begin{aligned} f_{\rm dep} &= f(N_c,V,\rho_p^r) - f(N_c,V,\rho_p^r=0) \\ &= \int_0^{\rho_p^r} d\rho_p^{r\prime} \left(\frac{\partial f(N_c,V,\rho_p^{r\prime})}{\partial \rho_p^{r\prime}}\right)_{N_c,V,\rho_p^{r\prime}} \end{aligned} \tag{6.16}$$

The system at $\rho_p^r = 0$ is a system of colloids interacting with pair potentials $U_{\rm cc}$. The integral is calculated by dividing the interval $[0,\rho_p^r]$ in 20 to 30 equally spaced intervals. We

used 10000 MC steps per particles for equilibration, while averages were taken for 20000 MC steps per particle. In addition we used the integrand to determine the number density of ideal polymer in the system using the thermodynamic relation

$$\left(\frac{\partial f(N_c,V,\rho_p^r)}{\partial \rho_p^r}\right) = \left(\frac{\partial f(N_c,V,z_p)}{\partial z_p}\right) = -v_c \frac{\langle \rho_p \rangle_{\rho_p^r}}{\rho_p^r} \tag{6.17}$$

6.4 Theory

6.4.1 Charged colloids

In this section we propose a simple description for charged colloidal suspensions. We consider the screened-Coulomb repulsion as a perturbation of the hard-sphere interaction which is only valid for highly screened colloidal suspensions. The effective volume fraction η_e of the charged repulsive spheres is approximated as

$$\eta_e = \left(\frac{\sigma_e}{\sigma_c}\right)^3 \eta_c = m\,\eta_c \tag{6.18}$$

where $\eta_c \equiv \pi\sigma_c^3\rho_c/6$ with ρ_c the colloid number density and σ_e the effective diameter of the spheres defined by the Barker-Henderson relation [148]:

$$\sigma_e = \sigma_c + \int_{\sigma_c}^{\infty} \left(1 - \exp[-\beta U_{\rm cc}(r)]\right) dr \tag{6.19}$$

which is a useful way to generalise pair potentials of various shapes [149], in particular, perturbations from hard-sphere behaviour (see [44]). Instead of $U_{\rm cc}$ defined in equation (6.1) one may use any other form for a (soft) repulsion. The physical effects are contained in the value for m. Since we assume that a collection of charged spheres behave similarly as a collection of pure hard spheres plus a small perturbation, we may use the Carnahan-Starling (CS) expression [144] for the Helmholtz free energy to describe the thermodynamic properties of the fluid of charged spheres:

$$m f_c^{\rm fluid}(\eta_c,T) = \eta_e \ln\eta_e + \frac{4\eta_e^2 - 3\eta_e^3}{(1-\eta_e)^2} - \eta_e + \eta_e \ln\frac{6\Lambda_c^3}{\pi\sigma_c^3} \tag{6.20}$$

where Λ_c is the thermal wavelength of the colloids and where the hard-sphere volume fraction η_c in the classical CS expression is replaced by the effective volume fraction η_e, defined in equations (6.18) and (6.19). In equation (6.20) we use (as in [118]) the normalised Helmholtz free energy f_c, defined as $\beta F_c v_c/V$, where F_c is the Helmholtz free energy, and $v_c = \pi\sigma_c^3/6$ is the volume of a single colloid.

The equation of state of the face-centred-cubic (fcc) crystal phase of pure hard spheres is described accurately by the expression proposed by Hall [145]. Likewise, the equation of state for the fcc crystal phase of the charged spheres reads

$$m f_c^{\rm crystal}(\eta_c,T) = \eta_e\left(2.1306 + 3\ln\left[\frac{\eta_e}{1-\eta_e/\eta_{cp}}\right]\right) + \eta_e \ln\frac{6\Lambda_c^3}{\pi\sigma_c^3} \tag{6.21}$$

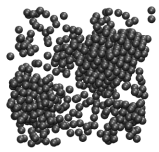

containing the volume fraction at close packing $\eta_{cp} = \pi\sqrt{2}/6 \approx 0.74$. The quantity 2.1306 is derived from computer simulation results [146]. The osmotic pressure $\beta\Pi_c v_c = \eta_c \partial f_c/\partial\eta_c - f_c$ reads

$$m\beta\Pi_c^{\text{fluid}} v_c(\eta_c, T) = \frac{\eta_e + \eta_e^2 + \eta_e^3 - \eta_e^4}{(1-\eta_e)^3}, \tag{6.22}$$

for the fluid phase and

$$m\beta\Pi_c^{\text{crystal}} v_c(\eta_c, T) = \frac{3\eta_e}{1 - \eta_e/\eta_{cp}}, \tag{6.23}$$

for the f.c.c. crystal.

6.4.2 Charged colloid-polymer mixtures

A simple approach that successfully describes the stability of polymer-colloid mixtures is the semi-grand canonical free volume or osmotic equilibrium theory [30, 128]. In this approach, a macroscopic volume V at temperature T is considered, that contains N_c colloids together with polymer chains and solvent, which are in osmotic equilibrium with a reservoir containing only solvent and polymer chains. Hence, the system is considered in the (N_c, V, z_p, T) ensemble, in which the number of colloids N_c and the fugacity of the polymer chains z_p are fixed. Consider the thermodynamic identity [43]:

$$\beta F(N_c, V, z_p) = \beta F(N_c, V, z_p = 0) + \int_0^{z_p} dz_p' \left(\frac{\partial \beta F(N_c, V, z_p')}{\partial z_p'}\right)_{z_p'} \tag{6.24}$$

where we dropped the temperature dependence for convenience. The integrand can now be Taylor expanded about $z_p = 0$:

$$\begin{aligned} \beta F(N_c, V, z_p) &= \beta F(N_c, V, z_p = 0) + z_p \left(\frac{\partial \beta F(N_c, V, z_p)}{\partial z_p}\right)_{z_p=0} \\ &\quad + \mathcal{O}(z_p^2) + \cdots \end{aligned} \tag{6.25}$$

where the partial derivative can be written as

$$\left(\frac{\partial \beta F(N_c, V, z_p)}{\partial z_p}\right)_{z_p=0} = \left(\frac{\partial F}{\partial \mu_p}\right)_{z_p=0} \frac{\partial \beta \mu_p}{\partial z_p} = -\frac{\langle N_p \rangle_{z_p=0}}{z_p}. \tag{6.26}$$

The number of polymer chains $\langle N_p \rangle_{z_p=0}$ can be related by definition to the averaged free volume that is available for the polymer chains $\langle V_{free} \rangle_{z_p=0}$ in the system of spheres that is undistorted by the addition of polymers:

$$\langle N_p \rangle_{z_p=0} \equiv \rho_p^r \langle V_{free} \rangle_{z_p=0}. \tag{6.27}$$

where ρ_p^r is the density of ideal polymer in the corresponding reservoir. Defining the free volume fraction $\alpha \equiv \langle V_{free} \rangle_{z_p=0}/V$, we can rewrite equation (6.24) as:

$$\beta F(N_c, V, z_p) = \beta F(N_c, V, z_p = 0) - \alpha \rho_p^r V + \mathcal{O}(z_p^2) + \cdots \tag{6.28}$$

The free volume theory [30] retains only the first-order term, neglecting terms $\mathcal{O}(z_p^2)$ and higher. With this assumption the normalised thermodynamic potential $f \equiv \beta F v_c / V$ can be written as the sum of two terms:

$$f(N_c, V, z_p) = f_c(N_c, V) - \alpha \phi_p^r q^{-3} \tag{6.29}$$

The first term in equation (6.29) is the normalised Helmholtz free energy $f(N_c, V, z_p = 0) \equiv f_c(N_c, V)$ of a 'pure colloid' fluid at a given η_c, while the second can be interpreted as a perturbation due to the presence of polymer chains. Note that equation (6.24)-(6.29) holds for any colloid-polymer and polymer-polymer interactions within the assumptions that are made.

All information about the interactions between colloid and polymer is contained in the variation of α with η_c. For our model and the AOV model, the free volume fraction α can be calculated accurately from scaled particle theory [30, 150] (see *e.g.* Meijer and Frenkel [35] for a comparison with computer simulation results). Once the coexisting colloid volume fractions are determined for given ϕ_p^r, the actual relative polymer concentrations can be obtained in the coexisting phases from $\phi_p \equiv \alpha \phi_p^r$. The expression for the free volume fraction of polymer chains in a mixture of charged spheres using scaled particle theory reads

$$\alpha = (1 - \eta_c) \exp(-A\gamma - B\gamma^2 - C\zeta - 3C\zeta^2 - 3C\zeta^3), \tag{6.30}$$

where $\gamma = \eta_c/(1-\eta_c)$, $\zeta = \eta_e/(1-\eta_e)$, $A = 3q + 3q^2$, $B = 9q^2/2$, and $C = q^3$. An explicit derivation is given in section 6.4.3. Equation (6.30) reduces to the classical expression of Lekkerkerker *et al.* [30] for the case $\eta_e = \eta_c$ ($m = 1$). The free volume available for the polymer chains is thus mainly a function of the pure hard-sphere volume fraction η_c; it is only affected by the screened-Coulomb repulsion at high colloid volume fractions or large polymer chains. In the derivation of equation (6.30) an equal statistical weight is assigned to all (non-overlapping) hard-sphere configurations, whereas the weight should involve the polymer-mediated effective interactions and the screened-Coulomb interactions. We expect our results to be accurate only if $\sigma_e/\sigma_c - 1 << q$. If the depletion layers become small compared to $\sigma_e - \sigma_c$ one expects hardly any overlap of depletion layers.

6.4.3 Free volume fraction in a charged sphere dispersion

We consider the free volume fraction α that is available for ideal polymer chains in a sea of charged spheres with diameter σ_c. As the centre-of-mass of the polymer chains is excluded from the centre-of-mass of the charged colloids by a distance $(\sigma_c + \sigma_p)/2$ and the polymer interactions are ideal, α is just the free volume fraction for a single hard-sphere with diameter σ_p in a sea of charged spheres. This free volume fraction α can be determined from the chemical potential of the polymer chains. The chemical potential for inserting a polymer in a sea of charged spheres consists of an ideal gas term and a work term W.

$$\beta\mu_p = \ln \rho_p \Lambda_p^3 + W \tag{6.31}$$

Following Widom's particle insertion method [151], the required work to insert a polymer W is equal to $\beta W = -\ln \alpha$. The work W can be determined from scaled particle theory,

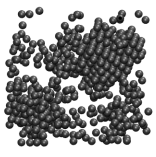

that considers two limits. In this theory, the size of the particle is scaled with a parameter x. In the limit $x \ll 1$, the polymer coils reduce to points, and hence the volume fraction available to the polymer is simply unity minus the sum of the overall hard-sphere volumes plus the depletion layers around them:

$$\alpha(x \ll 1) = 1 - \frac{\pi}{6}\rho_c\left(\sigma_c + x\sigma_p\right)^3 \tag{6.32}$$

where $\rho_c = N_c/V$ is the number of colloidal spheres per volume (related to η_c via $\eta_c = \pi\rho_c\sigma_c^3/6$). Hence, it follows

$$\beta W(x \ll 1) = -\ln\left[1 - \frac{\pi}{6}\rho_c\left(\sigma_c + x\sigma_p\right)^3\right] \tag{6.33}$$

On the other hand, if $x \gg 1$, the work required to insert a polymer coil in a sea of charged spheres, is approximately the work to create a hole with the size of the polymer coil, which is equal to the volume of the polymer coil times the osmotic pressure Π_c of the dispersion of charged colloids:

$$W(x \gg 1) = \frac{\pi}{6}x^3\sigma_p^3\Pi_c. \tag{6.34}$$

In scaled particle theory, $W(x \ll 1)$ is expanded about $x = 0$ up to order x^2 and $W(x \gg 1)$ is added as the x^3 term.

$$W(x) = W(x=0) + x\left(\frac{\partial W}{\partial x}\right)_{x=0} + \frac{1}{2}x^2\left(\frac{\partial^2 W}{\partial x^2}\right)_{x=0} + \frac{\pi}{6}x^3\sigma_p^3\Pi_c \tag{6.35}$$

Scaling the polymer coils to the desired size by $x = 1$, yields

$$\begin{aligned}\beta W(x=1) \quad &= \quad -\ln\left[1-\eta_c\right] + 3q\gamma + \frac{1}{2}\left(6q^2\gamma + 9q^2\gamma^2\right) \\ &\quad + \frac{\pi}{6}\sigma_p^3\beta\Pi_c\end{aligned} \tag{6.36}$$

where $\gamma = \eta_c/(1-\eta_c)$. Hence α follows straightforwardly from $W \equiv W(x=1)$. For pure hard spheres one usually takes the Percus-Yevick result for the pressure Π_{HS} from the virial route (see [44]) since it is consistent with SPT

$$\frac{\beta\Pi_{\mathrm{HS}}}{\rho_c} = \frac{1 + \eta_c + \eta_c^2}{\left(1-\eta_c\right)^3} = \frac{1}{1-\eta_c} + \frac{3\eta_c}{\left(1-\eta_c\right)^2} + \frac{3\eta_c^2}{\left(1-\eta_c\right)^3} \tag{6.37}$$

Inserting this expression for Π_{HS} into equation 6.36 for Π_c yields

$$\beta w = -\ln\left[1-\eta_c\right] + (A + C)\gamma + (B + 3C)\gamma^2 + 3C\gamma^3 \tag{6.38}$$

where A, B, and C, are defined below equation 6.30. Hence, we arrive at the standard SPT result for the free volume fraction of ideal polymer in a sea of hard spheres [30]

$$\alpha = \left(1-\eta_c\right)\exp\left[-\left((A + C)\gamma + (B + 3C)\gamma^2 + 3C\gamma^3\right)\right] \tag{6.39}$$

In case of colloidal spheres interacting with a Yukawa pair potential, we rewrite equation (6.37) following the approach outlined in section 3 giving a pressure

$$\frac{\beta\Pi_{\rm Yuk}}{\rho_c} = \frac{1+\eta_e+\eta_e^2}{\left(1-\eta_e\right)^3} = \frac{1}{1-\eta_e} + \frac{3\eta_e}{\left(1-\eta_e\right)^2} + \frac{3\eta_e^2}{\left(1-\eta_e\right)^3} \tag{6.40}$$

where η_e is defined by equation (6.18). Using this expression for Π_c in equation 6.36 yields equation 6.30.

6.5 Results

6.5.1 Hard spheres

Let us first check the accuracy of equations (6.20) and (6.21) on the level of the resulting osmotic pressure Π_c. Results using equations (6.22) and (6.23) with $U_{\rm cc}(R_{ij})$ given by equation (6.1) are plotted in figure 6.2 (curves) and are compared with computer simulation data (symbols), for $\beta\epsilon = 20$ and $1/\kappa\sigma_c$ equals 0 (full curves, open circles), 0.01 (dotted curve, filled squares) and 0.02 (dashed curve, open triangles), corresponding to $m = 1$, 1.110 and 1.225, respectively. The results for pressures below $\beta\Pi_c v_c = 6.2$ correspond to the colloidal fluid phase, while the results for larger pressures correspond to the fcc crystal. Figure 6.2 shows that the pressure increases upon increasing the range of the soft repulsion. The simulation results are well described by equation (6.22) (see the results for

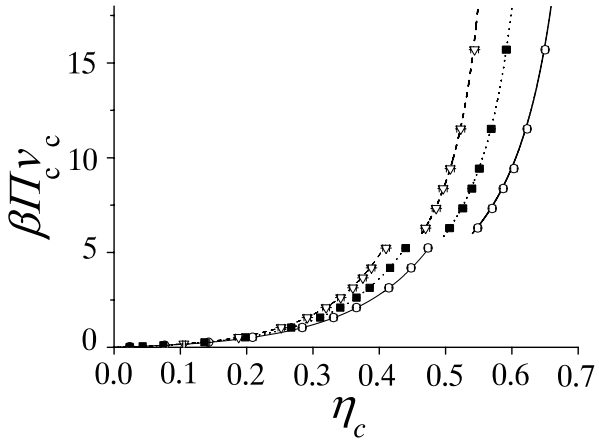

Figure 6.2: Pressure of a dispersion of charged colloidal spheres interacting with $U_{\rm cc}(R_{ij})$ (see equation (6.1)) for $\beta\epsilon = 20$ and $1/\kappa\sigma_c = 0$ (open circles, full curves), 0.01 (filled squares, dotted curves), and 0.02 (open triangles, dashed curves), corresponding to $m = 1, 1.110$, and 1.225, respectively, in equation (6.18). The symbols denote the simulation results, while the curves denote the theoretical predictions of equations (6.22) (lower set of pressures) and (6.23) (upper set).

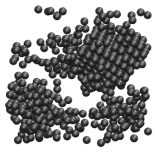

$\beta\Pi_c v_c < 6.2$.) for the fluid phase for $m = 1$, $m = 1.110$ and $m = 1.225$. In addition, the results for the solid phase using equation (6.23) ($\beta\Pi_c v_c > 6.2$) agree well with the simulations for $m = 1$, $m = 1.110$ and $m = 1.225$. Our results demonstrate that for sufficiently short-ranged soft repulsions, the screened-Coulomb interaction can be treated as a perturbation of the hard-sphere potential using the Barker-Henderson relation (6.19). The

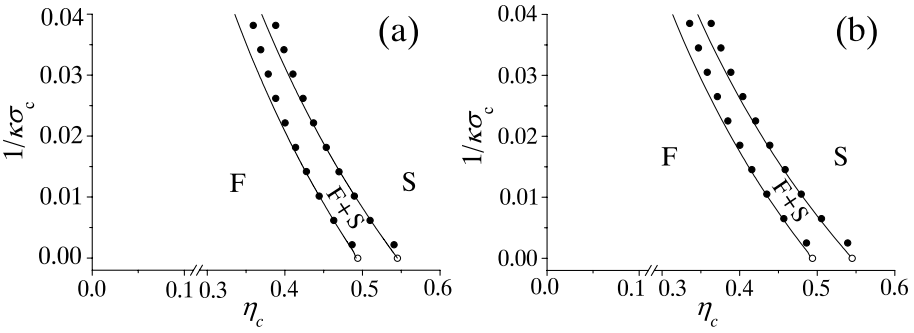

Figure 6.3: Fluid-solid (fcc) transition of charged colloidal spheres interacting with a hard-core repulsive Yukawa potential (6.1) with a) $\beta\epsilon = 20$ and b) $\beta\epsilon = 39$. Open symbols denote simulation results of pure hard spheres taken from Ref. [60]. Filled circles denote the simulation results of Hynninen and Dijkstra [26]. Full curves correspond to the theoretical predictions as described in section 6.4.

fluid-solid transition, first established for pure hard spheres by Alder and Wainwright [2] and Wood and Jacobson [152], can now be studied as a function of the softness of the repulsive tail. We determine the densities of the coexisting phases by equating the osmotic pressures and the chemical potentials $\beta\mu = \partial f_c/\partial\eta_c$ using equations (6.20) and (6.21). It becomes evident that the Ansatz of equations (6.18), (6.19), (6.20) and (6.21) is expected to be useful only for short-ranged soft repulsions, so for $\sigma_e \simeq \sigma_c$ or $1/\kappa\sigma_c \to 0$. In order to test whether this approach is valid for relatively short-ranged soft repulsions, we compare the predicted fluid-solid transitions with computer simulation data for small values of $1/\kappa\sigma_c$.

In figure 6.3, the fluid-solid binodals calculated for $1/\kappa\sigma_c < 0.04$ are plotted as the full curves. In figure 6.3(a), the $\beta\epsilon = 20$ case is considered. The dots are computer simulation results by Hynninen and Dijkstra [26]. Open symbols are the pure hard-sphere computer simulation results of Hoover and Ree [60]. For $1/\kappa\sigma_c < 0.02$ the agreement is excellent though for larger Debye lengths deviations are found. This deviation is not surprising since the simple theoretical method is based on a perturbation from the hard-sphere system and is, hence, expected to be only accurate for very small values of $1/\kappa\sigma_c$. Still, this simple theory for charged colloidal sphere dispersions suffices our purpose of studying the stability of charged colloid-polymer mixtures in the regime of $1/\kappa\sigma_c < 0.02$. To be more specific, this means that our Ansatz describes well the case of colloidal particles with a diameter of, say, $\sigma_c = 100$ nm with a Debye length smaller than about 2 nm or, equivalently, an ionic strength $> 0.02M$ (in the case of monovalent ions in water at room temperature). Actually, in nature, the ionic strength in aqueous salt concentrations is usually above $0.02M$, so for

large spheres we still capture the biologically relevant ionic strength regime. For globular proteins we can only compare with experimental data at significant salt concentrations but we can still make estimates of the main trends. In figure 6.3(b), we compare our theoretical results (full curves) with computer simulation data (crosses) for $\beta\epsilon = 39$. Again, our Ansatz is in fair agreement with the computer simulation results (data points) [26]. Hence we validated our approach to describe the fluid and fcc crystal equations of state and the fluid-solid transition of a charged sphere dispersion for $1/\kappa\sigma_c < 0.02$. This provides a base for studying the effect of adding non-adsorbing polymer to such a suspension.

6.5.2 Results for model charged colloid-polymer mixtures

We study the stability of a mixture of charged colloidal spheres and non-adsorbing polymer chains in a common (background) solvent. In figure 6.4 we compare the result of the free volume fraction α as a function of the colloid volume fraction η_c of equation (6.30) with Monte Carlo simulation results for $\langle\rho_p\rangle_{z_p}/\rho_p^r$ using equation (6.17) for $q = 0.1$. It is worth mentioning that α is evaluated in the pure charged-colloid system in the free volume theory, i.e., $z_p = 0$, while $\langle\rho_p\rangle_{z_p}/\rho_p^r$ from simulations do depend on z_p. In the simulations, however, we use z_p along the bulk binodals as shown in figure 6.1 (which will be discussed later). The theoretical curves in figure 6.4 show only a slight effect of the

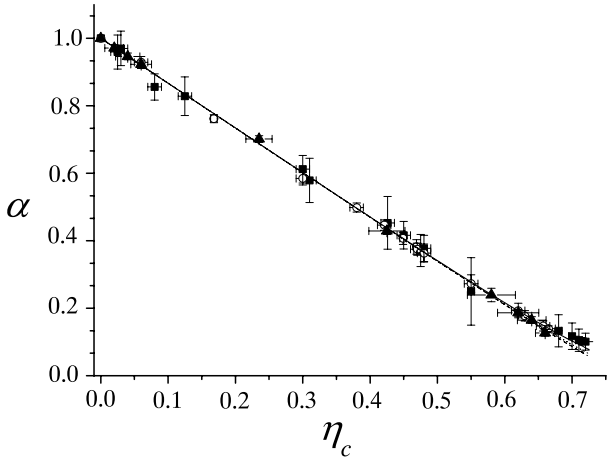

Figure 6.4: Free volume fraction $\alpha \equiv \langle V_{free}\rangle_{z_p=0}/V$ for a mixture of charged colloids and ideal polymer with size ratio $q = \sigma_p/\sigma_c = 0.1$ as a function of hard-core volume fraction η_c. The screened-Coulomb repulsion is characterised by $\beta\epsilon = 20$ and various values of $\kappa\sigma_c$. Full, dotted and dashed curves represent equation (6.30) for $\kappa\sigma_c = \infty$ ($m = 1$), 100 ($m = 1.110$) and 80 ($m = 1.138$), respectively. Note that the differences in the theoretical curves are only noticeable at high η_c.The symbols with errorbars denote the Monte Carlo simulation results for $\langle\rho_p\rangle_{z_p}/\rho_p^r$ using equation (6.17) for $\kappa\sigma_c = \infty$ (closed squares), $\kappa\sigma_c = 100$ (open circles) and $\kappa\sigma_c = 80$ (closed triangles), where we used z_p at bulk coexistence (see figure 6.6).

screened-Coulomb repulsion on α for $\eta_c > 0.4$. Within the statistical error bars, no signifi-

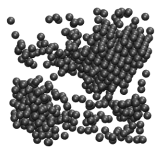

cant effect of the screened-Coulomb repulsion was detected in the simulations on the free volume fraction. Moreover, the z_p-dependence is hardly noticeable. We thus conclude that equation (6.30) is accurate for short-ranged screened-Coulomb repulsions for $q = 0.1$ or, equivalently, that the effect of the screened-Coulomb repulsion on α is negligible.

We can now analyse the effect of the screened-Coulomb repulsion on the phase behaviour. The osmotic pressures Π and colloid chemical potentials μ_c can be found by differentiation of the Helmholtz free energy (6.29). The colloid volume fractions in each of the coexisting phases, η_c^1 and η_c^2, are obtained by equating μ_c and Π at fixed polymer reservoir concentration ϕ_p^r. The Helmholtz free energy density (6.21) is used for the solid phase, while equation (6.20) is employed for the fluid.

In figure 6.5(a), we plot the phase diagram using the free volume theory (6.29) for a size ratio $q = 0.1$ and $(\kappa\sigma_c)^{-1} = 0.0$, 0.005, 0.01, and 0.0125 in the (η_c, ϕ_p^r) plane. For $(\kappa\sigma_c)^{-1} = 0$ and $\phi_p^r = 0$, we recover the well-known pure hard-sphere freezing transition at $\eta_c = 0.494$ and 0.545 [60]. In the case of charged spheres, the freezing transition at $\phi_p^r = 0$ shifts to lower colloid volume fractions η_c, which is in line with the results in figure 6.3, and is due to a larger effective volume of the charged spheres. Figure 6.5(a), shows clearly that the fluid-solid transition widens upon increasing the polymer concentration. More specifically, the broadening of the freezing transition shifts to higher ϕ_p^r with increasing range of the screened-Coulomb repulsion $(\kappa\sigma_c)^{-1}$. This can be explained as follows. Upon increasing the range of the screened-Coulomb repulsion, $\eta_e = m\eta_c$, and hence f_c, increases. At the same time the free volume fraction α is not affected significantly (see figure 6.4) upon adding a screened-Coulomb repulsion. So, in order to attain a similar effect on f (see Eq. (6.29)), a higher polymer concentration is required to broaden the freezing transition.

For larger values of q, say $q > 0.4$, a fluid-fluid coexistence becomes stable in the AOV model, which dominates the phase behaviour at colloid volume fractions $\eta_c < 0.49$. In analogy with figures 6.1(b) and 6.1(c) we choose $q = 0.6$ and 1 and study the effect of the repulsive screened-Coulomb interaction on the fluid-solid and fluid-fluid transition. In figures 6.5(b),(c), we plot the predictions from free volume theory in the (η_c, ϕ_p^r) representation for $q = 0.6$ and $q = 1.0$, respectively. We again find that the freezing transition at $\phi_p^r = 0$ shifts to lower colloid volume fractions η_c upon increasing $(\kappa\sigma_c)^{-1}$. In addition, figures 6.5(b),(c) show that the fluid-fluid demixing shifts to higher ϕ_p^r with increasing range of the screened-Coulomb repulsion $(\kappa\sigma_c)^{-1}$. Hence, the trends are similar as for $q = 0.1$. The screened-Coulomb repulsion reduces the depletion effect. The critical points are indicated as the filled circles in figure 6.5(b),(c), and they indicate that the critical colloid volume fraction η_c shifts to somewhat smaller values upon increasing the range of the soft repulsion.

To test the validity of the predictions from free volume theory, we compare our results with Monte Carlo simulations. We determine the phase diagram of the effective one-component system by calculating the dimensionless free energy density $f = \beta F v_c / V$ as a function of the colloid packing fraction η_c and the fugacity of the polymer chains z_p as explained in section 6.3. For non-interacting chains the fugacity z_p equals the density of polymer chains ρ_p^r in the corresponding reservoir. In order to map out the phase diagram we determine the total free energy density $f(\eta_c, z_p)$ for many state points (η_c, z_p) in simulations. We employ common tangent constructions at fixed z_p to obtain the coexisting

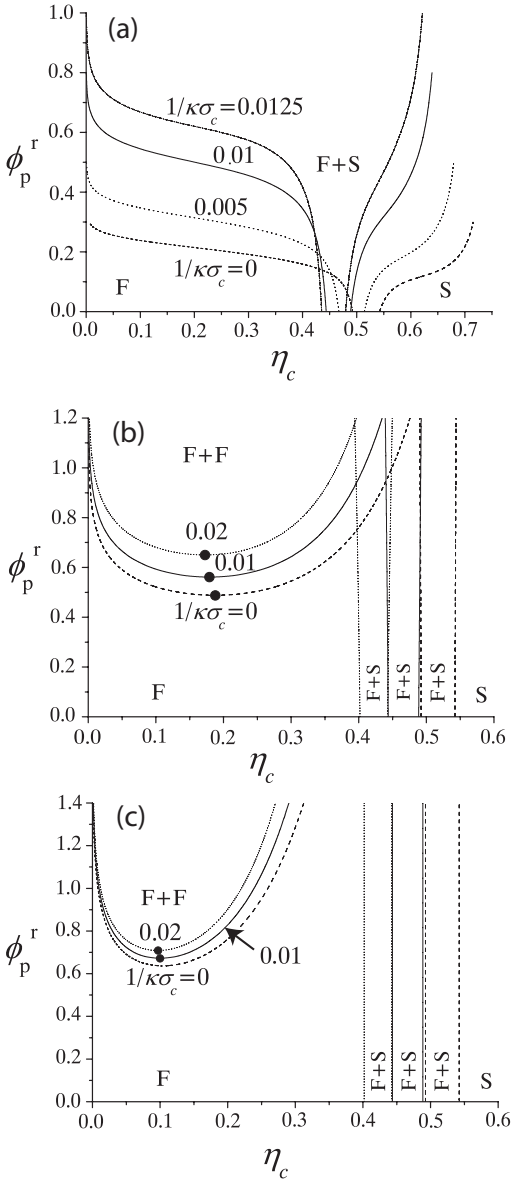

Figure 6.5: Phase diagram of a mixture of charged spheres and ideal polymer as obtained from free volume theory as a function of the colloid volume fractions η_c and the ideal polymer reservoir concentration ϕ_p^r. The screened-Coulomb repulsion (6.1) is characterised by $\beta\epsilon = 20$ and various values of $\kappa\sigma_c$ as indicated. F and S denote the stable fluid and solid fcc phase. $F+S$ denotes the stable fluid-solid coexistence region. $F+F$ denotes the stable fluid-fluid coexistence region (a) For size ratio $q = 0.1$. (b) For size ratio $q = 0.6$. (c) For size ratio $q = 1.0$.

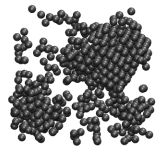

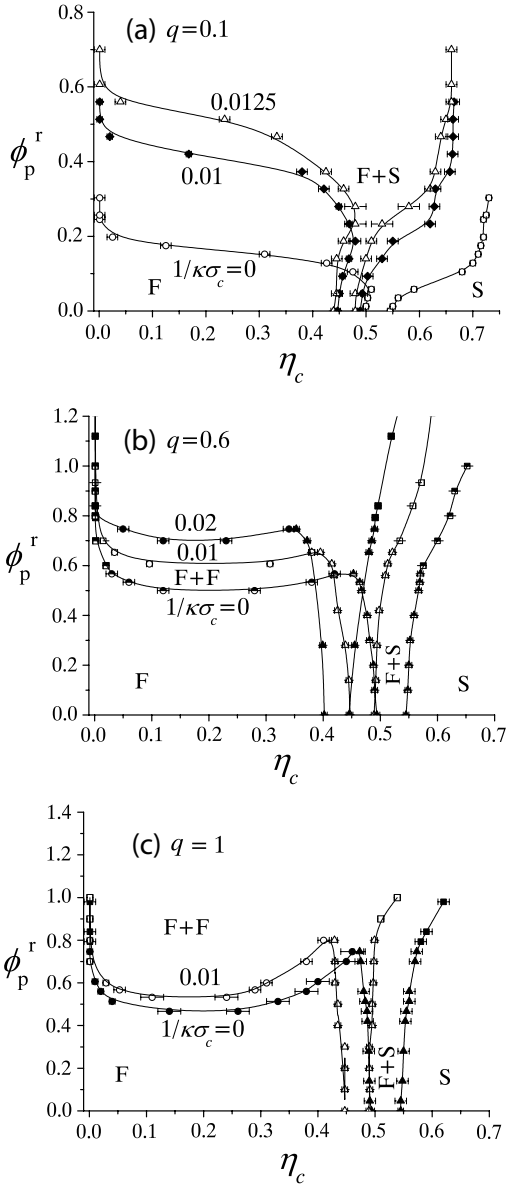

Figure 6.6: Phase diagram of a mixture of charged spheres and ideal polymer as obtained from simulations of the effective pair potential (6.4) as a function of the colloid volume fractions η_c and the ideal polymer reservoir concentration ϕ_p^r. The screened-Coulomb repulsion (6.1) is characterised by $\beta\epsilon = 20$ and various values of $\kappa\sigma_c$ as indicated. The curves serve as a guide to the eye. Open circles correspond to the pure hard-sphere case $(\kappa\sigma_c)^{-1} = 0$, closed circles to a screened-Coulomb repulsion with $(\kappa\sigma_c)^{-1} = 0.01$ and open triangles to $(\kappa\sigma_c)^{-1} = 0.0125$. F and S denote the stable fluid and solid fcc phase. $F + S$ denotes the stable fluid-solid coexistence region. (a) For size ratio $q = 0.1$. (b) For size ratio $q = 0.6$. (c) For size ratio $q = 1.0$.

phases [42]. Fgure 6.6(a) shows the simulation phase diagram for size ratio $q = 0.1$. The results agree semi-quantitatively with the prediction of the theory shown in figure 6.5(a). The main difference is due to the fact that the results of both approaches deviate already for the AOV model (hard-sphere colloids with ideal polymer, i.e., $(\kappa\sigma_c)^{-1} = 0$) [43]. For the AOV model, the theoretical binodal is shifted with a factor of about 1.3 in ϕ_p^r compared to the simulations. This factor between the theoretical predictions and the simulation results is about 1.2 when the screened-Coulomb repulsion is added. We also compare the free volume theory results for the phase behaviour for $q = 0.6$ and 1 as shown in figures 6.5(b),(c) with computer simulations. The phase diagrams obtained from Monte Carlo simulations of the effective one-component systems are plotted in figure 6.6(b), and figure 6.6(c), for size ratios $q = 0.6$, and $q = 1.0$, respectively. The main theoretical trends are also found in the simulation results. Again, the data of the simulations suggest that a higher polymer concentration is required to induce the fluid-fluid transition upon increasing the range of the soft repulsion. We stress that the free volume theory incorporates some of the many-body effects which are present at large q, while our simulations are based on a two-body approximation to the effective Hamiltonian. It is therefore difficult to make a direct comparison between the simulation results and those obtained from free volume theory. However, for $q \leq 0.1547$, the mapping of the charged colloid-polymer mixture onto an effective one-component Hamiltonian based on depletion pair potentials is exact and thus a direct comparison is feasible for our results for $q = 0.1$.

Finally, we convert the polymer reservoir concentration ϕ_p^r to that in the actual system ϕ_p. Figure 6.7(a) shows the conversion of the phase diagram of figure 6.5(a) for $q = 0.1$ and $\beta\epsilon = 20$ and Debye screening lengths $(\kappa\sigma_c)^{-1} = 0$ (dashed curves; the pure hard-sphere case), $(\kappa\sigma_c)^{-1} = 0.005$ (dot-dashed curves), $(\kappa\sigma_c)^{-1} = 0.01$ (full curves) and 0.0125 (dotted curves). The phase stability of a mixture of charged colloids and neutral polymer chains in an aqueous salt solution is thus expected to depend very sensitively on the screening length, and thus on the salt concentration, at least for small size ratios q. In figure 6.7(b), we investigate the effect of $\beta\epsilon$ on the phase behaviour. We plot the converted phase diagram for the same set of parameters as in figure 6.7(a), i.e., $q = 0.1$ and varying Debye screening lengths $(\kappa\sigma_c)^{-1}$, but with $\beta\epsilon = 39$ instead of $\beta\epsilon = 20$. There is a striking similarity between the two sets of results and, hence, we conclude that the effect of $\beta\epsilon$ is not significant. For larger values of $\beta\epsilon$, the system becomes more sensitive to $\kappa\sigma_c$ and thus to the salt concentration. Figure 6.7(c) shows the conversion of the phase diagram as shown in figure 6.5(c) for $q = 1.0$ and $\beta\epsilon = 20$ and Debye screening lengths $(\kappa\sigma_c)^{-1} = 0$ (dashed curves; the pure hard-sphere case), $(\kappa\sigma_c)^{-1} = 0.01$ (full curves) and 0.02 (dotted curves).

It follows that an increase of the reduced Debye length $(\kappa\sigma_c)^{-1}$ shifts the fluid-fluid coexistence curves upwards. Using a PRISM approach, Ferreira *et al.* [135] also found this trend for the spinodal curve of the demixing fluid (see their figure 6.6) based on determining the composition where the inverse structure factor vanishes in the long wavelength limit. Figures 6.5(c) and 6.7(c) show clearly that the shift in polymer concentration of the fluid-fluid binodals for $q = 1$ is weak compared to the shift in the fluid-solid binodals for small q.

A relevant quantity that measures the relative influence of the screened-Coulomb repulsive pair interaction is $(\kappa\sigma_p)^{-1}$ or $(\kappa\sigma_c q)^{-1}$. Hence, the size of the polymer chains (or the depletion thickness) as compared to the range of the repulsion determines the relative

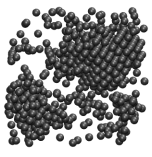

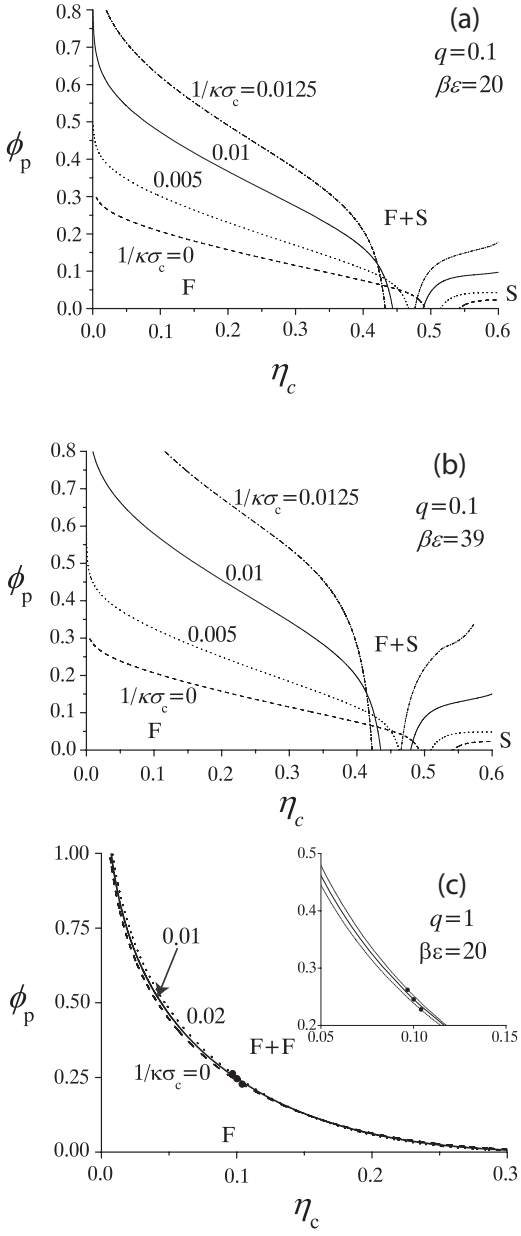

Figure 6.7: Same as figure 6.5 but as a function of the actual ideal polymer concentration ϕ_p. The filled circles indicate the location of the gas-liquid critical points. The inset is a blow-up of the critical region of the liquid-gas binodal.

importance of the screened-Coulomb repulsion on the total *effective* depletion interaction. In biological systems such as charged proteins mixed with neutral polysaccharides, where often $\kappa^{-1} < \sigma_c q$, we expect that the phase behaviour is only moderately sensitive to the salt concentration. Decreasing the salt concentration significantly is then expected to stabilise the charged biocolloid dispersion against depletion-induced demixing. This explains the enhanced miscibility found in mixtures of proteins mixed with neutral non-adsorbing polysaccharides in aqueous salt solutions [36]. In many charged colloidal dispersions the soft repulsion is expected to suppress the depletion effect. In several applications such as paints and food dispersions where colloidal particles are mixed with polymer chains, a screened-Coulomb repulsion helps stabilising the dispersion.

6.6 Conclusions

We have studied the effect of a short-ranged screened-Coulomb repulsion on the phase stability of mixtures containing charged spheres and non-adsorbing polymer chains. The charged spheres are described as hard spheres with an additional screened-Coulomb or Yukawa repulsion with the screening length given by the Debye length κ^{-1}, setting the range of the soft repulsion. The phase behaviour of the charged sphere dispersion is described using standard expressions for the colloidal hard-sphere fluid and fcc crystal with the hard-sphere volume fraction replaced by an *effective* volume fraction that depends on the Yukawa interaction between the spheres. Our results obtained from free volume theory and Monte Carlo simulations show that the additional screened-Coulomb repulsion reduces the depletion effect. For mixtures of small polymers plus relatively large charged spheres the fluid-solid transition is shifted to significantly larger polymer concentrations with increasing Debye screening length κ^{-1}, while for relatively larger polymers the effect is weaker: the resulting fluid-fluid binodal is affected weakly by adding a short-ranged soft repulsion. In general, the range of the screened-Coulomb repulsion compared to the range of the depletion attraction determines qualitatively the reduction of the depletion effect, and hence, the shift of the fluid-fluid and fluid-solid binodals correspondingly. In conclusion, a mixture of charge-stabilised colloids and non-adsorbing polymers at large concentrations of both components can be stabilised by lowering the salt concentration, which increases the range of the screened-Coulomb interaction of the colloids.

Acknowledgements: The theoretical calculations presented in this chapter were performed by Remco Tuinier.

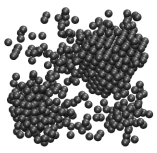

7

Gas-liquid phase separation in oppositely charged colloids: stability and interfacial tension

We study the phase behaviour and the interfacial tension of the screened Coulomb (Yukawa) restricted primitive model (YRPM) of oppositely charged hard spheres with diameter σ using Monte Carlo simulations. We determine the gas-liquid and gas-solid phase transition using free energy calculations and grand-canonical Monte Carlo simulations for varying inverse Debye screening length κ. We find that the gas-liquid phase separation is stable for $\kappa\sigma \leq 4$, and that the critical temperature decreases upon increasing the screening of the interaction (decreasing the range of the interaction). In addition, we determine the gas-liquid interfacial tension using grand-canonical Monte Carlo simulations. The interfacial tension decreases upon increasing the range of the interaction. In particular, we find that simple scaling can be used to relate the interfacial tension of the YRPM to that of the restricted primitive model, where particles interact with bare Coulomb interactions.

7.1 Introduction

Coulombic interactions are important in a wide variety of physical systems such as electrolytes, molten salts, plasmas, colloidal suspensions, micelles, microemulsions, and liquid metals. The screened Coulomb (Yukawa) potential arises naturally for charged particles in the presence of a screening distribution of microions. The phase behaviour of a pure system of hard spheres interacting with screened Coulomb potentials has been well-studied and the phase diagram displays stable fluid, fcc, bcc crystal phase [26, 153–155]. In this chapter, we study a binary fluid of oppositely charged particles using computer simulations. While the phase diagram of the restricted primitive model (RPM), consisting of a binary mixture of equally sized hard spheres carrying opposite charges of equal magnitude, and interacting with bare Coulombic interactions, has been widely studied [156–163], there is little information available on the phase diagram of the Yukawa restricted primitive model (YRPM), where the hard spheres of diameter σ interact with screened Coulomb potentials $u_{ij} = \pm\epsilon\sigma \exp[-\kappa(r_{ij}-\sigma)]/r_{ij}$, with r_{ij} the distance between particles

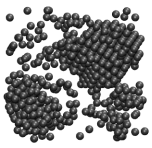

i and j, ϵ the contact value, and κ the Debye screening parameter (inverse of the Debye screening length). Recently Hynninen et al. [164], determined the full phase diagram of the YRPM for a screening parameter $\kappa\sigma = 6$. At high temperatures, the system behaves like a pure hard-sphere system, with a transition between a fluid and a substitutionally disordered fcc phase, where the opposite charges are distributed randomly on a fcc lattice. At lower temperatures, a dilute gas phase coexists with a high density CsCl solid phase, and the gas-liquid transition is metastable with respect to freezing. At high densities, various solid-solid transitions appear, e.g., a transition from CsCl to CuAu and from CuAu to the tetragonal phase. Overall the system exhibits a phase behaviour in striking similarity with the RPM phase diagram [158–161, 164], which displays a fluid-disordered fcc transition at high temperatures, a stable gas-liquid transition at low temperatures, and a fluid-solid transition at higher densities. Since the RPM is the limit of the YRPM for $\kappa\sigma \to 0$, we expect a crossover from a metastable to a stable gas-liquid transition for $0 < \kappa\sigma < 6$.

The gas-liquid transition for a similar model with pair potential $u_{ij} = \epsilon \exp[-\kappa(r_{ij}-\sigma)]$, has been studied using computer simulations [165–167]. This interaction potential differs by a factor σ/r_{ij} from our model. The factor σ/r_{ij} is of the order of unity, and we expect the effect on the phase behaviour to be small. This allows us to compare the results of Refs. [165–167] with the results of the YRPM. In particular Caballero et al. [166], investigated the critical temperature as a function of the screening parameter. In a later paper [167], the stability of the gas-liquid separation with respect to the gas-solid transition was estimated by computing the melting density of the CsCl structure. This technique overestimates the stability of the gas-liquid binodal, with respect to our free energy calculations. We will discuss the relationship between our results and those of Ref. [167] in more detail in Sec. IV.

An experimental realisation of the YRPM is provided by charge-stabilised colloidal suspensions. Recently, it was shown experimentally that the charge on the colloids can be tuned in such a way that oppositely charged colloids can form large equilibrium ionic colloidal crystals [5, 164, 168, 169]. Experiments, theory, and simulations based on screened Coulomb interactions are in good agreement. The system studied in Refs. [5, 164] had a Debye screening parameter $\kappa\sigma \sim 7$, and a gas-liquid phase separation was not observed.

The critical temperature and structure of the YRPM has also been studied using integral equation theory [170], but no information on the stability of the gas-liquid transition with respect to freezing has been given.

In this chapter, we determine the value of the screening parameter $\kappa\sigma$ at which the gas-liquid transition becomes stable for oppositely charged colloids. To this end, we perform Monte Carlo simulations to compute the Helmholtz free energies of the fluid and solid phases of the YRPM. We also study the dependence of the critical parameters and the gas-liquid interfacial tension on the interaction range. The critical parameters and the values of the interfacial tension are calculated using histogram reweighting methods and grand-canonical Monte Carlo simulations.

7.2 Model

We investigate the Yukawa restricted primitive model (YRPM) consisting of N spherical particles with a hard-core diameter σ in a volume V. Half of the spheres carry a posi-

tive charge and the other half a negative charge of the same magnitude. The pair interaction reads

$$\beta u(r_{ij}) = \begin{cases} \infty & r_{ij} \leq \sigma \\ \pm \dfrac{\epsilon_{\mathrm{Y}}}{k_B T} \dfrac{\exp[-\kappa(r_{ij}-\sigma)]}{r_{ij}/\sigma} & \sigma < r_{ij} < r_{\mathrm{cut}} \\ 0 & \text{otherwise} \end{cases} , \tag{7.1}$$

where r_{ij} is the distance between spheres i and j, κ the screening parameter, $\beta \equiv 1/k_B T$ the inverse temperature with k_B the Boltzmann constant and T the temperature, and ϵ_{Y} the contact value of the potential. The cut-off value is $r_{\mathrm{cut}} = 3.6\sigma$. The interaction is attractive for oppositely charged spheres, and repulsive for like-charged spheres. We define a reduced temperature $T^*_{\mathrm{Y}} = k_B T/\epsilon_{\mathrm{Y}}$ and measure particle density in terms of the packing fraction $\eta = (\pi\sigma^3/6)N/V$.

According to the Derjaguin-Landau-Verwey-Overbeek (DLVO) theory [23, 24] explained in section 1.3.2, the effective pair potential between two charged spheres carrying the same number Z of elementary charges e suspended in a sea of salt ions with density ρ_s is given by Eq. (7.1) with a contact value

$$\frac{\epsilon_{\mathrm{Y}}}{k_B T} = \frac{Z^2}{(1+\kappa\sigma/2)^2} \frac{\lambda_B}{\sigma} . \tag{7.2}$$

The Debye screening parameter reads $\kappa = \sqrt{8\pi\lambda_B\rho_s}$, where $\lambda_B = e^2/\epsilon_s k_B T$ is the Bjerrum length and ϵ_s is the dielectric constant of the solvent. It must be noted that, more recent theories on same charged colloidal spheres suspended in a sea of salt ions yield potentials of the form of Eq. (7.1), but with screening parameters that depend on the charged colloid concentration [40, 136–139, 171, 172]. However, the exact functional form is yet unknown [173] and different theories predict varying functional forms. Furthermore, the DLVO theory was not originally derived for oppositely charged spheres, but it can be extended using the linear superposition approximation (LSA) to obtain the potential given by Eqs. (7.1) and (7.2) [174]. The extended DLVO theory has been shown to give good agreement with Poisson-Boltzmann [175] and primitive model calculations [176] at small $\kappa\sigma$, justifying the use potential in Eq. (7.1) with the contact value given by Eq. (7.2). We will refer to the DLVO theory extended by the LSA simply as the DLVO theory. To facilitate the comparison between the results of the DLVO theory for different screening lengths κ, we define a reduced temperature $T^*_{\mathrm{C}} = \sigma/Z^2\lambda_B$ that is independent of κ and equal to the the definition of the reduced temperature of the RPM.

7.3 Simulation Methods

In order to determine the stable phase for a given state point, we compute the Helmholtz free energy as a function of η and T^*_Y. As the free energy cannot be measured directly in a Monte Carlo simulation, we use thermodynamic integration [18, 146, 147] to relate the free energy of the YRPM system to that of a reference system, whose free energy is known. In the thermodynamic integration of the fluid phase, we use the hard-sphere fluid as the

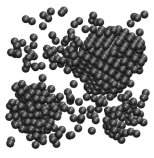

reference state, whereas in the solid phase, the reference state is the Einstein crystal. We use a 10-point Gaussian quadrature for the numerical integrations and the ensemble averages are calculated from runs with 40000 MC cycles (attempts to displace each particle once), after first equilibrating the system during 20000 MC cycles. Employing a common tangent construction on the fluid free energy density curves as a function of η, we find the points of tangency that correspond to the densities of the coexisting gas and liquid phase. A similar common tangent construction is used to determine the coexistence between the fluid and solid phases, and to check whether the gas-liquid separation is stable with respect to the fluid-solid phase coexistence. In addition, we perform a more detailed study of the gas-liquid binodal using methods based on histogram reweighting. To this end, we employ grand-canonical Monte Carlo simulations with successive umbrella sampling [126] to overcome the free energy barrier between the liquid and gas phases. In the successive umbrella sampling method, the probability $P(N)|_{z_+,z_-}$ of having N particles at fugacity $z = z_+ = z_-$, with z_+ and z_- the fugacity of positively and negatively charged colloids, respectively, is obtained by sampling successively 'windows' of particle numbers at a fixed volume $V = L^3$. In each window, the number of spheres N is allowed to fluctuate by one particle, i.e., between 0 and 1 in the first window, 1 and 2 in the second window, etc. We choose at random whether to make an attempt to insert or to remove a particle such that, on average, the system is charge neutral. The sampling of the probability ratio $P(N)/P(N+1)$ is done, in each window, until the difference between two successive samplings of the probability ratio is smaller than 10^{-3}. At phase coexistence, the (normalised) distribution function $P(N)|_z$ becomes bimodal, with two separate peaks of equal area for the liquid and gas phases. To determine phase coexistence we calculate the average number of particles

$$\langle N\rangle = \int_0^\infty NP(N)|_z dN. \tag{7.3}$$

Subsequently, we use the histogram reweighting technique [177] to determine the fugacity z' for which the equal area rule

$$\int_0^{\langle N\rangle} P(N)|_{z'} dN = \int_{\langle N\rangle}^\infty P(N)|_{z'} dN, \tag{7.4}$$

which is the condition for phase coexistence, is satisfied.

The gas-liquid interfacial tension $\gamma_{\rm lg}$ for a finite system with volume $V = L^3$ is obtained from $P(N)|_{z'}$ at coexistence:

$$\beta\gamma_{{\rm lg},L} = \frac{1}{2L^2}\left[\ln\left(\frac{P(N^g_{\rm max}) + P(N^l_{\rm max})}{2}\right) - \ln(P(N_{\rm min}))\right], \tag{7.5}$$

where $P(N^g_{\rm max})$ and $P(N^l_{\rm max})$ are the maxima of the gas and liquid peaks, respectively, and $P(N_{\rm min})$ is the minimum between the two peaks. We determine the bulk interfacial tension $\gamma_{\rm lg}$ by performing simulations for a range of system sizes and by extrapolating the results to the infinite system size using the relation [127, 178, 179]

$$\beta\gamma_{{\rm lg},L} = \beta\gamma_{\rm lg} - \frac{x\ln L}{2L^2} - \frac{\ln A}{2L^2}, \tag{7.6}$$

where A and x are generally unknown. The finite size scaling is performed using the simulation results for box lengths L/σ =8, 10, 12, and 14.

The critical temperature T_{cr} and critical packing fraction η_{cr} are determined by fitting the scaling law

$$\eta_l - \eta_g = f_1 (T_{cr} - T)^{0.32}, \tag{7.7}$$

and the law of rectilinear diameters

$$\frac{\eta_l + \eta_g}{2} = \eta_{cr} + f_2 (T_{cr} - T), \tag{7.8}$$

to the simulation results for the gas (η_g) and liquid (η_l) packing fractions, where f_1 and f_2 are fitting parameters.

7.4 Results

We compute the phase diagram using thermodynamic integration and grand-canonical Monte Carlo simulations for screening parameters $\kappa\sigma$=2, 3, 4, 4.5, and 6. In Fig. 7.1, we show the resulting phase diagrams in the (η, T_Y^*) plane, together with the $\kappa\sigma$=0 phase diagram from Refs. [161] (fluid-solid) and [156, 157] (gas-liquid). The squares denote the results from the free energy calculations, and the circles represent the gas-liquid binodal obtained from the grand-canonical Monte Carlo simulations. We find good agreement between both results. The shaded areas in Figs. 7.1(e)-(f) represent the metastable gas-liquid regions for screening parameters $\kappa\sigma = 6$ and 4.5. For smaller screening parameters, $\kappa\sigma$=4, 3, and 2, the gas-liquid transition is stable, and the phase diagram resembles that of a simple fluid. At sufficiently low temperatures, a gas-liquid phase separation (metastable for screening parameters $\kappa\sigma = 6$ and 4.5) appears at low densities and a fluid-solid transition at high density. At the triple point, the gas, liquid, and the solid phase are in coexistence, while at the critical point, the gas and the liquid phase have the same density. At temperatures below the triple point, a dilute gas coexists with a high density solid, and at temperatures higher than the critical temperature, a fluid coexists with a solid phase. Figure 7.1 shows that the region of stable liquid phase increases upon increasing the range of the interaction, i.e., decreasing $\kappa\sigma$. For simple fluids with short-range attractive Yukawa interactions, square-well attractions, and depletion attractions, the relationship between the range of the attractive interactions and the stability of the gas-liquid transition has been well-studied by computer simulations, density functional calculations, and integral equation theories [180–186]. These studies show that the minimum range of attractions required for a stable gas-liquid transition is about one sixth of the range of the repulsions.

Our results show that the gas-liquid coexistence is stable for $\kappa\sigma \leq 4$, and therefore contradict the findings of Ref. [167], where an estimate $\kappa\sigma \leq 25$ was given. In this comparison, we have to keep in mind that the pair potential used in Ref. [167] did not include the factor $1/r$, which we include. To study the effect of this factor, we repeated our free energy calculations using the pair potential of Ref. [167] for screening length $\kappa\sigma = 6$. The results for this model are presented in Fig. 7.1(f) with a dashed line. We find that there is no qualitative difference between the two models; both predict a metastable gas-liquid transition

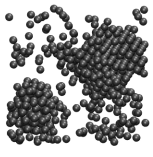

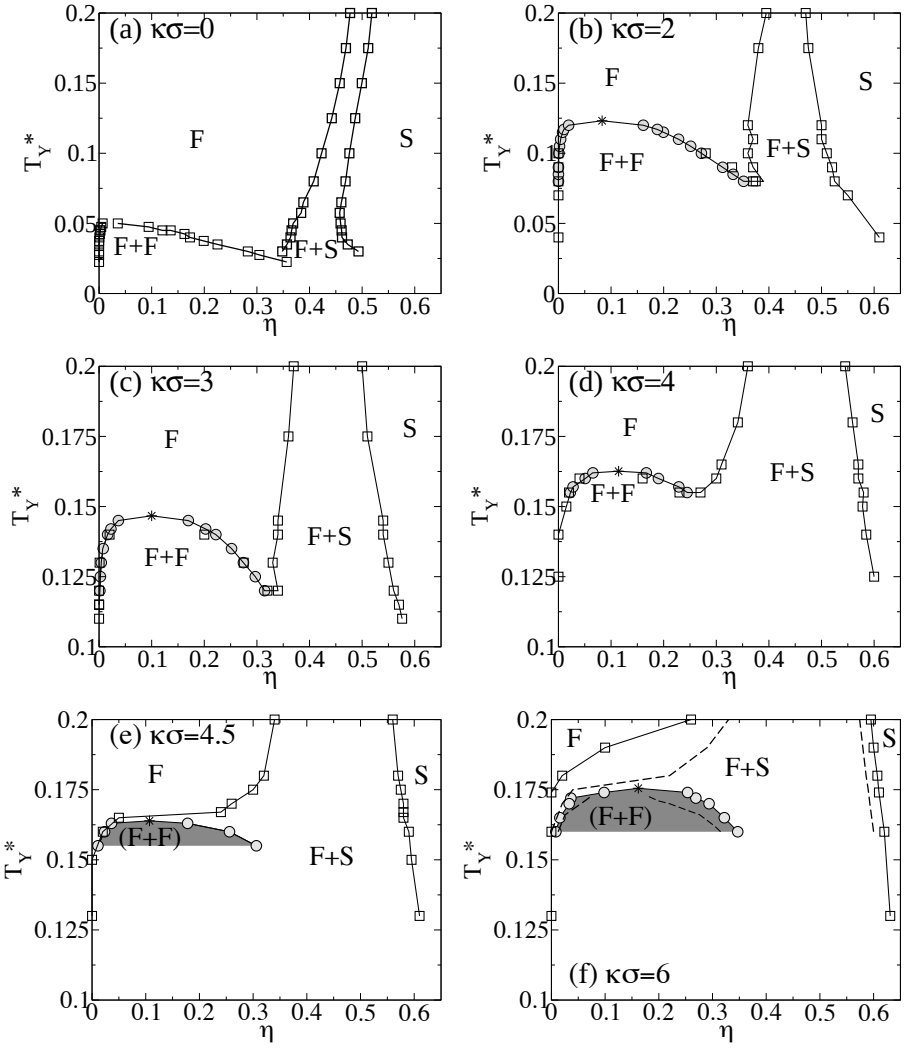

Figure 7.1: Phase diagrams of the YRPM in the reduced temperature T_Y^* - packing fraction η representation for varying Debye screening parameter (a) $\kappa\sigma = 0$ from Refs. [156, 157, 161]; (b) $\kappa\sigma = 2$; (c) $\kappa\sigma$=3; (d) $\kappa\sigma = 4$; (e) $\kappa\sigma = 4.5$; (f) $\kappa\sigma = 6$. The squares are the results from the free energy calculations and the circles are the results from the grand-canonical Monte Carlo simulations. F and S denote the stable fluid and solid (CsCl) phase. F + S and F + F denote, respectively, stable fluid-solid and (meta)stable gas-liquid coexistence region (the shaded regions are metastable). The dashed line in (f) indicates the results of the model used by Caballero and Puertas [167]. The lines are a guide to the eye. Tie lines (not shown) are horizontal.

for screening length $\kappa\sigma = 6$. In Ref. [167], the stability of the gas-liquid transition was determined from the cross-over between the freezing line and the liquid branch of the gas-liquid binodal. The cross-over point was recognised as the gas-liquid-solid triple point. When the triple point was at a lower temperature than the critical point, the gas-liquid phase separation was considered stable. Since the CsCl structure melts in the middle of the broad gas-solid coexistence, the criteria used in Ref. [167] would indicate a stable gas-liquid separation, whereas our free energy calculations show that it is, in fact, metastable. We argue that the computation of the melting line cannot be used to determine the stability of gas-liquid transition with respect to a broad gas-solid coexistence region.

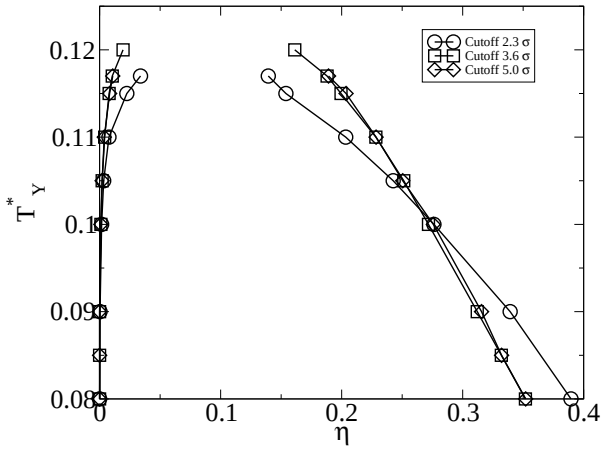

Figure 7.2: Binodals of the YRPM for screening parameter $\kappa\sigma$=2, and cutoff values $r_{\rm cut}/\sigma$=2.3, 3.6, and 5 in the $(\eta, T^*_{\rm Y})$ representation. Statistical errors are of the order of the symbol size. The lines are a guide to the eye.

It is interesting to note that previous simulation studies of a one-component hard-core attractive Yukawa fluid predict a stable gas-liquid transition for $\kappa\sigma = 3.9$, while it is metastable for $\kappa\sigma = 7$ [180, 186], which compares well with our results.

Table 7.1: Critical temperatures $T^*_{\rm Y,cr}$ and packing fractions $\eta_{\rm cr}$ for the YRPM for different values of the Debye screening parameter $\kappa\sigma$. The GMSA theory data is from Ref. [170].

	Simulation		GMSA theory	
$\kappa\sigma$	$T^*_{\rm Y,cr}$	$\eta_{\rm cr}$	$T^*_{\rm Y,cr}$	$\eta_{\rm cr}$
6	0.1755 (5)	0.162(8)	0.16053	0.07875
4	0.1626 (1)	0.114(3)	0.16498	0.06263
3	0.1467(1)	0.100(1)	0.16240	0.05009
2	0.1232(8)	0.083(1)		
0	0.0490(3)[1]	0.037(3)	0.07858	0.00758

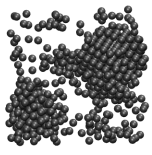

In Figure 7.2, we analyse the effect of the cutoff value of equation (7.1) on the liquid-gas binodal. Huge deviations are expected as the interaction becomes longer ranged. We used three different cutoff values $r_{\rm cut}/\sigma = 2.3, 3.6, 5$ for the calculation of the liquid-gas binodal for our longest range interaction ($\kappa\sigma = 2$). The binodals for cutoff values $r_{\rm cut}/\sigma = 3.6$, and 5 are equivalent within the statistical accuracy, thereby justifying the choice of a cutoff value $r_{\rm cut}/\sigma = 3.6$ in all subsequent calculations.

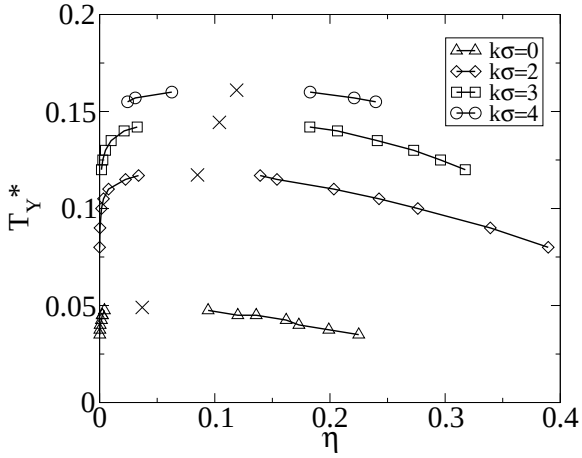

Figure 7.3: Binodals and the critical points of the YRPM for screening parameters $\kappa\sigma$=0, 2, 3, and 4, in the $(\eta, T_{\rm Y}^*)$ representation. Crosses denote the location of the critical points. The binodal for $\kappa\sigma$=0 (RPM) is taken from Ref. [156] and the critical point from Ref. [187]. The lines are a guide to the eye.

Table 7.1 summarises the critical temperatures $T_{\rm Y,cr}^*$ and critical packing fractions $\eta_{\rm cr}$ as found from our simulations and from the generalised mean spherical approximation (GMSA) theory [170] for different values of $\kappa\sigma$, while Figure 7.3 shows the (stable) gas-liquid binodals for $\kappa\sigma$=2, 3, and 4, in the $(\eta, T_{\rm Y}^*)$ representation. Table I and Fig. 7.3 show that, for $0 \leq \kappa\sigma \leq 6$, the reduced critical temperature $T_{\rm Y,cr}^*$ and the critical packing fraction $\eta_{\rm cr}$ decrease for increasing range of the interaction, i.e., decreasing $\kappa\sigma$, in agreement with the findings of Caballero et al. [166]. The non-monotonic behaviour of the critical temperature as a function of $\kappa\sigma$ that was reported in Ref. [166] for screening parameters $\kappa\sigma > 10$ is in the region where we claim the gas-liquid phase separation to be metastable. As can be seen from Table I, the GMSA theory predicts a non-monotonic behaviour of the critical temperature as a function of $\kappa\sigma$. Comparing the theoretical results with our simulations, we observe that the GMSA theory overestimates the critical temperature for $\kappa\sigma < 6$ and underestimates it at $\kappa\sigma = 6$. On the other hand, the GMSA theory underestimates the critical packing fraction for all values of $\kappa\sigma$.

Figure 7.4(a) shows the binodals of the YRPM and the RPM in the corresponding state representation, where the reduced temperature $T_{\rm Y}^*$ is scaled with the critical temperature $T_{\rm Y,cr}^*$, and the packing fraction η is scaled with the critical packing fraction $\eta_{\rm cr}$. We see that the binodals do not collapse on a single master-curve, but instead, the RPM binodal (where $\kappa\sigma = 0$) differs considerably from the YRPM binodals (where $\kappa\sigma = 2, 3,$ and 4). This

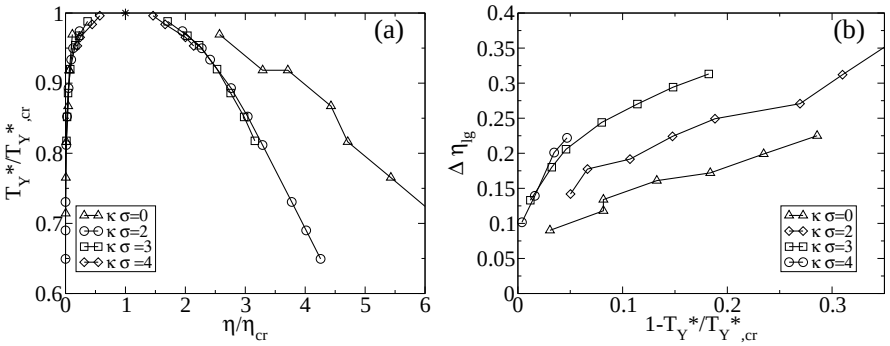

Figure 7.4: (a) Binodals of the YRPM and the RPM in the corresponding state representation for Debye screening parameters $\kappa\sigma = 2, 3$, and 4. The reduced temperature T_Y^* is scaled with the critical temperature $T_{Y,cr}^*$ and the packing fraction η is scaled with the critical packing fraction η_{cr}. The binodal for $\kappa\sigma$=0 (RPM) is from Ref. [156] and the critical point from Ref. [187]. (b) The difference in coexisting packing fractions $\Delta\eta_{lg} = \eta_l - \eta_g$ is plotted against $1 - T_Y^*/T_{Y,cr}^*$.

finding is in agreement with the prediction of the GMSA theory [170]. In Fig. 7.4(b), we plot the width of the gas-liquid separation, $\Delta\eta_{lg} = \eta_l - \eta_g$, as a function of $1 - T_Y^*/T_{Y,cr}^*$. We see that for a fixed $1 - T_Y^*/T_{Y,cr}^*$, the width of the gas-liquid separation decreases with increasing range of the interaction, resulting in a smaller density gap between the coexisting liquid and gas phase for longer-ranged interactions.

Figure 7.5 shows the gas-liquid interfacial tension, scaled with the contact value energy ϵ_Y, for different values of the screening parameter $\kappa\sigma$. For comparison, we also show the interfacial tension of the RPM from Ref. [188]. As can be seen from Fig. 7.5, the value of the dimensionless interfacial tension increases with increasing $\kappa\sigma$. This can be understood on the basis of Fig. 7.4(b), which shows that, with increasing $\kappa\sigma$, the density gap of the coexistence region increases, meaning that the interfacial tension increases. The inset of figure 7.5 shows a log-log plot of $\gamma_{lg}\sigma^2/\epsilon_Y$ versus $1 - T_Y^*/T_{Y,cr}^*$ in the vicinity of the critical point, which can be used to extract an estimate for the critical exponent of the correlation length ν. We found $2\nu \simeq 1.1$ for all screening parameters $\kappa\sigma$, by performing a linear fit on the data, which differs from the Ising model result $2\nu = 1.32$ [127], and from the accepted value of $2\nu = 1.26$ [189, 190]. The value of the correlation length is very sensitive to the extrapolated surface tension to infinite system sizes. In order to improve the statistical accuracy of the simulations, larger system sizes, as well as longer runs are needed, especially close to the critical point. Nevertheless, our results are compatible within the simulation error, with the theoretical prediction of the correlation length (dashed line in the inset of figure 7.5).

We now interpret our results in view of the DLVO theory. In the DLVO theory, the contact value ϵ_Y, and hence the reduced temperature $T_Y^* = k_B T/\epsilon_Y$, depend on the salt concentration ρ_s through the screening parameter $\kappa\sigma$, see Eq. (7.2). In Fig. 7.6(a), we plot the gas-liquid binodals and critical points for $\kappa\sigma$=0, 2, 3, and 4, using the reduced temperature $T_C^* = \sigma/Z^2\lambda_B$ that does not depend on $\kappa\sigma$. As can be seen from Fig. 7.6(a), the reduced critical temperature $T_{C,cr}^*$ decreases with increasing $\kappa\sigma$, or salt concentration. This means that, at a fixed T_C^* and at a statepoint inside the gas-liquid coexistence region, adding salt

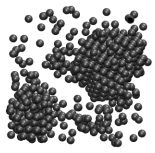

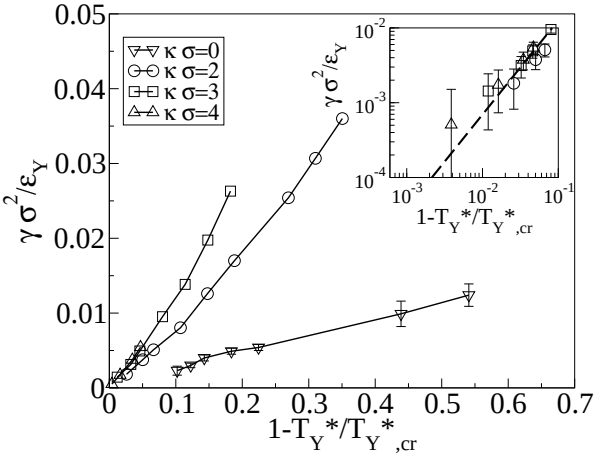

Figure 7.5: Dimensionless gas-liquid interfacial tension $\gamma_{lg}\sigma^2/\epsilon_Y$ as a function of $1-T^*_{Y,cr}/T^*_Y$. The data for $\kappa\sigma = 0$ is from Ref. [188]. Inset: log-log plot of the dimensionless interfacial tension in the vicinity of the critical point. The dashed line is the theoretical prediction[189, 190] $\gamma \sim (T^*_{Y,cr} - T^*_Y)^{1.26}$.

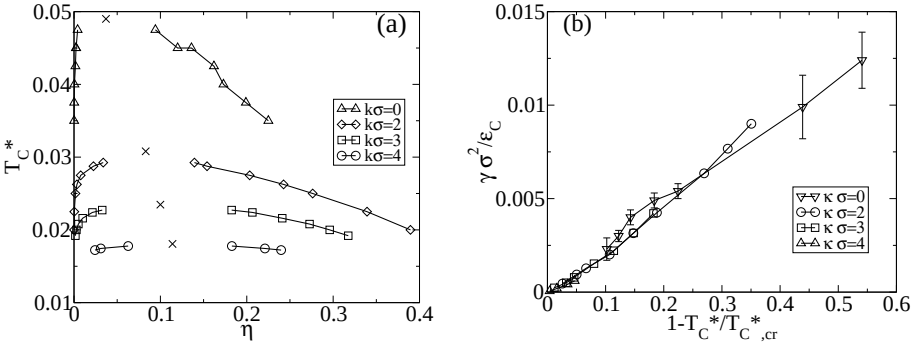

Figure 7.6: (a) Binodals of the YRPM, for Debye screening parameters $\kappa\sigma$ =0, 2, 3, and 4, in the reduced temperature T^*_C and the packing fraction η representation. The binodal for $\kappa\sigma$=0 (RPM) is from Ref. [156] and the critical point from Ref. [187]. (b) Dimensionless gas-liquid interfacial tension $\gamma_{lg}\sigma^2/\epsilon_C$ as a function of $1-T^*_Y/T^*_{Y,cr}$. Remember that $T^*_C/T^*_{C,cr} = T^*_Y/T^*_{Y,cr}$. The data for $\kappa\sigma = 0$ is from Ref. [188].

decreases the density difference between the gas and the liquid phases, until, at the critical salt concentration, the density difference disappears. This finding could be confirmed by performing simulations with explicit co- and counterions [173, 191], and could be used to experimentally test the validity of the DLVO theory for oppositely charged colloids. Figure 7.6(b) shows the interfacial tension scaled with the contact value $\epsilon_C = \frac{Z^2 k_B T \lambda_B}{\sigma}$, and as can be seen, the interfacial tensions for different $\kappa\sigma$ collapse to a single line. This suggests that the interfacial tension is determined solely by the contact value and not by the range of the interaction.

7.5 Conclusions

We have used a combination of MC free energy calculations and grand-canonical MC simulations to determine the stability and the interfacial tension of the gas-liquid phase separation in a binary mixture of oppositely charged hard spheres, which interact via screened-Coulomb (Yukawa) potentials. We find that the gas-liquid coexistence is stable with respect to gas-solid coexistence for values of the screening parameter $\kappa\sigma \leq 4$. This value is similar to what is found for the single component attractive Yukawa model [186], where the gas-liquid transition is stable at $\kappa\sigma = 4$ and metastable at $\kappa\sigma = 7$.

We have studied the dependence of the critical temperature as a function of the range of the Yukawa interaction. If the contact value of the interaction potential does not depend on the screening length, it is possible to define a reduced critical temperature simply as the inverse of the Yukawa contact value. With this definition, the reduced critical temperature decreases upon increasing the range of the interaction, which is in agreement with Ref. [166].

We have related the Yukawa restricted primitive model (YRPM) to the DLVO theory, which was recently used to explain experimental results on oppositely charged colloids [5, 164, 169, 192]. The DLVO theory predicts a contact value that depends on the screening length. Thus, in order to facilitate the comparison between the results for different screening lengths, we define a temperature scale that is independent of the screening length. The natural choice is the reduced temperature of the RPM, which is the limit of zero screening length of the DLVO theory. With this definition, the reduced critical temperature decreases upon increasing the range of the interaction. This means that upon adding salt to a system at fixed temperature and at a statepoint in the gas-liquid coexistence region, the density difference between the gas and liquid phases decreases, and finally disappears at the critical salt concentration. This prediction could be tested by computer simulations with explicit co- and counterions [173, 191], and could be used to study experimentally the validity of the DLVO theory for oppositely charged colloids.

Finally, we have studied the gas-liquid interfacial tension using histogram reweighting methods. We find that the dimensionless tension decreases for decreasing screening parameter. Upon scaling the interfacial tension with the contact value of the Coulomb interaction, we observed a collapse of the interfacial tensions onto a single curve. This means that for state points at coexistence and at the same scaled temperature $T^*_C / T^*_{C,cr}$, the interfacial tension is determined solely by the contact value and not by the range of the interaction. There might be a possible connection with the well known similarities be-

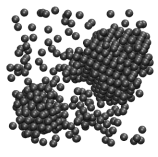

tween the structures of the RPM and of the YRPM. Larsen and Rogde [193] noted that their Monte Carlo results for the radial distribution functions of the YRPM were similar to those obtained for the RPM at different state points. The structurally equivalent states were further investigated by Copestake and Evans [194] and by Leote de Carvalho and Evans [170]. This correspondence is due to the screening of charges in the RPM, which in turn is due to charge ordering.[170, 193, 194] Consequently, the potential of mean force between two ions decays more rapidly than the bare Coulomb potential, and for certain state points the potentials of mean force will be similar for the YRPM and the RPM.

8

Brownian dynamics simulations of phase-separating colloid-polymer mixtures

We study a mixture of monodisperse colloidal hard spheres and ideal polymers described by an effective one-component system, in which the colloids interact with a short-range effective Asakura-Oosawa potential. We determine the equilibrium bulk phase diagram using free energy calculations. The phase diagram displays a broad fluid-solid coexistence region and a metastable gas-liquid regime. We divide the phase diagram in different kinetic regimes according to Evans et al. [195]. We carry out Brownian dynamics simulations to study the dynamic evolution of the different kinetic pathways. In agreement with Cates et al. [196], we find a fluid of 'long-lived' clusters in the binodal regime at low colloid packing fractions. In the spinodal regime, we observe at low colloid packing fractions a phase of crowded clusters that can merge and break-up again, and a kinetic arrested spinodal decomposition at higher packing fractions. At even higher colloid densities, a homogeneous gel phase is observed, which can be viewed as an attractive glass phase. The structure of the clusters are crystal-like at low attractive interactions and glassy at high attraction strengths.

8.1 Introduction

The structure and the equilibrium phase behaviour of colloid-polymer mixtures and of particles with short-range interactions in general depend strongly on the range and the strength of the interaction [29, 30, 32, 35, 43]. The scenario is further enriched by the presence of non-ergodic states like glasses [4, 197–199] and gel-like phases [200–207] that can form in certain regions of the phase diagram [208].

A fluid of hard spheres crystallises when the packing fraction is larger than $\eta = 0.545$ but arrests into a colloidal glass phase for packing fractions larger than $\eta \gtrsim 0.58$ [4]. In a colloidal glass, the particles are arrested as they become localised in a "cage" formed by the surrounding spheres [199]. Hence, the system is trapped in a non-ergodic state, and the lowest free energy state, i.e., the ordered crystal phase, is unreachable. Experiments on

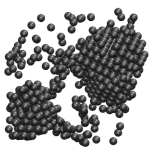

colloidal hard spheres in a space-shuttle (microgravity) show, however, crystallisation at $\eta = 0.619$ [209], while vitrification is observed for these samples on earth (normal gravity). It is clear that an external field, e.g., gravity or a centrifugal field, has a pronounced effect on the glass transition.

Interestingly, the addition of non-adsorbing polymer, resulting in an effective attraction between the colloids can enhance the relaxation processes, the cage of surrounding particles becomes looser due to the natural tendency of particles to get closer together. Therefore, the particles can escape the cage and the system can crystallise. The so-called 'repulsive' glass transition moves towards higher packing fractions upon increasing the attraction between the particles. Nevertheless, for increasing attraction strengths the particles become more and more localised due to long-lived bonds between the neighbouring particles. This type of arrested state due to bonding is called an attractive glass. The interpretation of glassy dynamics is mainly due to the developments of the Mode Coupling Theory (MCT) [210–213].

Recent studies show that the transition from fluid to attractive glass moves towards lower packing fractions for increasing attraction, until it meets the metastable gas-liquid binodal on the liquid side [214, 215]. This finding supports the hypothesis that gel-like states are due to an MCT-like dynamical arrest of a percolating cluster in the system: the phase separation is arrested because the liquid-like clusters crosses the glass transition [204]. It is worth noting that a percolating arrested cluster is required to sustain stress in a macroscopic gel. These clusters can result from spinodal decomposition, binodal decomposition (nucleation and growth) [196], or diffusion limited aggregation for sufficiently high attractions, when the particles stick irreversible to each other. On the other hand other mechanisms like aggregation or percolation [200, 216–221], can be responsible for the gel transition. Recent experiments [206] identified indeed the importance of the MCT glass transition in the formation of gels in the region of the metastable gas-liquid phase separation. At these intermediate packing fractions gelation is driven by a spinodal decomposition into an interconnected colloid-rich network, followed by dynamic arrest due to a local glass transition [206]. However, some differences in the ageing dynamics between high density glasses and the percolated structures were pointed out by Foffi et al. [222]. At lower packing fraction a state of disconnected (glassy) clusters exists as a precursor to gelation [205, 223–226]. Subsequently, these clusters can grow and form a gel by cluster-cluster aggregation. At even lower colloid packing fractions, 'long-lived' fluid clusters has been reported recently in experiments on colloid-polymer mixtures [227]. It is important to stress that these clusters are not stabilised by a competition between short-range attractions and long-range Coulombic repulsions as in Ref. [224, 228, 229]. The mechanisms behind all these non-equilibrium structures and their relation with the equilibrium phase diagram and distinct kinetic pathways are still unclear.

In many simulation studies on the gel formation and the glass transition, it is common place to suppress the metastable phase separation by adding a long-range repulsive barrier [196, 230] or by decreasing the maximum valency [207, 231]. In addition, a polydisperse system of colloids is often used to prevent crystallisation. However, the effect of these changes to the particle interactions on the bulk phase diagram is never investigated in great detail.

In this chapter, we study a monodisperse system of hard spheres with short range at-

tractive interactions. It is straightforward to determine the equilibrium phase diagram for this system using free energy calculations. We then perform extensive Brownian dynamics simulations at fixed range of interaction and varying colloid packing fractions and strengths of the interaction. We study the morphology of the resulting crystallites, glassy and gel-like phases, and their relation to the equilibrium phase diagram and the different available kinetic pathways [195, 232].

8.2 Model and Method

We study a system of N_c hard spheres of diameter σ_c and non-adsorbing polymers with diameter σ_p described by the AOV model. The polymers induce a short range attractive interaction between the colloids given by the AO potential (1.24)

$$\beta U_{\rm dep}(R_{ij}) = \begin{cases} -\eta_p^r \frac{(1+q)^3}{q^3}\left[1 - \frac{3R_{ij}}{2(1+q)\sigma_c} + \frac{R_{ij}^3}{2(1+q)^3\sigma_c^3}\right] & \sigma_c < R_{ij} < \sigma_c + \sigma_p \\ 0 & R_{ij} > \sigma_c + \sigma_p \end{cases} \tag{8.1}$$

where $R_{ij} = |\vec{R}_i - \vec{R}_j|$ is the distance between two colloidal particles, with $\vec{R}_i$ the position of the centre-of-mass of colloid i. The size ratio $q = \sigma_p/\sigma_c$ determines the range of the interaction. The polymer reservoir packing fraction $\eta_p^r = \pi/6\sigma_p^3\rho_p^r$, is proportional to the density of polymer ρ_p^r in a reservoir in osmotic contact with the system of interest. This parameter controls the strength of attraction. In addition, we define $\beta U = \beta U_{\rm dep}(R_{ij} = \sigma_c)$ as a measure of the interaction strength.

We determine the phase diagram by calculating the dimensionless free energy density $f = \beta F/V$ as a function of the colloid packing fraction η_c and the polymer reservoir packing fraction η_p^r with Monte Carlo simulations. We use thermodynamic integration to relate the free energy of the effective system to that of a reference system at the same colloid volume fraction η_c. To this end, we write the total free energy density as the sum of two contributions

$$f(N_c, V, \eta_p^r) = f_c(N_c, V) + f_{\rm dep}(N_c, V, \eta_p^r)\,, \tag{8.2}$$

where $f_c(N_c, V)$ is the free energy density of a system of N_c hard spheres in a volume V, for which we used the Carnahan-Starling expression [144] for the fluid phase, and the Hall expression [233] for the face-centred-cubic (f.c.c.) solid phase. The free energy density $f_{\rm dep}$ is the contribution of the depletion potential (8.1) to the free energy density, and it is computed using the λ-integration [18]. In order to map out the phase diagram we determine the total free energy density $f(\eta_c, \eta_p^r)$ for many state points (η_c, η_p^r) in simulations, and we employ common tangent constructions at fixed η_p^r to obtain the coexisting phases [42].

To study the dynamics of the system we carry out standard Brownian dynamics [15] simulations based on the Langevin equation for N_c particles of radius $r_c = \sigma_c/2$, and mass m

$$m\ddot{\vec{r}}_i = -\vec{\nabla}U_i - \xi\dot{\vec{r}}_i + \vec{F}_i\,, \tag{8.3}$$

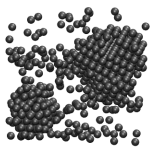

where U_i is the potential energy of particle i in the field of $N-1$ particles, ξ is the friction coefficient, and $\vec{F}_i$ is a random force acting on particle i. We neglect the inertia term $m\ddot{\vec{r}}_i$ and the equation (8.3) reduces to

$$\dot{\vec{r}}_i = \frac{1}{\xi}(-\vec{\nabla}U_i + \vec{F}_i)\,, \tag{8.4}$$

that we solve using the Euler forward algorithm. The time step δt is chosen to be much larger than the velocity relaxation time ($\simeq mD_0/k_BT$), and much smaller than the diffusion time $\tau_D = r_c^2/D_0$, where D_0 is the Stokes-Einstein diffusion coefficient. We use Stokes law for the friction coefficient $\xi = 6\pi\nu r_c$, where ν is the viscosity of the solvent. We neglect all hydrodynamic interactions between the particles. The random forces $\vec{F}_i$ mimic the interaction between particles and solvent, and are sampled from a Gaussian distribution with variance $2D_0\delta t$. The random force and the dissipative term provide the system with a heat bath at constant temperature. In the Brownian dynamics simulation we replace the hard-core potential with the repulsive soft potential $1/r^{36}$.

We characterise the local structure around a particle i by the set of numbers

$$q_{lm}(i) = \frac{1}{N_b(i)}\sum_{j}^{N_b(i)} Y_{lm}(\vec{r}_{ij})\,, \tag{8.5}$$

where $Y_{lm}(\vec{r}_{ij})$ are spherical harmonics, $\vec{r}_{ij}$ is a unit vector in the direction of the bond between particle i and particle j. The sum runs over all $N_b(i)$ neighbours of particle i. We then construct the dot product

$$q(ij) = \vec{q}_l(i)\cdot\vec{q}_l(j) = \sum_{m=-l}^{l} q_{lm}(i)q^*_{lm}(j)\,, \tag{8.6}$$

where i and j are neighbouring particles, and $q^*_{lm}(i)$ is the complex conjugate of $q_{lm}(i)$. We normalised the vector $\vec{q}_l(i)$, such that $\vec{q}_l(i)\cdot\vec{q}_l(i) = 1$. In our analysis two particles are defined as neighbours if their separation is smaller then a cutoff value of 1.25 σ_c, corresponding to the position of the minimum between the first and second peak of the radial distribution function. Two particles are defined to be joined by a crystal bond if the factor $q(ij) > 0.5$. Particle i is crystal-like if at least 7 of its bonds with neighbouring particles are crystal-like [234]. As in other studies [10] we use the l=6 order parameter.

8.3 Results

Fig. 8.1 shows the equilibrium phase diagram obtained from free energy calculations for size ratio $q = 0.15$, in the attraction energy βU (polymer reservoir packing fraction η_p^r), colloid packing fraction representation. For βU=0 we recover the hard sphere phase diagram with a fluid phase at packing fraction $\eta_c \simeq 0.494$, at coexistence with an f.c.c. crystal at packing fraction $\eta_c \simeq 0.545$. For increasing βU the region of fluid-solid coexistence opens up. At the critical energy $\beta U_{cr} \simeq$2.3 ($(\eta_p^r)_{cr} \simeq 0.316$) we find a metastable gas-liquid transition. In Fig. 8.1 we plot the metastable gas-liquid binodal and spinodal denoted by the

circles and crosses, respectively. The geometric percolation line indicates at which colloid packing fraction one cluster spans the system with a probability of 50% [235]. Note that the percolation line crosses the gas-solid binodal and that the percolation line follows closely the gas-liquid spinodal.

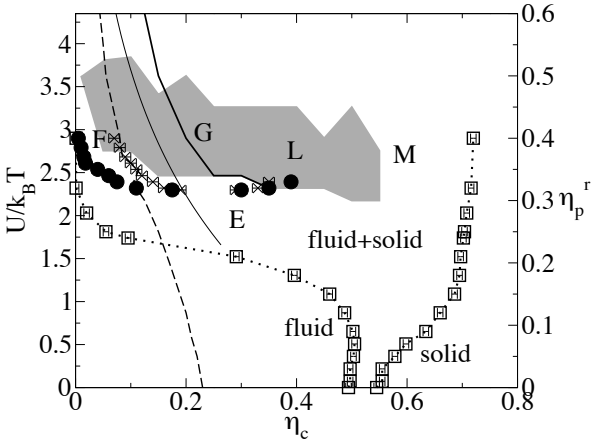

Figure 8.1: Phase diagram in the attraction energy βU colloid packing fraction η_c representation. The squares indicate the fluid-solid coexistence densities. Also shown are the metastable gas-liquid binodal (circles) and spinodal (crosses). The dotted lines are a guide to the eye. The dashed line indicate the geometric percolation transition, while the continuous line is the limit of the region of clusters formation. The dark shaded area is the region where the fraction of crystalline particles is larger than 0.2. The thin continuous line indicates the transition from ergodic to non-ergodic fluid of clusters according to Segrè et al. [223].

For the topology of the phase diagram considered here we can identify five different regimes using the Cahn construction [236] on the free energy density curves shown schematically in Fig. 8.2. Following the notation of Evans et al. [195] we indicate the kinetic regimes as E, F, G, L, and M, as shown in Fig. 8.1. The common tangent construction in Fig. 8.2(a) shows that for all statepoints with $\eta_{gas} < \eta_c < \eta_{cry}$ the system can lower its free energy by gas-solid phase separation with coexisting densities η_{gas} and η_{cry}. Consider the initial state point A denoted by an asterisk on Fig. 8.2(a), which is in regime E. Drawing a tangent (line α) to this point one can easily see that the tangent lies below the gas minimum, but above the solid minimum. Hence, 'positive' free energy Δf is available to nucleate the crystal phase from the fluid phase. For higher η_p^r typical free energy density curves are drawn in Fig. 8.2(b). The curves show three minima, corresponding to the gas, liquid and crystal phase. Moreover one can observe a stable gas-solid transition and a metastable gas-liquid transition shown by the two corresponding common tangent constructions (line α and β, respectively). One can now divide the free energy curve for the fluid phase in five different regions. If we consider an initial state in regime M, that is outside the metastable gas-liquid coexistence region, we can easily see that the tangent to a point on the fluid branch lies below the gas minimum, but above the solid minimum.

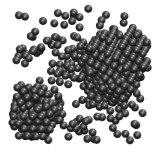

Hence, only crystallites can be nucleated which must be coated with gas phase because no tangent can be drawn between the liquid and the crystal phase. Similarly, one can determine that in regime F, either crystal nucleation from the supersaturated gas phase is possible, or more likely crystal formation from an intermediate liquid phase. Regime G corresponds to spinodal decomposition of gas and liquid. Subsequently crystallites can be nucleated from the dense phase. In regime L gas bubbles or crystals can be nucleated. In this chapter we concentrate on the pathways F, G, and L, where there is a competition between gas-liquid phase separation and crystal nucleation [195]. Furthermore non-equilibrium effects like aggregation and glass transition can influence the kinetics dramatically [196].

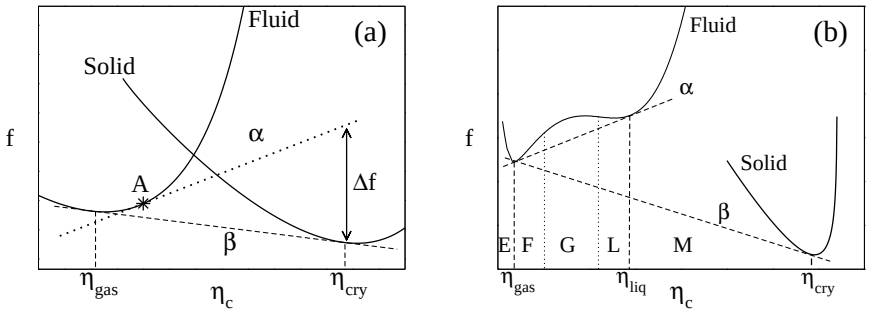

Figure 8.2: Schematic fluid and solid free energy density curves of a system with short range attractive interaction at fixed interaction strength βU (η_p^r). (a) Low attraction strength. Only gas-solid phase separation is possible. The vertical dashed lines indicate the packing fractions η_{gas} and η_{cry} of the coexisting gas and solid phase, respectively. Also shown is the common tangent between the fluid and solid curves (line β) and the tangent (line α) to the state point A. (b) High attraction strength. The fluid free energy curve shows two minima, corresponding to the metastable gas and liquid phases, with packing fractions η_{gas} and η_{liq}, respectively. Vertical dashed lines indicate the position of the minima in the free energy curves. Vertical dotted lines denote the limit of the spinodal decomposition region. The line α indicate the common tangents between gas and liquid phases, while the line β is the common tangent between between the gas and solid phases.

In order to study the dynamic evolution of the different kinetic regimes we carry out Brownian dynamics simulations in a box with dimension $L_x \times L_y \times L_z$ with number of particles N_c ranging from 600 to 1000. The time step is chosen to be $\delta t = 5 \times 10^{-6} \tau_B$. Starting from homogenous configurations the system is instantaneously quenched to a state point in one of the kinetic regimes. We studied the evolution of the system for a total time $t = 35\tau_B$, plus few runs up to $t = 105\tau_B$ to evaluate the ageing of the quenched structures.

In Fig. 8.3 we report examples of the calculated fraction f_{cr} of crystal-like particles as a function of the interaction energy U/k_BT for varying colloid packing fraction η_c. We observe a sharp increase of crystal nucleation for energies larger than the critical energy. The fraction of crystal-like particles reaches a maximum and slowly decreases for increasing attraction energy. The dark grey area in Fig. 8.1 shows the region where $f_{cr} > 0.2$ at $t = 35\tau_B$. For $U/k_BT \gtrsim 3.26$ ($\eta_p^r \simeq 0.45$) the fraction of crystalline particles is almost zero and the system is glassy. In Ref. [237] the attractive glass transition was predicted to be at

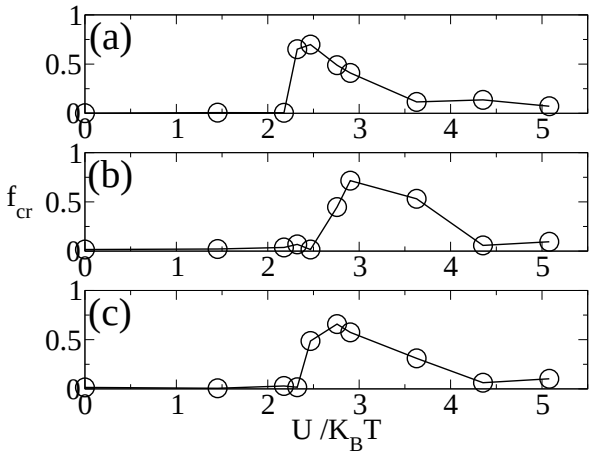

Figure 8.3: Fraction of crystal-like particles as a function of the interaction energy (a) η_c=0.10. (b) η_c=0.25. (c) η_c=0.40

.

$\eta_p^r \simeq 0.43$ for a system with size ratio $q = 0.1$, and using a pair potential that included a long-range repulsive barrier to prevent gas-liquid phase separation. This value is remarkably close to our estimate. Note that the boundary is nearly horizontal which is consistent with the picture that gel formation is due to the intersection of the attractive glass line with the gas-liquid binodal.

In regime F we observe the nucleation of fluid-like clusters (Fig. 8.4(a)) as expected on the basis of the Cahn construction. For attraction energy $\beta U \simeq 2.5$ (η_p^r=0.34) we observe that the fluid clusters subsequently transform into crystal-like clusters. At higher attraction energy $\beta U \simeq 4.35$ (η_p^r=0.6) which is in regime G the clusters remain in a fluid-like (probably glassy) state, with few crystal-like particles (Fig. 8.4(b)). Fig. 8.5 shows the evolution in the number of clusters in the simulation box for packing fraction η_c=0.10. In Fig. 8.5(a) we show the evolution of the number of clusters for a state point within pathway F. We observe the formation of clusters due to nucleation. The number of clusters decreases exponentially due to coalescence or growth.

We observe cluster formation also for the state points whose evolution is reported in Fig. 8.5(b),(c) that correspond to state points within regime G. The spinodal decomposition is much faster than crystal nucleation because there are no energy barriers involved. Fig. 8.6 shows the evolution in the number of clusters in the simulation box for packing fraction η_c=0.25. All these state points lie in regime G. Fig. 8.6(a) shows the evolution for energy $\beta U \simeq 2.3$ (η_p^r=0.32). There is immediate percolation due to spinodal decomposition, but the increasing noise at longer times indicates the formation of reversible clusters in the system, the clusters can form and break-up again (Fig. 8.7(a)). The thick continuous line in Fig. 8.1 shows the crossover between the region where the spinodal decomposition is arrested (right side), and the region (left side) where clusters can form due to coarsening of spinodal decomposition or aggregation. Moreover another line (thin continuous

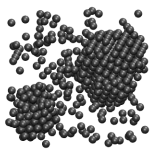

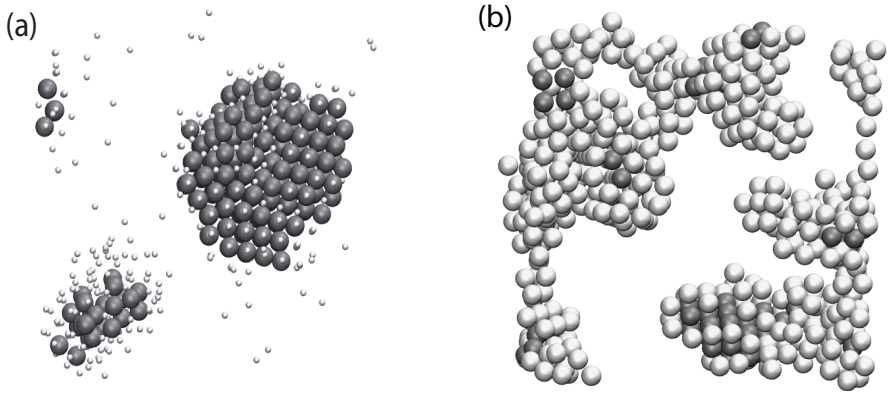

Figure 8.4: Simulation snapshots for colloid packing fraction η_c=0.10 at time $t/t_s = 21 \times 10^6$. Dark particles are crystalline, while light particles are fluid like. (a) η_p^r=0.34 (regime F). The diameter of the fluid particles is reduced by a factor 1/3. (b) η_p^r=0.60 (regime G). In (a) we observe the formation of clusters due to nucleation of the liquid phase in the gas phase. Subsequently, the fluid clusters nucleate the crystal phase. In (b) we observe the formation of clusters due to spinodal decomposition. The reversible clusters can break and merge, remain glassy and correspond to weak gelation.

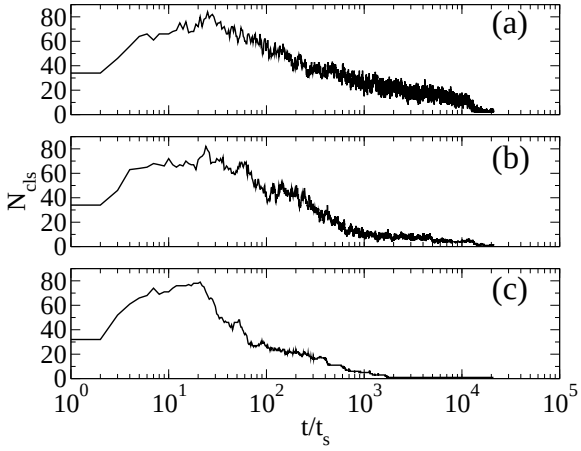

Figure 8.5: Number of clusters for colloid packing fraction η_c=0.10 as a function of time t/t_s, where $t_s = 10^3 \delta t$ is the sampling interval. (a) η_p^r=0.34. (b) η_p^r=0.38. (c) η_p^r=0.60. In (a) the cluster formation is due to nucleation of the liquid phase. The fluid clusters can aggregate or nucleate the crystal phase (kinetic pathway F). In (c) the cluster formation is due to spinodal decomposition (kinetic pathway G). The state point (b) is at the boundary between spinodal decomposition and nucleation.

line in Fig. 8.1) can be drawn in regime G that denotes the crossover from fluid of mobile clusters to a weak gel that consist of kinetically arrested clusters similar as the arrest of particles in a repulsive glass.

Figs. 8.6(b),(c) show the time evolution of the number of clusters in the system for interaction energies $\beta U \simeq 2.8$, and $\beta U \simeq 4.4$, respectively. The spinodal decomposition is arrested, resulting in a long-lived percolating cluster. For interaction energy $\beta U \simeq 2.8$ (η_p^r=0.38) crystallites can form in the system (Fig. 8.7(b)), while for $\beta U \simeq 4.4$ (η_p^r=0.6) the branches are glassy (Fig. 8.7(c)).

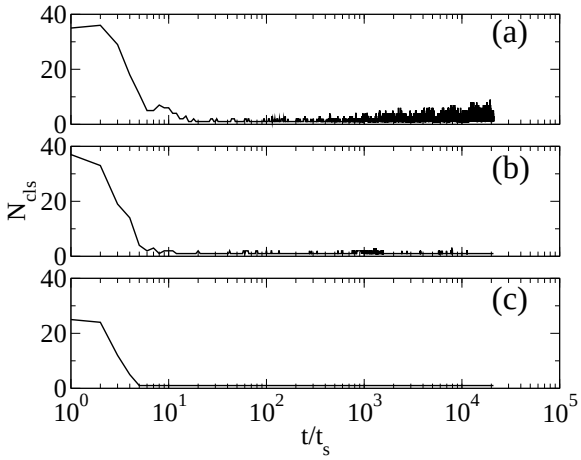

Figure 8.6: Number of clusters for colloid packing fraction η_c=0.25 (kinetic pathway G) as a function of time t/t_s, where $t_s = 10^3\delta t$ is the sampling interval. (a) η_p^r=0.32. (b) η_p^r=0.38. (c) η_p^r=0.60. In (a) we observe fluctuations in the number of clusters at high t/t_s, this indicates the presence of clusters in the system. While in (b),(c) a single cluster is formed at small t/t_s, and survives for the entire simulation time.

In regime L the initial homogeneous fluid can nucleate a gas or a crystal phase. We observe the formation of voids in the structure, but we are unable to discriminate between gas nucleation or particle crowding. In this region we observe that the branches crystallise (Fig. 8.8(a)) at low attraction energy, but remain glassy at higher attraction energy (Fig. 8.8(b)).

8.4 Conclusions

We studied the dynamical evolution of a phase separating system of hard spheres with short range attractive interactions. We find a well-defined region in the phase diagram where crystallites formed during the simulations. This region is limited at low attractions by a fluid phase (of clusters), and at high attractive interactions by a gel-like phase. The nucleation of crystallites is dramatically enhanced by the metastable gas-liquid phase separation.

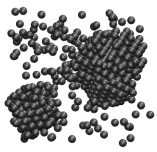

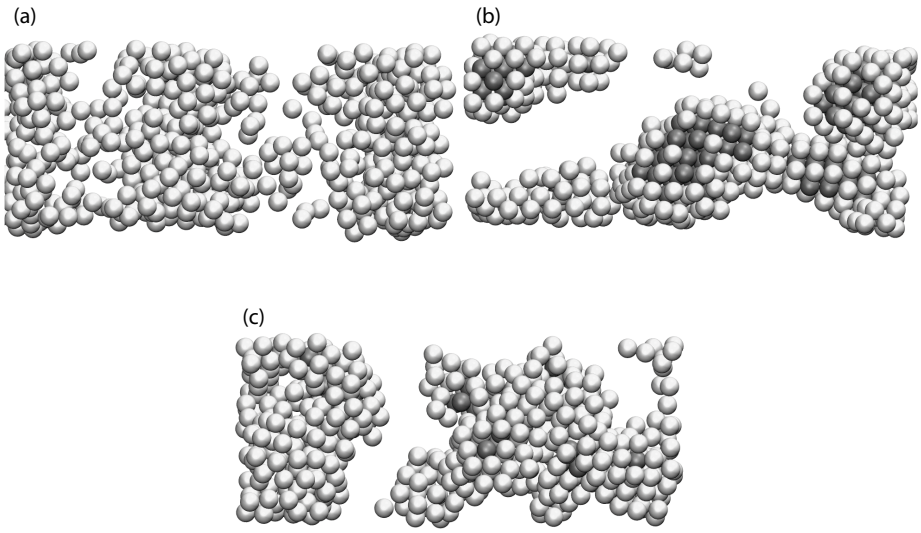

Figure 8.7: The same as Fig. 8.4, but for colloid packing fraction η_c=0.25 (regime G). (a) η_p^r=0.32. (b) η_p^r=0.38. (c) η_p^r=0.60. In (a) the structure is that of a fluid of crowding, reversible clusters, that can break and merge. In (b) and (c) we observe a single long-lived cluster that can be crystalline (b) or glassy (c).

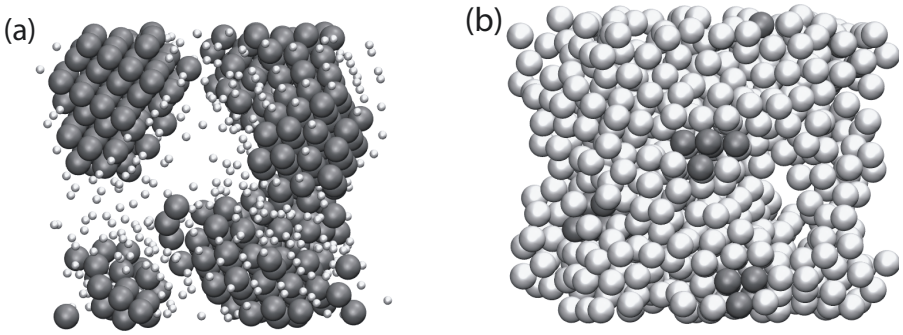

Figure 8.8: The same as Fig. 8.4, but for colloid packing fraction η_c=0.40 (regime L) and $t/t_s = 7\times10^3$. (a) η_p^r=0.34. (b) η_p^r=0.60. In (a) we observe the formation of voids and subsequently the nucleation of crystal structures in the fluid branches. In (b) we observe the formation of voids but the structure remains glassy, corresponding to a spatially homogeneous gel or attractive glass.

We studied the competition between gas-liquid phase separation and crystal nucleation. Upon quenching the system well-inside the metastable gas-liquid coexistence region we find the immediate formation of clusters. The clusters can be formed through spinodal decomposition, nucleation and growth or kinetic aggregation. The structure of the clusters can be crystal-like or glassy.

We can distinguish different regions in the phase diagram that partly coincide with kinetic regions. In regime F, we observe 'long-lived' compact clusters that are formed by nucleation and growth. These clusters are stable over the simulation time probably because they cannot adapt their shapes to allow coalescence on the Smoluchowski timescale. A fluid of clusters was recently observed by Lu et al. [227]. In regime G, we find the formation of an interconnected network of colloid-rich and colloid-poor regions, due to spinodal decomposition. At low packing fraction the network coarsens into long-lived non-equilibrium clusters that can merge and break-up again. At sufficiently high packing fraction these reversible clusters can get arrested due to crowding of clusters (type III gels in the notation of Cates et al. [196]) which is the 'weak gelation' as the particles bonding is reversible. The crossover from mobile fluid clusters to arrested clusters was observed experimentally by Segrè et al. [223].

At higher colloid packing fractions in regime G the spinodal decomposition is immediately arrested into a percolated network. The fluid branches can nucleate the crystal phase, and for higher attraction we observe glassy branches. These structures are type II gels in the notation of Cates et al. [196]. Type II gels are driven by spinodal decomposition into a percolating colloid-rich network that can get arrested at sufficiently high polymer reservoir packing fraction or interaction energy. The ageing of the crystal-like network can proceed very fast leading to a collapse of the branches, but can sometimes survive for the entire simulation time. The glass-like arrest of the spinodal decomposition was observed experimentally by Manley et al. [206].

In regime L we observe percolated structures with thick branches with crystal or glassy structure. These structure corresponds to type I gels in the notation of Cates et al. [196], which are spatially homogeneous gels at high colloid packing fraction and might be related to the attractive glass.

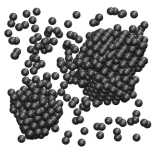

Bibliography

[1] J. Perrin, Ann. Chim. Phys **18**, 1 (1909).

[2] B. Alder and T. Wainwright, J. Chem. Phys. **27**, 1208 (1957).

[3] A. Van Helden, J. Jansen, and A. Vrij, J. Colloid Interface Sci. **81**, 354 (1981).

[4] P. N. Pusey and W. van Megen, Nature **320**, 340 (1986).

[5] M. E. Leunissen, C. G. Christova, A.-P. Hynninen, C. P. Royall, A. I. Campbell, A. Imhof, M. Dijkstra, R. van Roij, and A. van Blaaderen, Nature **437**, 235 (2005).

[6] V. de Villeneuve, R. Dullens, D. Aarts, E. Groeneveld, J. Scherff, W. Kegel, and H. Lekkerkerker, Science **309**, 1231 (2005).

[7] A. Moussaïd, W. C. K. Poon, P. N. Pusey, and M. F. Soliva, Phys. Rev. Lett. **82**, 225 (1999).

[8] W. C. K. Poon, J. Phys.: Condens. Matter **14**, R859 (2002).

[9] S. Auer and D.Frenkel, Nature **409**, 1020 (2001).

[10] U. Gasser, E. R. Weeks, A. Schofield, P. N. Pusey, and D. A. Weitz, Science **292**, 258 (2001).

[11] D. G. A. L. Aarts, M. Schmidt, and H. N. W. Lekkerkerker, Science **304**, 847 (2004).

[12] R. L. C. Vink, A. Jusufi, J. Dzubiella, and C. N. Likos, Phys. Rev. E **72**, 030401(R) (2005).

[13] W. K. Wijting, N. A. M. Besseling, and M. A. C. Stuart, Phys. Rev. Lett. **90**, 196101 (2003).

[14] M. Dijkstra and R. van Roij, Phys. Rev. Lett. **89**, 208303 (2002).

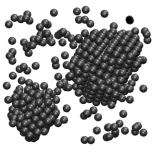

[15] M. P. Allen and D. J. Tildesley, *Computer Simulation of Liquids* (Oxford University Press, New York, 1987).

[16] D. C. Rapaport, *The art of molecular dynamics simulation* (Cambridge University Press, Cambridge, 1995).

[17] D. P. Landau and K. Binder, *A guide to Monte Carlo simulations in statistical physics* (Cambridge University Press, Cambridge, 2000).

[18] D. Frenkel and B. Smit, *Understanding Molecular Simulation 2nd edition*, vol. 1 of *Computational Science Series* (Academic Press, 2002).

[19] N. Metropolis, A. W. Rosenbluth, M. N. Rosenbluth, A. N. Teller, and E. Teller, J. Chem. Phys. **21**, 1087 (1953).

[20] P. G. Bolhuis, D. Frenkel, S.-C. Mau, and D. A. H. E. difference, Nature **388**, 236 (1997).

[21] S.-C. Mau and D. A. Huse, Phys. Rev. E **59**, 4396 (1999).

[22] C. Radin and L. Sadun, Phys. Rev. Lett. **94**, 015502 (2005).

[23] B. Derjaguin and L. Landau, Acta Physicochim. **14**, 633 (1941).

[24] E. Verwey and J. T. Overbeek, *Theory of the Stability of Lyophobic Colloids* (Elsevier, Amsterdam, 1948).

[25] S. Hamaguchi, R. T. Farouki, and D. H. E. Dubin, Phys. Rev. E **56**, 4671 (1997).

[26] A.-P. Hynninen and M. Dijkstra, Phys. Rev. E **68**, 021407 (2003).

[27] S. Asakura and F. Oosawa, J. Chem. Phys. **22**, 1255 (1954).

[28] A. Vrij, Pure Appl. Chem. **48**, 471 (1976).

[29] E. Meijer and D. Frenkel, Phys. Rev. Lett. **67**, 1110 (1991).

[30] H. N. W. Lekkerkerker, W. C. K. Poon, P. N. Pusey, A. Stroobants, and P. Warren, Europhys. Lett. **20**, 559 (1992).

[31] P. Sperry, H. Hopfenberg, and N. Thomas, J. Colloid Interface Sci. **82**, 62 (1981).

[32] A. Gast, C. Hall, and W. Russel, J. Colloid Interface Sci. **96**, 251 (1983).

[33] S. M. Ilett, A. Orrock, W. C. K. Poon, and P. N. Pusey, Phys. Rev. E **51**, 1344 (1995).

[34] R. Tuinier, D. Aarts, H. Wensink, and H. Lekkerkerker, Phys. Chem. Chem. Phys. **5**, 3707 (2003).

[35] E. J. Meijer and D. Frenkel, J. Chem. Phys. **100**, 6873 (1994).

[36] V. Y. Grinberg and V. B. Tolstoguzov, Food Hydrocolloids **11**, 145 (1997).

[37] J.-L. Doublier, C. Garnier, C. Renard, and C. Sanchez, Curr. Opin. Colloid Interface Sci. **5**, 184 (2000).

[38] S. Asakura and F. Oosawa, J. Pol. Sci. **33**, 183 (1958).

[39] H. De Hek and A. Vrij, J. Colloid Interface Sci. **84**, 409 (1981).

[40] M. Dijkstra, R. van Roij, and R. Evans, Phys. Rev. Lett. **81**, 2268 (1998).

[41] M. Dijkstra, R. van Roij, and R. Evans, Phys. Rev. Lett. **82**, 117 (1999).

[42] M. Dijkstra, R. van Roij, and R. Evans, Phys. Rev. E **59**, 5744 (1999).

[43] M. Dijkstra, J. M. Brader, and R. Evans, J. Phys.: Condens. Matter **11**, 10079 (1999).

[44] J.-P. Hansen and I. McDonald, *Theory of Simple Liquids* (Academic Press, San Diego, CA, USA, 1986).

[45] M. Heni and H. Löwen, Phys. Rev. E **60**, 7057 (1999).

[46] M. Schmidt, H. Löwen, J. M. Brader, and R. Evans, Phys. Rev. Lett. **85**, 1934 (2000).

[47] P. P. F. Wessels, M. Schmidt, and H. Löwen, J. Phys.: Condens. Matter **16**, L1 (2004).

[48] Y. Rosenfeld, Phys. Rev. Lett. **63**, 980 (1989).

[49] P. P. F. Wessels, M. Schmidt, and H. Löwen, J. Phys.: Condens. Matter **16**, S4169 (2004).

[50] R. Evans and U. M. B. Marconi, J. Chem. Phys. **86**, 7138 (1987).

[51] M. Dijkstra, J. Chem. Phys. **107**, 3277 (1997).

[52] J. S. Rowlinson and B. Widom, *Molecular Theory of Capillarity* (Dover, New York, 2002).

[53] H. Reiss, H. L. Frisch, and J. L. Lebowitz, J. Chem. Phys. **31**, 369 (1959).

[54] H. Reiss, H. L. Frisch, E. Helfand, and J. L. Lebowitz, J. Chem. Phys. **32**, 119 (1960).

[55] J. R. Henderson and F. van Swol, Mol. Phys. **51**, 991 (1984).

[56] R. Roth and S. Dietrich, Phys. Rev. E **62**, 6926 (2000).

[57] M. Dijkstra, Phys. Rev. Lett. **93**, 108303 (2004).

[58] R. Roth and R. Evans, private communication (2004).

[59] J. M. Brader, R. Evans, and M. Schmidt, Mol. Phys. **101**, 3349 (2003).

[60] W. Hoover and F. Ree, J. Chem. Phys. **49**, 3609 (1968).

[61] P. Pieranski, L. Strzelecki, and B. Pansu, Phys. Rev. Lett. **50**, 900 (1983).

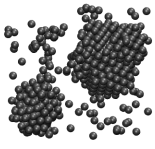

[62] J. A. Weiss, D. W. Oxtoby, D. G. Grier, and C. A. Murray, J. Chem. Phys. **103**, 1180 (1995).

[63] S. Neser, C. Bechinger, T. Palberg, and P. Leiderer, Phys. Rev. Lett. **79**, 2348 (1997).

[64] A. B. Fontecha, H. J. Schöpe, H. König, T. Palberg, R. Messina, and H. Löwen, J. Phys.: Condens. Matter **17**, s2779 (2005).

[65] I. Cohen, T. G. Mason, and D. A. Weitz, Phys. Rev. Lett. **93** (2004).

[66] M. Schmidt and H. Löwen, Phys. Rev. Lett. **76**, 4552 (1996).

[67] R. Zangi and S. A. Rice, Phys. Rev. E **61**, 671 (2000).

[68] R. Messina and H. Löwen, Phys. Rev. Lett. **91**, 146101 (2003).

[69] J. Klein and E. Kumacheva, Science **269**, 816 (1995).

[70] J. Gao, W. D. Luedtke, and U. Landman, Phys. Rev. Lett. **79**, 705 (1997).

[71] C. Ghatak and K. G. Ayappa, Phys. Rev. E **64**, 051507 (2001).

[72] A. Ciach, Prog. Colloid Polym. Sci. **129**, 40 (2004).

[73] J. H. Conway and N. J. A. Sloane, *Sphere Packings, Lattices and Groups* (Springer, New York, 1993).

[74] T. Aste and D. Weaire, *The Pursuit of Perfect Packing* (IOP, Bristol, 2000).

[75] R. L. Davidchack and B. B. Laird, J. Chem. Phys. **108**, 9452 (1998).

[76] D. Chaudhuri and S. Sengupta, Phys. Rev. Lett. **93**, 115702 (2004).

[77] L. D. Gelb, K. E. Gubbins, R. Radhakrishnan, and M. Sliwinska-Bartkowiac, Rep. Prog. Phys. **62**, 1573 (1999).

[78] R. Evans, J. Phys.: Condens. Matter **2**, 8989 (1990).

[79] M. Dijkstra and R. van Roij, J. Phys.: Condens. Matter **17**, S3507 (2005).

[80] M. Dijkstra, R. van Roij, R. Roth, and A. Fortini, Phys. Rev. E **73**, 041404 (2006).

[81] J. M. Brader, R. Evans, M. Schmidt, and H. Löwen, J. Phys.: Condens. Matter **14**, L1 (2002).

[82] D. G. A. L. Aarts, J. H. van der Wiel, and H. N. W. Lekkerker, J. Phys.: Condens. Matter **15**, S245 (2003).

[83] D. G. A. L. Aarts and H. N. W. Lekkerker, J. Phys.: Condens. Matter **16**, S4231 (2004).

[84] W. K. Wijting, N. A. M. Besseling, and M. A. C. Stuart, J. Phys. Chem. B **107**, 10565 (2003).

[85] P. Jenkins and M. Snowden, Adv. Coll. Interf. Sci. **68**, 57 (1996).

[86] P. P. F. Wessels, M. Schmidt, and H. Löwen, Phys. Rev. Lett. **94**, 078303 (2005).

[87] M. Schmidt, E. Schöll-Paschinger, J. Köfinger, and G. Kahl, J. Phys.: Condens. Matter **14**, 12099 (2002).

[88] P. P. F. Wessels, M. Schmidt, and H. Löwen, Phys. Rev. E **68**, 061404 (2003).

[89] I. O. Götze, J. M. Brader, M. Schmidt, and H. Löwen, Mol. Phys. **101**, 1651 (2003).

[90] A. Z. Panagiotopoulos, Mol. Phys. **61**, 813 (1987).

[91] A. Z. Panagiotopoulos, Mol. Phys. **62**, 701 (1987).

[92] B. Smit and D. Frenkel, Mol. Phys. **68**, 951 (1989).

[93] R. L. C. Vink and J. Horbach, J. Phys.: Condens. Matter **16**, S3807 (2004).

[94] R. L. C. Vink, K. Binder, and J. Horbach, Phys. Rev. E **73**, 056118 (2006).

[95] J.-T. Lee and M. Robert, Phys. Rev. E **60**, 7198 (1999).

[96] M. Schmidt, H. Löwen, J. M. Brader, and R. Evans, J. Phys.: Condens. Matter **14**, 9353 (2002).

[97] T.-C. Lee, J.-T. Lee, D. Pilaski, and M. Robert, Physica A **329**, 411 (2003).

[98] J. M. Brader and R. Evans, Europhys. Lett. **49**, 678 (2000).

[99] M. Schmidt, A. Fortini, and M. Dijkstra, J. Phys.: Condens. Matter **15**, 3411 (2003).

[100] P. Bolhuis, A. A. Louis, and J.-P. Hansen, Phys. Rev. Lett. **89**, 128302 (2002).

[101] P. G. Bolhuis and A. A. Louis, Macromolecules **35**, 1860 (2002).

[102] E. H. A. de Hoog and H. N. W. Lekkerkerker, J. Phys. Chem. B **103** (1999).

[103] B.-H. Chen, B. Payandeh, and M. Robert, Phys. Rev. E **62**, 2369 (2000).

[104] R. L. C. Vink and J. Horbach, J. Chem. Phys. **121**, 3253 (2004).

[105] J. M. Brader, M. Dijkstra, and R. Evans, Phys. Rev. E **63**, 041405 (2001).

[106] D. G. A. L. Aarts, J. Phys. Chem. B **109**, 7407 (2005).

[107] A. Fortini, M. Dijkstra, M. Schmidt, and P. P. F. Wessels, Phys. Rev. E **71**, 051403 (2005).

[108] M. Schmidt, A. Fortini, and M. Dijkstra, J. Phys.: Condens. Matter **16**, S4159 (2004).

[109] A. Fortini, M. Schmidt, and M. Dijkstra, Phys. Rev. E **73**, 051502 (2006).

[110] R. L. C. Vink, A. D. Virgiliis, J. Horbach, and K. Binder, Phys. Rev. E **74**, 031601 (2006).

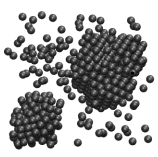

[111] M. Schmidt and A. R. Denton, Phys. Rev. E **65**, 061410 (2002).

[112] A. R. Denton and M. Schmidt, J. Phys.: Condens. Matter **14**, 12051 (2002).

[113] A. R. Denton and M. Schmidt, J. Chem. Phys. **122**, 244911 (2005).

[114] A. Fortini, M. Dijkstra, and R. Tuinier, J. Phys.: Condens. Matter **17**, 7783 (2005).

[115] M. Schmidt, A. R. Denton, and J. M. Brader, J. Chem. Phys. **118**, 1541 (2003).

[116] R. L. C. Vink and M. Schmidt, Phys. Rev. E **71**, 051406 (2005).

[117] M. Schmidt, M. Dijkstra, and J.-P. Hansen, Phys. Rev. Lett. **93**, 088303 (2004).

[118] D. G. A. L. Aarts, R. Tuinier, and H. N. W. Lekkerkerker, J. Phys: Condens. Matter **14**, 7551 (2002).

[119] A. Moncho-Jorda, B. Rotenberg, and A. A. Louis, J. Chem. Phys. **119**, 12667 (2003).

[120] D. G. A. L. Aarts, R. P. A. Dullens, H. N. W. Lekkerker, D. Bonn, and R. van Roij, J. Chem. Phys. **120**, 1973 (2004).

[121] A. Jusufi, J. Dzubiella, C. N. Likos, C. von Ferber, and H. Löwen, J. Phys.: Condens. Matter **13**, 6177 (2001).

[122] J. Dzubiella, C. N. Likos, and H. Löwen, J. Chem. Phys. **116**, 9518 (2002).

[123] R. Rotenberg, J. Dzubiella, A. A. Louis, and J.-P. Hansen, Mol. Phys. **102**, 1 (2004).

[124] R. L. C. Vink, A. Jusufi, J. Dzubiella, and C. N. Likos, Phys. Rev. E **72**, 030401(R) (2005).

[125] A. Moncho-Jorda, J. Dzubiella, J.-P. Hansen, and A. A. Louis, J. Phys. Chem. B **109**, 6640 (2005).

[126] P. Virnau and M. Müller, J. Chem. Phys. **120**, 10925 (2004).

[127] K. Binder, Phys. Rev. A **25**, 1699 (1982).

[128] H. N. W. Lekkerkerker, Colloids and Surfaces **51**, 419 (1990).

[129] W. K. Wijting, W. Knoben, N. A. M. Besseling, F. A. M. Leermakers, and M. A. C. Stuart, Phys. Chem. Chem Phys. **6**, 4432 (2004).

[130] T. Hebert, Phytopathology **53**, 362 (1963).

[131] S. Finet and A. Tardieu, J. Crystal Growth **232**, 40 (2001).

[132] M. Casselyn, J. Perez, A. Tardieu, P. Vachette, J. Witz, and H. Delacroix, Acta Cryst. D **57**, 1799 (2001).

[133] P. Patel and W. Russel, J. Colloid Interface Sci. **131**, 192 (1989).

[134] O. Annunziata, N. Asherie, A. Lomakin, J. Pande, O. Ogun, and G. Benedek, PNAS **99**, 14165 (2002).

[135] P. Ferreira, M. Dymitrowska, and L. Belloni, J. Chem. Phys. **113**, 9849 (2000).

[136] H. Graf and H. Löwen, Phys. Rev. E **57**, 5744 (1998).

[137] A. R. Denton, Phys. Rev. E **62**, 3855 (2000).

[138] P. Warren, J. Chem. Phys. **112**, 4683 (2000).

[139] L. Belloni, J. Phys.: Condens. Matter **12**, R549 (2000).

[140] M. Dijkstra and R. van Roij, J. Phys.: Condens. Matter **10**, 1219 (1998).

[141] F. Donnan and A. Harris, J. Chem. Soc. **99**, 1554 (1911).

[142] F. Donnan, Z. Electrochem. **17**, 572 (1911).

[143] F. Donnan, Chem. Rev. **1**, 73 (1924).

[144] N. F. Carnahan and K. E. Starling, J. Chem. Phys. **51**, 635 (1969).

[145] C. Hall, J. Chem. Phys. **52**, 2252 (1972).

[146] D. Frenkel and A. Ladd, J. Chem. Phys. **81**, 3188 (1984).

[147] J. M. Polson, E. Trizac, S. Pronk, and D. Frenkel, J. Chem. Phys. **112**, 5339 (2000).

[148] J. Barker and D. Henderson, J. Chem. Phys. **47**, 4714 (1967).

[149] A. Louis and R. Roth, J. Phys: Condens. Matter **13**, L777 (2001).

[150] J. Lebowitz, E. Helfand, and E. Praestgaard, J. Chem. Phys. **43**, 774 (1965).

[151] B. Widom, Science **157**, 375 (1967).

[152] W. Wood and J. Jacobson, J. Chem. Phys. **27**, 1207 (1957).

[153] M. Robbins, K. Kremer, and G. Grest, J. Chem. Phys. **88**, 3286 (1993).

[154] E. J. Meijer and F. E. Azhar, J. Chem. Phys. **106**, 4678 (1997).

[155] F. E. Azhar, M. Baus, J. P. Ryckaert, and E. J. Meijer, J. Chem. Phys. **112**, 5121 (2000).

[156] G. Orkoulas and A. Z. Panagiotopoulos, J. Chem. Phys. **101**, 1452 (1994).

[157] C. Vega, F. Bresme, and J. L. Abascal, Phys. Rev. E **54**, 2746 (1996).

[158] B. Smit, K. Esselink, and D. Frenkel, Mol. Phys. **87**, 159 (1996).

[159] F. Bresme, C. Vega, and J. L. F. Abascal, Phys. Rev. Lett. **85**, 3217 (2000).

[160] J. L. F. Abascal, C. Vega, C. McBride, and F. Bresme, Phys. Rev. E **68**, 052501 (2003).

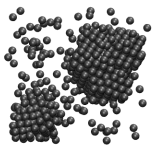

[161] C. Vega, J. L. F. Abascal, and C. McBride, J. Chem. Phys. **119**, 964 (2003).

[162] Y. V. Kalyuzhnyi, G. Kahl, and P. T. Cummings, J. Chem. Phys. **123**, 124501 (2005).

[163] M. E. Fisher, J.-N. Aqua, and S. Banerjee, Phys. Rev. Lett. **95**, 135701 (2005).

[164] A.-P. Hynninen, M. E. Leunissen, A. van Blaaderen, and M. Dijkstra, Phys. Rev. Lett. **96**, 018303 (2006).

[165] J. B. Caballero, A. M. Puertas, A. Fernández-Barbero, and F. J. de las Nieves, J. Chem. Phys. **121**, 2428 (2004).

[166] J. B. Caballero, A. M. Puertas, A. Fernández-Barbero, F. J. de las Nieves, J. Romero-Enrique, and L. Rull, J. Chem. Phys. **124**, 054909 (2006).

[167] J. B. Caballero and A. Puertas, Preprint (cond-matt/0511666).

[168] P. Bartlett and A. I. Campbell, Phys. Rev. Lett. **95**, 128302 (2005).

[169] A.-P. Hynninen, C. G. Christova, R. van Roij, A. van Blaaderen, and M. Dijkstra, Phys. Rev. Lett. **96**, 138308 (2006).

[170] R. J. F. L. de Carvalho and R. Evans, Mol. Phys. **92**, 211 (1997).

[171] R. van Roij, M. Dijkstra, and J.-P. Hansen, Phys. Rev. E **59**, 2010 (1999).

[172] B. Zoetekouw and R. van Roij, Phys. Rev. E **73**, 021403 (2006).

[173] A.-P. Hynninen and M. Dijkstra, J. Chem. Phys. **123**, 244902 (2005).

[174] G. M. Bell, S. Levine, and L. N. McCartney, J. Colloid. Interface Sci. **33**, 335 (1970).

[175] G. R. Maskaly, Ph.D. thesis, MIT, Boston (2005).

[176] A.-P. Hynninen, Ph.D. thesis, Utrecht University, Utrecht (2005).

[177] A. M. Ferrenberg and R. H. Swendsen, Phys. Rev. Lett. **61**, 2635 (1988).

[178] J. J. Potoff and A. Z. Panagiotopoulos, J. Chem. Phys. **112**, 6411 (2000).

[179] R. L. C. Vink, J. Horbach, and K. Binder, Phys. Rev. E **71**, 011401 (2005).

[180] M. H. J. Hagen and D. Frenkel, J. Chem. Phys. **101**, 4093 (1994).

[181] P. Bolhuis and D. Frenkel, J. Chem. Phys. **101**, 9869 (1994).

[182] C. F. Tejero, A. Daanoun, H. N. W. Lekkerkerker, and M. Baus, Phys. Rev. Lett. **73**, 752 (1994).

[183] C. F. Tejero, A. Daanoun, H. N. W. Lekkerkerker, and M. Baus, Phys. Rev. E **51**, 558 (1995).

[184] A. Daanoun, C. F. Tejero, and M. Baus, Phys. Rev. E **50**, 2913 (1994).

[185] C. Caccamo, G. Pellicane, D. Costa, D. Pini, and G. Stell, Phys. Rev. E **60**, 5533 (1999).

[186] M. Dijkstra, Phys. Rev. E **66**, 021402 (2002).

[187] G. Orkoulas and A. Z. Panagiotopoulos, J. Chem. Phys. **110**, 1581 (1999).

[188] M. González-Melchor, J. Alejandre, and F. Bresme, Phys. Rev. Lett. **90**, 135506 (2003).

[189] J. H. Chen, M. E. Fisher, and B. G. Nickel, Phys. Rev. Lett. **48**, 630 (1982).

[190] A. M. Ferrenberg and R. H. Swendsen, Phys. Rev. B **44**, 5081 (1991).

[191] A.-P. Hynninen, M. Dijkstra, and A. Z. Panagiotopoulos, J. Chem. Phys. **123**, 084903 (2005).

[192] G. R. Maskaly, R. E. Garcia, W. C. Carter, and Y.-M. Chiang, Phys. Rev. E **73**, 011402 (2006).

[193] B. Larsen and S. A. Rogde, J. Chem. Phys. **72**, 2578 (1980).

[194] A. P. Copestake and R. Evans, J. Phys. C: Solid State Phys. **15**, 4961 (1982).

[195] R. M. L. Evans, W. C. K. Poon, and F. Renth, Phys. Rev. E **64**, 031403 (2001).

[196] M. E. Cates, M. Fuchs, K. Kroy, W. C. K. Poon, and A. M. Puertas, J. Phys.: Condens. Matter **16**, S4861 (2004).

[197] E. R. Weeks, J. C. Crocker, A. C. Levitt, A. Schofield, and D. A. Weitz, Science **287**, 627 (2000).

[198] W. K. Kegel and A. van Blaaderen, Science **287**, 290 (2000).

[199] K. N. Pham, A. M. Puertas, J. Bergenholtz, S. U. Egelhaaf, A. Moussaïd, P. N. Pusey, A. B. Schofield, M. E. Cates, M. Fuchs, and W. C. K. Poon, Science **296**, 104 (2002).

[200] M. T. A. Bos and J. H. J. van Opheusden, Phys. Rev. E **53**, 5044 (1996).

[201] N. A. M. Verhaegh, D. Asnaghi, and H. Lekkerkerker, Physica A **264**, 64 (1999).

[202] E. H. A. de Hoog, W. K. Kegel, A. van Blaaderen, and H. N. W. Lekkerkerker, Phys. Rev. E **64**, 021407 (2001).

[203] V. J. Anderson, E. H. A. de Hoog, and H. N. W. Lekkerkerker, Phys. Rev. E **65**, 011403 (2001).

[204] J. Bergenholtz, W. C. K. Poon, and M. Fuchs, Langmuir **19**, 4493 (2003).

[205] H. Sedgwick, K. Kroy, A. Salonen, M. Robertson, S. Egelhaaf, and W. Poon, Eur. Phys. J. E **16**, 77 (2005).

[206] S. Manley, H. M. Wyss, K. Miyazaki, J. C. Conrad, V. Trappe, L. J. Kaufman, D. R. Reichman, and D. A. Weitz, Phys. Rev. Lett. **95** (2005).

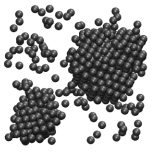

[207] E. Zaccarelli, I. Saika-Voivod, S. V. Buldyrev, A. J. Moreno, P. Tartaglia, and F. Sciortino, J. Chem. Phys. **124**, 124908 (2006).

[208] V. J. Anderson and H. N. W. Lekkerkerker, Nature **416**, 811 (2002).

[209] J. Zhu, M. Li, R. Rogers, W. Meyer, R. Ottewill, S.-. S. S. Crew, W. B. Russel, and P. M. Chaikin, Nature **387**, 883 (1997).

[210] P. N. Pusey and W. van Megen, Phys. Rev. A **43**, 5429 (1991).

[211] W. Götze and L. Sjörgren, Phys. Rev. A **43**, 5442 (1991).

[212] W. Götze and L. Sjörgren, Rep. Prog. Phys. **55**, 241 (1992).

[213] W. van Megen and S. M. Underwood, Phys. Rev. E **49**, 4206 (1994).

[214] G. Foffi, C. D. Michele, F. Sciortino, and P. Tartaglia, Phys. Rev. Lett. **94**, 078301 (2005).

[215] S. S. Ashwin, G. I. Menon, and S. Sastry, Europhys. Lett. **75**, 922 (2006).

[216] F. Sciortino, S. V. Buldyrev, C. D. Michele, G. Foffi, N. Ghofraniha, E. L. Nave, A. Moreno, S. Mossa, I. Saika-Voivod, P. Tartaglia, et al., Computer Physics Communications **169**, 166 (2005).

[217] S. Babu, M. Rotterau, T. Nicolai, J. C. Gimel, and D. Durand, Eur. Phys. J. E **19**, 203 (2006).

[218] E. Elfimova, A. O. Ivanov, and A. Y. Zubarev, Phys. Rev. E **74**, 021408 (2006).

[219] K. G. Soga, J. R. Melrose, and R. C. Ball, J. Chem. Phys. **108**, 6026 (1998).

[220] K. G. Soga, J. R. Melrose, and R. C. Ball, J. Chem. Phys. **110**, 2280 (1999).

[221] J. J. Cerdá, T. Sintes, C. M. Sorensen, and A. Chakrabarti, Phys. Rev. E **70**, 011405 (2004).

[222] G. Foffi, C. D. Michele, F. Sciortino, and P. Tartaglia, J. Chem. Phys. **122**, 224903 (2005).

[223] P. N. Segrè, V. Prasad, A. B. Schofield, and D. A. Weitz, Phys. Rev. Lett. **86**, 6042 (2001).

[224] A. Stradner, H. Sedgwick, F. Cardinaux, W. C. K. Poon, S. U. Egelhaaf, and P. Schurtenberger, Nature **432** (2004).

[225] K. Kroy, M. E. Cates, and W. C. K. Poon, Phys. Rev. Lett. **92**, 148302 (2004).

[226] A. Coniglio, L. de Arcangelis, A. de Candia, E. D. Gado, A. Fierro, and N. Sator, J. Phys: Condens. Matter **18**, S2383 (2006).

[227] P. J. Lu, J. C. Conrad, H. M. Wyss, A. B. Schofield, and D. A. Weitz, Phys. Rev. Lett. **96**, 028306 (2006).

[228] A. I. Campbell, V. J. Anderson, J. S. van Duijneveldt, and P. Bartlett, Phys. Rev. Lett. **94**, 208301 (2005).

[229] J. Groenewold and W. Kegel, J. Phys. Chem. B **105**, 11702 (2001).

[230] A. M. Puertas, M. Fuchs, and M. E. Cates, cond-matt/0603666 (2006).

[231] E. Zaccarelli, S. V. Buldyrev, E. L. Nave, A. J. Moreno, I. Saika-Voivod, F. Sciortino, and P. Tartaglia, Phys. Rev. Lett. **94**, 218301 (2005).

[232] W. C. K. Poon, F. Renth, and R. M. L. Evans, J. Phys: Condens. Matter **12**, A269 (2000).

[233] R. Hall, J. Chem. Phys. **57** (1972).

[234] P. R. ten Wolde, M. J. Ruiz-Montero, and D. Frenkel, Phys. Rev. Lett. **75**, 2714 (1995).

[235] M. A. Miller and D. Frenkel, J. Phys.: Condens. Matter **16**, S4901 (2004).

[236] J. W. Cahn, J. Am. Ceram. Soc. **52**, 118 (1969).

[237] A. M. Puertas, M. Fuchs, and M. E. Cates, J. Phys. Chem. B **109**, 6666 (2005).

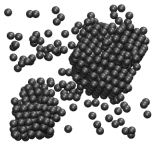

Summary

In this thesis, we have presented computer simulation results on the bulk and interfacial phase behaviour of colloidal suspensions. In the first part, consisting of chapters 2, 3, 4, and 5, we have studied inhomogeneous systems. In particular, in chapter 2 we have developed and tested a simulation technique to calculate the free energy of hard-core systems. This technique was used to calculate the interfacial free energy of colloidal hard spheres and with the addition of non-adsorbing polymer coils. Good agreement was found between the simulation results and those from density functional theory. On the other hand, qualitative agreement was found between simulations and scaled particle theory. In chapter 3 we have determined the equilibrium phases of a system of hard spheres confined between two parallel hard walls for plate separations from one to five hard-sphere diameters. We found a fluid-solid transition, which corresponded to either capillary freezing or melting depending on the plate separation. The coexisting solid phase consisted of crystalline layers with either triangular or square symmetry. At high densities, intermediate structures, e.g., prism, buckled, and rhombic phases, were found. In chapter 4, we have analysed colloid-polymer mixtures confined between two parallel plates. Colloids were described as hard spheres, while polymers were described as overlapping spheres and are excluded from the colloidal surfaces by a hard-core diameter. We have considered different types of confinement, namely either through two hard walls or through two semi-permeable walls that repel colloids but allowed polymers to freely penetrate. For hard walls we found capillary condensation, while for semi-permeable walls we found capillary evaporation. For hard walls the density profiles of polymers and colloids inside the slit displayed oscillations due to packing effects for all statepoints. For semi-permeable walls either similar structuring or flat density profiles were found, depending on the statepoint considered. In chapter 5, we have analysed a model of colloid-polymer mixtures with interacting polymers. We found that the number of polymers needed to drive the demixing transition is larger for the interacting polymers, and the gas-liquid interfacial tension is smaller. When the system was confined between two hard parallel plates we

found capillary condensation. This effect was slightly suppressed by the interactions between the polymers.

In the second part of the thesis, consisting of chapters 6, 7, and 8, we have analysed the bulk behaviour of colloidal suspensions. In chapter 6, we have studied the stability of mixtures of highly screened repulsive charged spheres and non-adsorbing ideal polymer chains. We found that the screened-Coulomb repulsion counteracts the effect of the effective polymer-mediated attraction. For mixtures of small polymers and relatively large charged colloidal spheres, the fluid-crystal transition shifted to significantly larger polymer concentrations with increasing range of the screened-Coulomb repulsion. For relatively large polymers, the effect of the screened-Coulomb repulsion was found to be weaker. The resulting fluid-fluid binodal was only slightly shifted towards larger polymer concentrations upon increasing the range of the screened-Coulomb repulsion. In chapter 7, we have studied the phase behaviour and the interfacial tension of the screened Coulomb (Yukawa) restricted primitive model (YRPM) of oppositely charged hard spheres. We found the gas-liquid phase separation to be stable for $\kappa\sigma \leq 4$. The critical temperature decreased upon increasing the screening of the interaction (decreasing the range of the interaction), while the interfacial tension decreased upon increasing the range of the interaction. In chapter 8, we have studied a mixture of monodisperse colloidal hard spheres and ideal polymers described by an effective one-component system. The equilibrium phase diagram was divided in different kinetic regimes. We carried out Brownian dynamics simulations to study the dynamic evolution of the different kinetic pathways. We found a fluid of 'long-lived' clusters in the binodal regime at low colloid packing fractions. In the spinodal regime, we observed at low colloid packing fractions a phase of crowded clusters that could merge and break-up again, and a kinetic arrested spinodal decomposition at higher packing fractions. At even higher colloid densities, a homogeneous gel phase was observed. The structure of the clusters were crystal-like at low attractive interactions and glassy at high attraction strengths.

Samenvatting

In dit proefschrift bestuderen we met behulp van computer simulaties het fasegedrag van colloïdale suspensies in bulk en begrensde geometrieën. In het eerste deel bestaande uit de hoofdstukken 2, 3, 4 en 5, hebben we inhomogene systemen bestudeerd. In het bijzonder hebben we in hoofdstuk 2 een simulatietechniek ontwikkeld om de grensvlakspanning te berekenen van harde bollen met niet-adsorberende polymeren tegen een harde wand. We hebben goede overeenkomst gevonden tussen de simulaties en dichtheidsfunctionaaltheorie en kwalitatieve overeenkomst met geschaalde deeltjestheorie. In hoofdstuk 3 hebben we de evenwichtsfases van een systeem van harde bollen tussen twee parallelle harde wanden bepaald voor plaatafstanden variërend van een tot vijf deeltjesdiameters. We hebben een vloeistof–vaste-stoffaseovergang gevonden, wat overeenkomt, afhankelijk van de afstand tussen de platen, met capillair bevriezen of capillair smelten. De coëxisterende vaste-stoffase bestaat uit kristallijne lagen met een driehoekige of een vierkante symmetrie. Bij hogere dichtheden werden tussenstructuren gevormd, bijvoorbeeld prisma's, scheefgetrokken en rhombische fases. In hoofdstuk 4 hebben we het fasegedrag van colloïd-polymeer mengsels tussen twee platen bestudeerd. We hebben de colloïden beschreven als harde bollen, terwijl de polymeren beschreven worden als bollen die wèl met elkaar maar niet met de colloïden mogen overlappen. We hebben zowel het effect van harde wanden als dat van semi-permeabele wanden onderzocht. De semipermeabele wanden laten wel de polymeren door, maar niet de colloïden. In het geval van harde wanden vinden we capillaire condensatie, terwijl we capillaire evaporatie vinden bij polymeer doorlatende wanden. In het geval van harde wanden vinden we oscillaties in de dichtheidsprofielen van de colloïden en de polymeren als gevolg van pakkingseffecten. Bij semi-permeabele wanden vinden we òf oscillerende òf vlakke dichtheidsprofielen, afhankelijk van het precieze fase punt. In hoofdstuk 5 hebben we mengsels van colloïden met interagerende polymeren bestudeerd. We vinden dat voor interagerende polymeren veel hogere polymeerconcentraties nodig zijn om een gas-vloeistof evenwicht te induceren dan voor ideale polymeren en dat de daarbij behorende gas-vloeistof grensvlakspan-

ning veel lager is. Wanneer we dit systeem tussen twee harde wanden plaatsen vinden we capillaire condensatie. Dit effect is echter zwakker door de interacties tussen de polymeren.

In het tweede deel van het proefschrift bestaande uit hoofdstukken 6, 7, en 8, hebben we het bulkgedrag van colloïdale suspensies geanalyseerd. In hoofdstuk 6, hebben we de stabiliteit bestudeerd van mengsels van sterk afgeschermd repulsief geladen bollen en niet-adsorberende ideale polymeer ketens. We hebben gevonden dat de afgeschermde Coulomb repulsie het effect van de effectieve polymeergeïnduceerde attracties tegenwerkt. Voor mengsels van kleine polymeren en relatief grote geladen colloïdale bollen verschuift de vloeistof-kristal overgang naar significant hogere polymeer concentraties wanneer het bereik van de afgeschermde Coulomb repulsie groter wordt. Voor relatief grote polymeren vinden we dat het effect van de afgeschermde Coulomb (Yukawa) repulsie zwakker is. De resulterende gas-vloeistof binodaal verschuift naar iets hogere polymeer concentraties wanneer het bereik van de afgeschermde Coulomb repulsie groter wordt. In hoofdstuk 7, hebben we het fasegedrag en de oppervlaktespanning bestudeerd van het Yukawa beperkte primitieve model (YRPM) van tegengesteld geladen harde bollen. We vinden dat de gas-vloeistoffasescheiding stabiel is voor $\kappa\sigma \leq 4$. De waarde van de kritische temperatuur neemt af bij toenemende afscherming van de wisselwerking (afnemende dracht van de wisselwerking), terwijl de oppervlaktespanning juist afneemt bij toenemende dracht van de wisselwerking. In hoofdstuk 8 hebben we een mengsel van monodisperse colloïdale harde bollen en ideale polymeren bestudeerd in een effectief een-component systeem. Het evenwichtsfasediagram wordt opgedeeld in verschillende kinetische regimes. We hebben Brownse dynamica simulaties uitgevoerd om de verschillende kinetische paden te bestuderen. In het binodale regime, bij lage volumefracties aan colloïden, ontdekten we een vloeistof bestaande uit langlevende clusters. In het spinodale regime, wederom bij lage volumefracties aan colloïden, vinden we dicht op elkaar gepakte clusters, die kunnen samenvloeien en weer kunnen opbreken. Daarnaast vinden we in het spinodale regime, ditmaal bij iets hogere volumefracties aan colloïden, een kinetisch bevroren spinodale ontmenging. Bij nog hogere dichtheden aan colloïden wordt een homogene gelachtige toestand waargenomen. De structuur van de clusters is kristallijn bij zwakke attracties tussen de colloïden en glasachtig bij sterke aantrekkingskrachten.

Publications

This thesis is based on the following publications:

1. A. FORTINI, M. SCHMIDT, AND M. DIJKSTRA, *Phase behavior and structure of model colloid-polymer mixtures confined between two parallel planar walls*, Phys. Rev. E, 73 (2006), p. 051502.

2. A. FORTINI, A.-P. HYNNINEN, AND M. DIJKSTRA, *Gas-liquid phase separation in oppositely charged colloids: Stability and interfacial tension*, J. Chem. Phys., 125 (2006), p. 094502.

3. A. FORTINI AND M. DIJKSTRA, *Phase behaviour of hard spheres confined between parallel hard plates: manipulation of colloidal crystal structures by confinement*, J. Phys.: Condens. Matter, 18 (2006), p. L371.

4. A. FORTINI, M. DIJKSTRA, AND R. TUINIER, *Phase behaviour of charged colloidal sphere dispersions with added polymer chains*, J. Phys.: Condens. Matter, 17 (2005), p. 7783.

5. A. FORTINI, M. DIJKSTRA, M. SCHMIDT, AND P. P. F. WESSELS, *Wall-fluid and liquid-gas interfaces of model colloid-polymer mixtures by simulation and theory*, Phys. Rev. E, 71 (2005), p. 051403.

Other publications from the author:

1. M. DIJKSTRA, R. VAN ROIJ, R. ROTH, AND A. FORTINI, *Effect of many-body interactions on the bulk and interfacial phase behavior of a model colloid-polymer mixture*, Physical Review E, 73 (2006), p. 041404.

2. A. FORTINI, M. MAZZOLA, A. MINA, D. PROVASI, G. COLÒ, G. ONIDA, H. E. ROMAN, AND R. A. BROGLIA, *The role of quantal fluctuations in the optical response of small metal clusters*, J. Phys. B: At. Mol. Opt. Phys., 38 (2005), p. 1581.

3. M. SCHMIDT, A. FORTINI, AND M. DIJKSTRA, *Capillary evaporation in colloid-polymer mixtures selectively confined to a planar slit*, J. Phys.: Condens. Matter, 16 (2004), p. S4159.

4. M. SCHMIDT, A. FORTINI, AND M. DIJKSTRA, *Capillary condensation of colloid-polymer mixtures confined parallel plates*, J. Phys.: Condens. Matter, 15 (2003), p. 3411.

Curriculum vitae

I was born in Orzinuovi (Italy) on the 2nd August 1976. In 1995 I earned a high school diploma in electronics and computer science. The same year I started to study physics at the University of Milan, where in November 2001 I defended cum laude my master thesis on the electron-phonon coupling in small sodium clusters. Afterwards, I worked as a research fellow at the University of Milan in the Theoretical physics of Nuclei, Atomic clusters and protein group of Prof. R. Broglia. My research in Milan was on *ab-initio* calculations of the electronic structure of small metallic atomic clusters. In February 2003, I joined the Soft Condensed Matter group of prof. Alfons van Blaaderen at the Utrecht University as a PhD student. My research at Utrecht was done under the supervision of dr. Marjolein Dijkstra on the simulation study of the phase behaviour of colloidal suspensions, with particular emphasis on the effect of confining geometries.

Dankwoord

Tu prova ad avere un mondo nel cuore e non riesci ad esprimerlo con le parole
F. de André

I arrived in Utrecht four years ago, barely speaking English and with a lot of new things to learn. If I'm here now (almost speaking English and almost a doctor) I have to thank my supervisor Marjolein Dijkstra. Your guidance and patience has meant a lot to me. Despite being very busy, you have always found time to answer my questions and listen to my problems. Your suggestions and advices were always relevant and useful. You have my gratitude for teaching me to think like a scientist. I'm also deeply grateful to Matthias Schmidt with whom I shared the office in the first two years. Your enthusiasm and almost endless flow of ideas have deeply influenced my approach to science. Being part of the SCM group I benefited from the interactions with many brilliant people, like my promotor Alfons van Blaaderen. I want to thank you for the opportunity to be a PhD student in one of the best groups in the world. Your comments and questions during the work discussions have been a constant source of inspiration. I also appreciated discussions with Arnout Imhof and René van Roij. I also want to thank René for the opportunity to be an assistant in his thermal physics courses, where I actually learned a lot about the beautiful science of thermodynamics and statistical physics (my geekness order parameter is diverging after this sentence...I must be close to a first order phase transition).

Next I want to express my gratitude to Remco Tuinier, Paul Wessels, Antti-Pekka Hynninen and Peter Bolhuis. Thank you for your contributions, ideas and advices from which this thesis has benefited greatly.

I want to thank all past and present members of the SCM group for the beautiful atmosphere, both scientifically and socially. I have to thank you all for the effort you put into teaching me some Dutch. Really! My only regret is that I did too little to learn Ducth and get to know you better. Nonetheless, I am infinitely grateful to those who provided me with live translations. I will miss the coffee breaks, lunches, the official and unofficial group outings. It has been a pleasure to meet Didi Derks, Carmen Zoldesi, Yu Ling Wu,

Esther Vermolen, Peter van Oostrum, Mirjam Leunissen, Ahmet Demirôrs, Dannis 't Hart, Job Thijssen, Carlos van Kats, Christina Christova, Astrid van der Horst, Joan Pennikof, Dirk Vossen, Teun Visser, Rao Vukuturi, Johan Stiefelhagen, Patrick Johnson, Paddy Royall, Andrew Campbell, and Catherine Quielliet. I very much appreciated the discussions and the fun I had with all of you. Thank you! Special acknowledgements to the people in the simulation subgroup: Antti-Pekka Hynninen, Slava Savenko, Matthieu Marechal, Michiel Hermes, Alejandro Cuetos and Eduardo Sanz for the help and the interesting discussions we had while working together. Especially, I want to thank Eduardo, with whom I could speak in a language I'm fluent in, for the useful discussions that contributed to the completion of the last chapter of this thesis. Didi for all the discussions on colloid-polymer mixtures, interfaces and shear. Andrew for the interesting discussions about gelation. Carmen and Peter for your dedication and contributions to the group activities. Yu Ling, Esther and Mirjam for your inspiring group meeting contributions. Finally I want to thank Matthias, Alejandro, Matthieu and Michiel for the nice office atmosphere. A special thank also to Esther, Job, Matthieu, Michiel, and Marjolein for the Dutch translation of the thesis summary. A huge thank to Maria for always helping me, and especially for being nice and supportive. I will miss our 4 languages conversations (Dutch-English-Spanish-Italian).

I want to thank Dirk Aarts and Richard Vink for many useful discussions on colloid-polymer mixtures, and all the nice people I have met during the SFB-TR6 workshops. The SFB-TR6 network is also acknowledged for providing financial support for my participation in conferences, workshops and schools.

The work presented in this thesis sums up to many years of CPU time. This wouldn't have been possible without Henk Moss who kept our "clusters" running smoothly. During these four years I also benefited of grants from the Dutch National Computer Facilities foundation for access to supercomputers at SARA.

Voglio ringraziare la mia famiglia, Mamma, Papá, Viviana, Fabrizio, Silvia, ed Eleonora. Nonostante la distanza, la vostra presenza e il vostro supporto sono sempre stati importanti.

Finally I want to thank Alessia, with whom I shared the highs and lows of the PhD life. Your dedicated support deserves much more than what I can express with words. Thank you for being there.